

# AD-A268 792 DOCUMENTATION PAGE



Form Approved  
OMB No. 0705-0188

*[Handwritten initials]*

1. REPORT DATE: 123192  
3. REPORT TYPE AND DATES COVERED: FINAL REPORT 03/15/89-03/15/92

4. TITLE AND SUBTITLE: "Metal/Ceramic Interfaces: Relationships Between Structure and Chemistry"

5. FUNDING NUMBERS: N00014-89-J-1764

6. AUTHOR(S): M. Röhle  
c/o A.G. Evans

7. PERFORMING ORGANIZATION NAME(S) AND ADDRESS(ES):  
MATERIALS DEPARTMENT  
COLLEGE OF ENGINEERING  
UNIVERSITY OF CALIFORNIA  
SANTA BARBARA, CA 93106

8. PERFORMING ORGANIZATION REPORT NUMBER

9. SPONSORING/MONITORING AGENCY NAME(S) AND ADDRESS(ES):  
OFFICE OF NAVAL RESEARCH  
MATERIALS DIVISION  
800 NORTH QUINCY STREET  
ARLINGTON, VA 22217-5000

10. SPONSORING/MONITORING AGENCY REPORT NUMBER

**SD TIC**  
**ELECTE**  
**SEP 01 1993**  
**SD**

11. SUPPLEMENTARY NOTES

12A. DISTRIBUTION/AVAILABILITY STATEMENT: **Approved for public release  
Distribution Unlimited**

12B. DISTRIBUTION CODE

13. ABSTRACT (Maximum 200 words):  
  
SEE ATTACHED EXECUTIVE SUMMARY

14. SUBJECT TERMS: Metal/Ceramic Interfaces, Structure Relationships

15. NUMBER OF PAGES: 82  
16. PRICE CODE

17. SECURITY CLASSIFICATION OF REPORT: UNCLASSIFIED

18. SECURITY CLASSIFICATION OF THIS PAGE: UNCLASSIFIED

19. SECURITY CLASSIFICATION OF ABSTRACT: UNCLASSIFIED

20. LIMITATION OF ABSTRACT

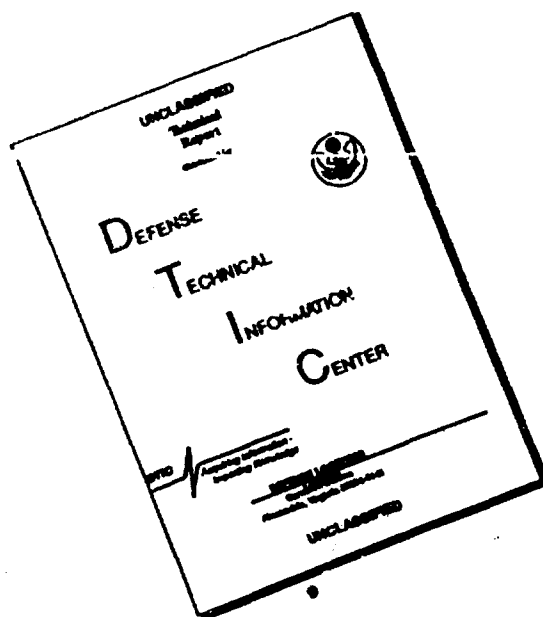
03 8 25 05 5

93-19748



*[Handwritten initials]*

# DISCLAIMER NOTICE



**THIS DOCUMENT IS BEST QUALITY AVAILABLE. THE COPY FURNISHED TO DTIC CONTAINED A SIGNIFICANT NUMBER OF PAGES WHICH DO NOT REPRODUCE LEGIBLY.**

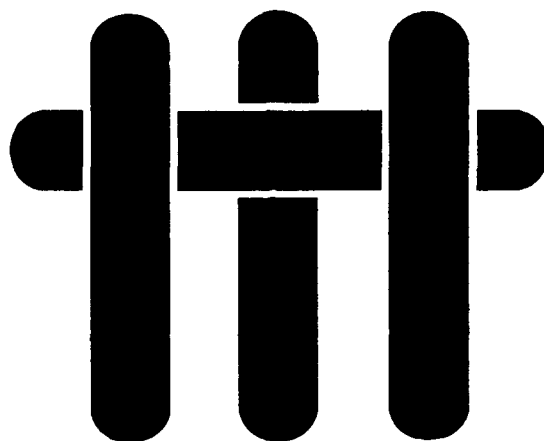
# **FINAL REPORT**

**Office of Naval Research**

Contract No.: N00014-89-J-1764

March 15, 1989 - March 15, 1992

## **M A T E R I A L S**



### **METAL/CERAMIC INTERFACES: RELATIONSHIPS BETWEEN STRUCTURE AND CHEMISTRY**

by

M. Rühle

Materials Department  
College of Engineering  
University of California  
Santa Barbara, California 93106

## EXECUTIVE SUMMARY

Studies have been conducted on interfaces between  $Al_2O_3$ , and three different metals: Nb, Pd and Ni. The objectives have been to establish orientation relationships and to understand the atomistic structure along the interface. In the case of Ni, the formation of a spinel reaction product has also been explored.

For Nb/ $Al_2O_3$ , it has been found that the orientation relationships and the atomic arrangements depend on the temperature at which the interface was formed. Those formed at high temperature by diffusion bonding have (110) planes in the Nb parallel to the interface. There are also misfit dislocations which 'stand-off' the interface. Conversely, interfaces formed at lower temperatures by molecular beam epitaxy have (111) planes in the Nb parallel to the interface. Moreover, the misfit dislocations are located at the interface itself. The differences are attributed to diffusional effects, such as dislocation climb, that can occur at the higher temperatures.

For Pd/ $Al_2O_3$ , the key finding was that the interface could have either oxygen or aluminum terminating planes in the  $Al_2O_3$ , depending on the oxygen activity in the Pd, upon bonding. These studies rationalize various discrepancies evident from previous work.

The principal conclusion of the studies on Ni/ $Al_2O_3$  concerned the oxygen activity in the Ni needed to form a spinel reaction layer. The thermodynamics of the system have been established and predictions made of the conditions needed to create spinel. These predictions are verified by experiment.

NTIS CR&I DTIC TAB Unannounced Justification

Accession For	
NTIS CRA&I	<input checked="" type="checkbox"/>
DTIC TAB	<input checked="" type="checkbox"/>
Unannounced	<input type="checkbox"/>
Justification	<i>for A-235713</i>
By .....	
Distribution /	
Availability Codes	
Dist	Avail and/or Special
<i>A-1</i>	

	<b><u>TITLE</u></b>	<b><u>AUTHOR</u></b>
Article 1.	Electron Microscopy Studies of Nb-Al <sub>2</sub> O <sub>3</sub> Interfaces Formed by Molecular Beam Epitaxy	J. Mayer J. A. Dura C. P. Flynn M. Rühle
Article 2.	Structures of Nb/Al <sub>2</sub> O <sub>3</sub> Interfaces Produced by Different Experimental Routes	J. Mayer W. Mader D. Knauss F. Ernst M. Rühle
Article 3.	High-Resolution Electron Microscopy Studies of Nb/Al <sub>2</sub> O <sub>3</sub> Interfaces	J. Mayer C. P. Flynn M. Rühle
Article 4.	Structure and Defects of MBE Grown Nb-Al <sub>2</sub> O <sub>3</sub> Interfaces	J. Mayer G. Gutekunst G. Möbus J. Dura C. P. Flynn M. Rühle
Article 5.	High Resolution Electron Microscopy Studies of Interfaces between Al <sub>2</sub> O <sub>3</sub> Substrates and MBE Grown NB Films	J. Mayer J. Dura C. P. Flynn M. Rühle
Article 6.	High-Resolution Transmission Electron Microscopy Studies of Structural Modifications in Pd-Al <sub>2</sub> O <sub>3</sub> Interfaces	T. Muschik M. Rühle
Article 7.	HREM Studies of Pd/Al <sub>2</sub> O <sub>3</sub> Interfaces	T. Muschik M. Rühle
Article 8.	The Role of Oxygen for the Spinel Interphase Formation at Diffusion-Bonded Ni/Al <sub>2</sub> O <sub>3</sub> Interfaces	K. P. Trumble M. Rühle

## ELECTRON MICROSCOPY STUDIES OF Nb-Al<sub>2</sub>O<sub>3</sub> INTERFACES FORMED BY MOLECULAR BEAM EPITAXY

J. MAYER\*

Materials Department, University of California, Santa Barbara, CA 93106 (U.S.A.)

J. A. DURA and C. P. FLYNN

University of Illinois at Urbana-Champaign, Materials Research Laboratory, Urbana, IL 61801 (U.S.A.)

M. RÜHLE\*

Materials Department, University of California, Santa Barbara, CA 93106 (U.S.A.)

### Abstract

Niobium films were grown by molecular beam epitaxy on sapphire substrates of different orientations. A unique three-dimensional orientation relationship was determined between the Al<sub>2</sub>O<sub>3</sub> substrate and the niobium film independent of substrate orientation: (0001)<sub>S</sub> || (111)<sub>Nb</sub> and [2 $\bar{1}$ 10]<sub>S</sub> || [1 $\bar{1}$ 0]<sub>Nb</sub>. This observation is in contrast with topotaxial relationships obtained between Al<sub>2</sub>O<sub>3</sub> particles formed by internal oxidation of NbAl alloys where close-packed planes are parallel: (0001)<sub>S</sub> || (110)<sub>Nb</sub>. The atomistic structure of the interface was identified by high resolution electron microscopy. Regions of good matching alternate with regions which contain localized misfit dislocations. These observations will be discussed and compared with results published in the literature.

### 1. Introduction

Studies of the atomistic structures of thin metallic films deposited on ceramic substrates as well as of the corresponding metal-ceramic interfaces are important for fundamental as well as applied reasons. Notably, the niobium-sapphire system has drawn much attention and has been investigated by different researchers [1-12]. This system serves as a model system since both components possess nearly the same thermal expansion coefficients and most thermodynamic quantities (solubility, diffusion data etc.) are well established for niobium and Al<sub>2</sub>O<sub>3</sub>. The Nb-Al<sub>2</sub>O<sub>3</sub> composites are used in different applications such as Josephson junctions and as components

\* Present address: Max-Planck-Institut für Metallforschung, Institut für Werkstoffwissenschaft, 7000 Stuttgart 1 (F.R.G.).

for structural materials. High resolution electron microscopy (HREM) has been used to study Nb-Al<sub>2</sub>O<sub>3</sub> interfaces [9-18] prepared by different experimental routes such as diffusion bonding [9, 10, 16], internal oxidation [13-15], and epitaxial growth of niobium overlayers on Al<sub>2</sub>O<sub>3</sub> substrates [1-8, 11, 12].

The orientation relationship (OR) between niobium and Al<sub>2</sub>O<sub>3</sub> [1-8, 11, 12] is predominantly determined by the manufacturing route. Topotaxial or epitaxial relationships develop after internal oxidation or epitaxial growth respectively. Mader [13, 14] and Kuwabara *et al.* [15] observed that a topotaxial orientation relationship forms between niobium and Al<sub>2</sub>O<sub>3</sub> particles (after internal oxidation) so that close-packed planes between both systems are parallel to each other, *i.e.*

$$(0001)_S \parallel (110)_{Nb} \text{ and } [01\bar{1}0]_S \parallel [001]_{Nb} \quad (S = \text{sapphire})$$

Epitaxial growth of very high quality single-crystal layers of niobium has been a subject of recent experiments [1-8]. For most sapphire surfaces a unique three-dimensional relationship between the niobium and Al<sub>2</sub>O<sub>3</sub> developments which can be characterized by the two sets of zone axes:

$$[0001]_S \parallel [111]_{Nb} \text{ and } [10\bar{1}0]_S \parallel [1\bar{2}1]_{Nb}$$

The latter OR was determined by reflection high energy electron diffraction (RHEED) and X-ray diffraction. Interestingly enough, (001)<sub>Nb</sub> films form on (1 $\bar{1}$ 02)<sub>S</sub>R planes with a distinct deviation from the exact orientation relationship [11, 17] at rather low deposition temperatures.

The aim of these studies was to characterize by HREM the atomistic structures of niobium films and of the Nb-Al<sub>2</sub>O<sub>3</sub> interfaces obtained by molecular beam epitaxy (MBE) growth [1, 2, 8]. Some preliminary results on the mechanical adhesion of the niobium-films on the Al<sub>2</sub>O<sub>3</sub> substrate will also be reported. These observations will be compared with results published in the literature.

## 2. Experimental details

The niobium layers were fabricated in an MBE growth chamber equipped with electron beam sources for evaporating refractory metals. The sapphire substrates were parallel to (0001)<sub>S</sub>, (1 $\bar{1}$ 00)<sub>S</sub> and (11 $\bar{2}$ 0)<sub>S</sub>. The substrates were preheated and cleaned by annealing at about 1500 K for 1 h in a dynamic vacuum of 5 × 10<sup>-6</sup> Pa. The growth of the niobium films was performed while the substrate was heated to 1123 K. Niobium is a powerful getter. A combination of ion pumping and cryopumping was therefore employed to maintain a vacuum in the 10<sup>-6</sup> Pa range during crystal growth so that no niobium oxides could form. The crystal surface structure could be monitored with RHEED which showed that the initial diffraction spots elongated with growth into streaks characteristic of an atomically smooth surface. Typical growth rates were 1 monolayer s<sup>-1</sup>. The resulting thickness ranged from 100 nm to 500 nm.

A special technique was used to obtain transmission electron microscopy (TEM) cross-sectional samples [18] of the niobium film and the Nb-Al<sub>2</sub>O<sub>3</sub> interface. Firstly, the sapphire plates carrying the niobium film were glued to another piece of sapphire to protect the thin metal layer. These "sandwiches" were then cut into strips and glued into a slit within a cylindrical alumina holder (2 mm diameter) which was stiffened by a thin alumina tube (outer diameter 3 mm). Discs were cut from these holders, carefully polished to a thickness of 0.2 mm and dimpled. During ion milling, shields were used to protect the interface and to reduce the effect of the different milling rates of niobium and Al<sub>2</sub>O<sub>3</sub>. This preparation technique resulted in specimens suitable for HREM studies. The foil thickness was less than 20 nm in regions which included the interface. Foil thicknesses down to 5 nm could frequently be obtained.

The HREM studies were performed at the Atomic Resolution Microscope (ARM) at the National Center for Electron Microscopy, Berkeley, CA, U.S.A. The microscope was operated at 800 kV resulting in a point-to-point resolution of better than 0.17 nm [19].

### 3. Experimental results

#### 3.1. Orientation relationships between niobium and Al<sub>2</sub>O<sub>3</sub>

Cross-sectional specimens were investigated in the ARM. Selected area diffraction (SAD) patterns were taken and evaluated. The SAD studies revealed the OR between the sapphire (S) and niobium (Nb):

$$(0001)_S \parallel (111)_{Nb} \quad (1)$$

which had already been identified by Durbin *et al.* [1, 2]. No deviation from this OR (eqn. (1)) could be identified within the experimental error of  $\pm 0.5^\circ$ .

A complete description of an OR requires an additional statement on one set of coinciding directions for both lattices within the interface plane. The following lattice directions coincide for niobium and sapphire:

$$[2\bar{1}\bar{1}0]_S \parallel [1\bar{1}0]_{Nb} \quad (\text{direction A}) \quad (2)$$

$$[10\bar{1}0]_S \parallel [1\bar{2}1]_{Nb} \quad (\text{direction B}) \quad (3)$$

The angle between the directions A and B is  $30^\circ$ . Deviations from the ORs in eqns. (2) and (3) could not be found within the experimental error ( $\pm 0.5^\circ$ ). Figure 1 illustrates the relative orientation of the two crystals (eqns. (1)–(3)). An important feature of this arrangement is that the threefold axes of the two crystals are parallel:

$$[0001]_S \parallel [111]_{Nb} \quad (4)$$

which is the zone axis perpendicular to the interface formed on (0001)<sub>S</sub> substrates.

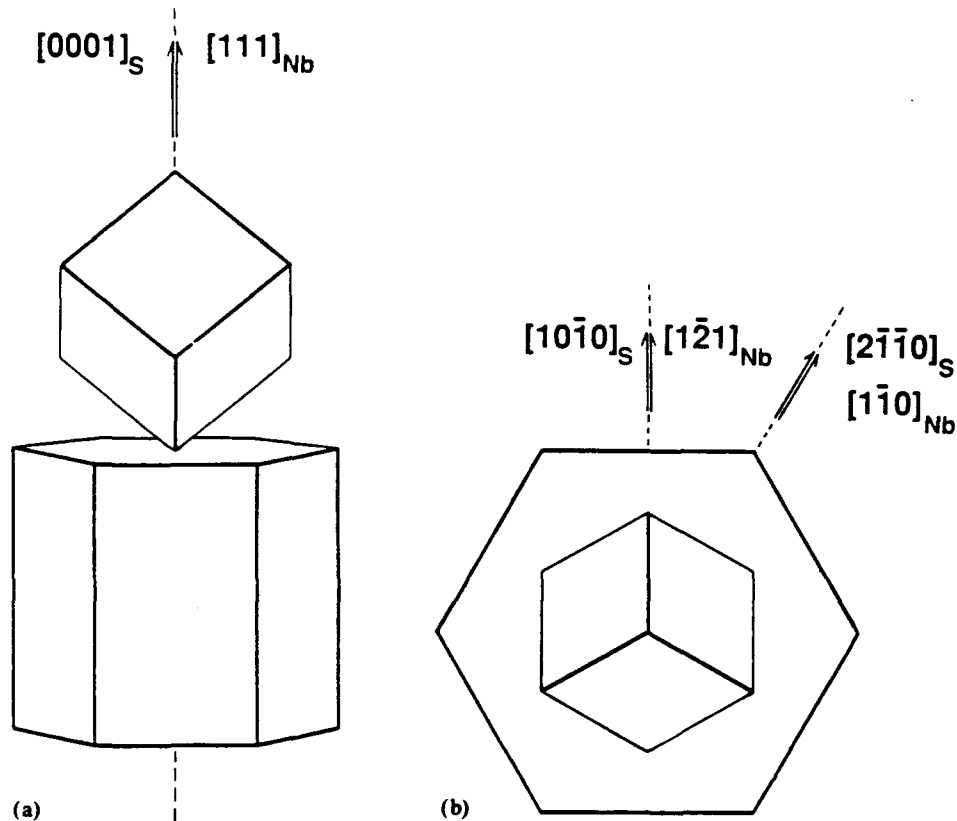


Fig. 1. OR between sapphire substrates and niobium overlayers. (a) The three-dimensional OR  $[0001]_S \parallel [111]_{Nb}$  ( $S = \text{sapphire}$ ) holds for all substrate orientations. (b) OR for different directions within the  $(0001)_S \parallel (111)_{Nb}$  plane.

### 3.2. Direct lattice images of the niobium film and of near-interface regions

Conventional TEM micrographs (Fig. 2) and direct lattice images (Fig. 3) of the niobium film showed that the niobium films possess low dislocation densities. The dislocation density  $\rho$  is so small that  $\rho$  could not be determined from TEM micrographs within any statistical significance. This demonstrates the high quality of the MBE grown films which was also identified by diffraction techniques [8].

Direct lattice imaging of near-interface regions allows the determination of the atomistic structure of the interface as well as the analysis of defects associated with the interface such as misfit dislocations etc. To obtain interpretable HREM images the electron beam should be incident along high symmetry directions in both crystals and should be parallel to the plane of the interface. A three-dimensional analysis of the structure requires HREM images taken under different directions of the incident electron beam with respect to the interface orientation. These conditions are fulfilled if the



Fig. 2. Conventional bright field image of a niobium film on a sapphire substrate: only defects introduced during ion beam thinning can be identified.

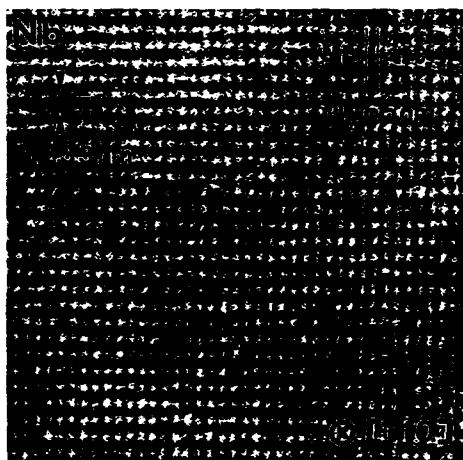


Fig. 3. Direct lattice image of the niobium film in [110] orientation. The niobium lattice can readily be identified.  $d_{002} = 0.165$  nm and  $d_{110} = 0.233$  nm are marked.

electron beam is parallel to directions A and B (see Fig. 1(b)). High resolution electron micrographs were taken from the same interface in both directions by simply tilting the specimen inside the ARM. Figure 4 shows an overview of a large area of near-interface regions. The defocus of the objective lens is slightly more positive ( $\Delta f = -40$  nm) than the Scherzer defocus ( $\Delta f = -55$  nm). At this defocus the atomistic distance corresponding to the (200) planes with  $d = 0.165$  nm becomes clearly visible [20]. Lattice planes can readily be identified in  $\text{Al}_2\text{O}_3$  and niobium. The foil thicknesses of niobium and  $\text{Al}_2\text{O}_3$  are identical. In niobium, regions of good matching (M) and poor matching (D) alternate at the interface. Steps can also be identified (S). The region of good matching (Fig. 4, M) is imaged at a higher magnifica-

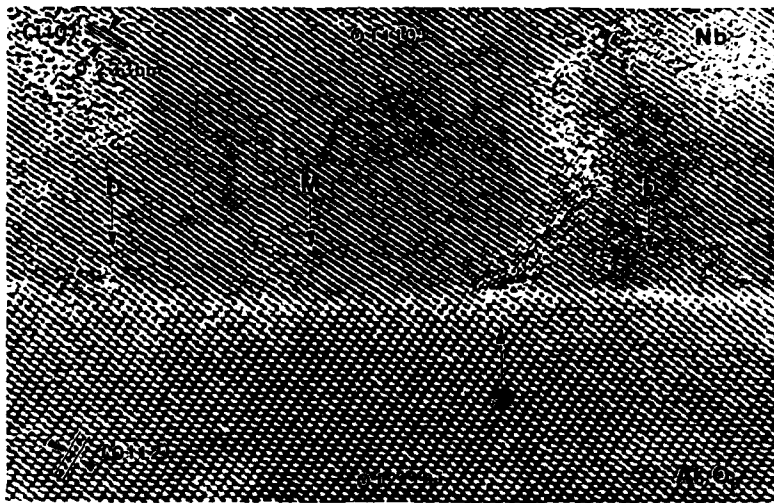


Fig. 4. High resolution image of an Nb-Al<sub>2</sub>O<sub>3</sub> interface. Direction of incoming electrons parallel to  $[1\bar{1}0]_{\text{Nb}}$  and defocus value  $\Delta f = -40$  nm (Scherzer value,  $-55$  nm). Lattice planes can clearly be identified in both sapphire and niobium. Foil thickness about 8 nm. At the interface regions of good matching (M) and poor matching (D) alternate. S, step in the substrate.

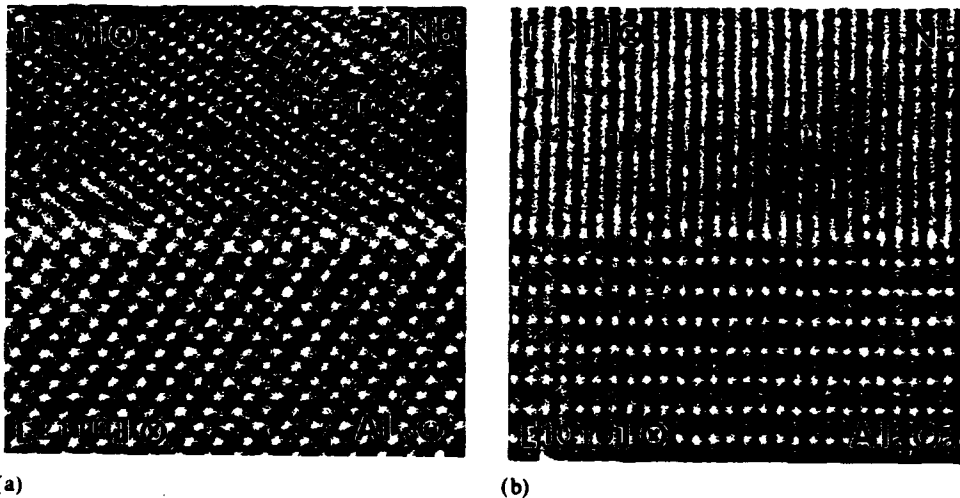


Fig. 5. High resolution image of Nb-Al<sub>2</sub>O<sub>3</sub> interface: region of good matching (M). (a) Direction A with  $[2\bar{1}\bar{1}0]_s \parallel [1\bar{1}\bar{1}]_{\text{Nb}}$ . (b) Direction B with  $[10\bar{1}0]_s \parallel [1\bar{2}\bar{1}]_{\text{Nb}}$ .

tion in Fig. 5. Figure 5(a) shows the interface with the electron beam parallel to direction A. Niobium and Al<sub>2</sub>O<sub>3</sub> possess the same thickness and lattice planes transfer continuously from niobium to Al<sub>2</sub>O<sub>3</sub>.

Figure 5(b) is a micrograph of the same interface viewed along orientation B. Only  $(10\bar{1})$  lattice planes with a spacing of 0.233 nm are visible in the niobium crystal in regions of good matching (M). The  $(222)$  lattice planes

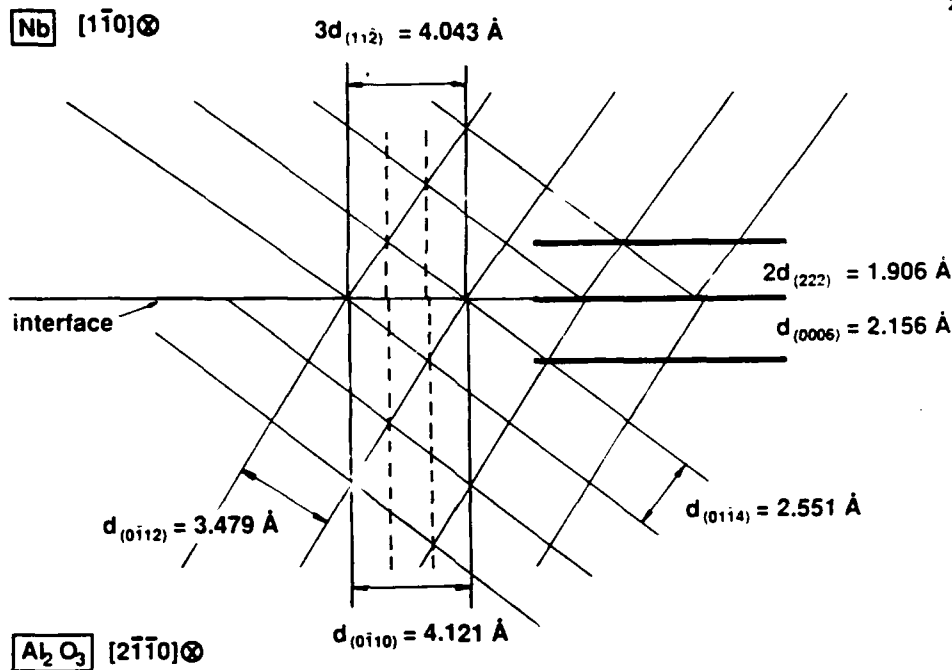


Fig. 6. Schematic drawing of selected lattice planes in niobium and  $\text{Al}_2\text{O}_3$  in direction A.

(perpendicular to  $(10\bar{1})$ ) possess a spacing of 0.095 nm which is beyond the resolution limit and information limit of the ARM. Therefore only  $(10\bar{1})$  lattice fringes are visible. In both orientations (Figs. 5(a) and 5(b)) a perfect match of the niobium and  $\text{Al}_2\text{O}_3$  lattice at the interfaces is visible. Figure 6 shows schematically several lattice planes in niobium and  $\text{Al}_2\text{O}_3$  for an axis of the incident electron beam parallel to direction A. The lattice mismatch of  $(0\bar{1}10)_S$  and  $(11\bar{2})_{Nb}$  planes perpendicular to the interface is 1.9%. The niobium lattice possesses the smaller spacing. The  $(0006)_S$  and  $(222)_{Nb}$  planes are parallel to the interface and possess a lattice mismatch of 11.9%. This larger mismatch is significant if steps are present at the interface; see Section 3.4.

### 3.3. Localized misfit dislocations at the interface

The misfit of 1.9% between the  $(11\bar{2})_{Nb}$  and  $(0\bar{1}10)_S$  planes perpendicular to the interface is accommodated by localized defects (misfit dislocations) in regions of poor matching (Fig. 4). These localized misfit dislocations at the interface are spaced periodically about one every 50  $(1\bar{1}2)_{Nb}$  lattice planes (Fig. 4). A higher magnification of region D of Fig. 4 is shown in Fig. 7. Figure 7(a) represents the images parallel to direction A. A misfit dislocation can clearly be identified. The Burgers vector is  $\frac{1}{2} [110]_{Nb}$ . No "stand-off" distance [13-15, 21] of the misfit dislocation can be identified.

The projection of the extra plane of the misfit dislocation is parallel to the electron beam in direction A. For direction B (Fig. 7(b)) the extra

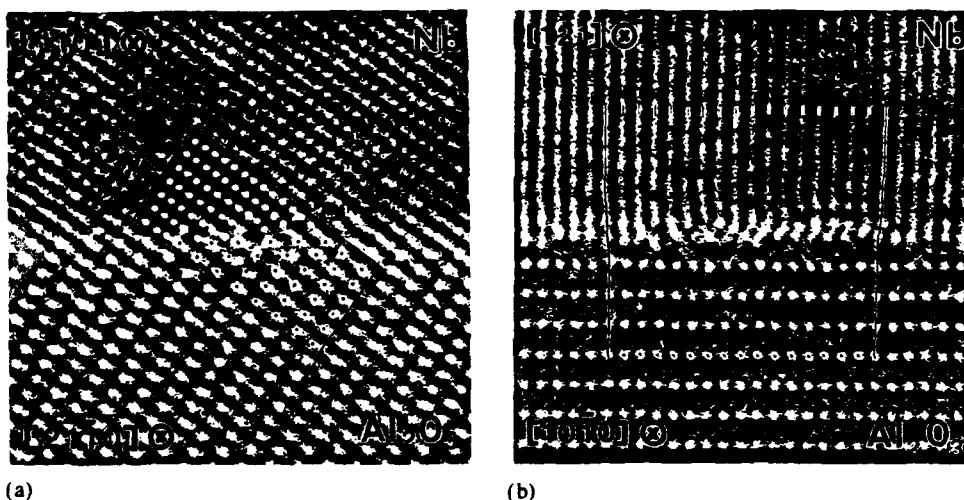


Fig. 7. High resolution image of Nb-Al<sub>2</sub>O<sub>3</sub>: region of poor matching. A misfit dislocation forms with no stand-off distance. (a) Direction A; the core of the misfit dislocation can readily be identified. (b) Direction B; the core of the dislocation line is inclined with respect to the electron beam. The region of no matching of corresponding lattice planes is marked. This region corresponds to the projection width of the additional lattice plane.

niobium plane is inclined at an angle of 30°. There is no fit of corresponding planes in niobium and Al<sub>2</sub>O<sub>3</sub> along the projection of the inclined plane of the misfit dislocation which is clearly visible in Fig. 7(b). The projected length  $x$  can be measured:

$$x = (17 \pm 2)d_{110} \quad (d_{110} = 0.233 \text{ nm})$$

and the thickness  $t$  of the foil can be evaluated with the known tilt angle  $\phi$ :

$$t = 8.0 \pm 1.0 \text{ nm}$$

### 3.4. Steps at the interface

The sapphire surface will usually not be atomically flat over large distances. Steps are expected if, for example, small deviations exist between the surface plane and the (0001)<sub>S</sub> basal plane of sapphire prior to thin film evaporation. Such surface steps can be recognized at the interface (Fig. 4). Careful inspection revealed (especially on micrographs imaged under a grazing angle, the "Scheimpflug technique" [22], Fig. 8) that the step height of the sapphire is always a multiple of the distance of the O<sup>2-</sup> layers within the Al<sub>2</sub>O<sub>3</sub> structure parallel to (0001)<sub>S</sub>. This distance corresponds to (0006)<sub>S</sub> planes with  $d = 0.2165$  nm. The corresponding lattice spacing in niobium is  $d_{111} = 0.1906$  nm and is 11.9% smaller than the O<sup>2-</sup> spacing. Because of this mismatch (Fig. 6), the niobium lattice is distorted adjacent to steps. The recognizable distortion extends up to about 10 nm into the niobium film.

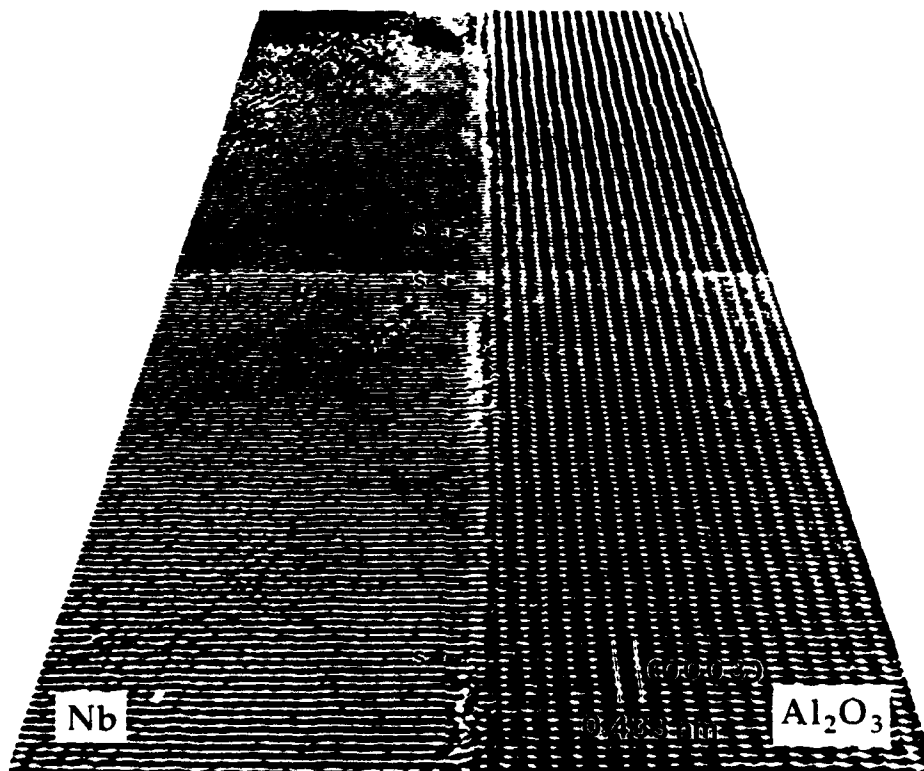


Fig. 8. "Scheimpflug image" [22] of HREM images in direction B. Steps can be observed (S). The step height corresponds to the (0006) plane distance.

### 3.5. Niobium overlayers on $(1\bar{1}00)_S$ substrates

Preliminary observations on niobium thin films deposited on  $(1\bar{1}00)_S$  substrates show that the same three-dimensional OR is maintained as for films on  $(0001)_S$  substrates (Fig. 1). The flatness of the  $(1\bar{1}00)_S$  substrates for this orientation is not as good as that of the corresponding  $(0001)_S$  surfaces. Pyramidal elevations can be seen (Fig. 9) and these elevations cause strong distortions in the niobium lattice. The distortion reaches about 10 nm into the niobium.

### 3.6. Stress state and decohesion of the niobium films

Films with thicknesses smaller than  $1\ \mu\text{m}$  were carefully inspected by RHEED and low energy electron diffraction techniques [1, 2, 8]. No distortions or displacements of reflections could be identified. This is indicative of a very small stress level within the film. Decohesion of the film could not be observed. Indentation experiments were performed [23, 24]; however, no decohesion of the film could be observed. Only a plastic deformation within the niobium overlayer could be identified. Higher loading of the indent lead to a cracking of the ceramic substrate.

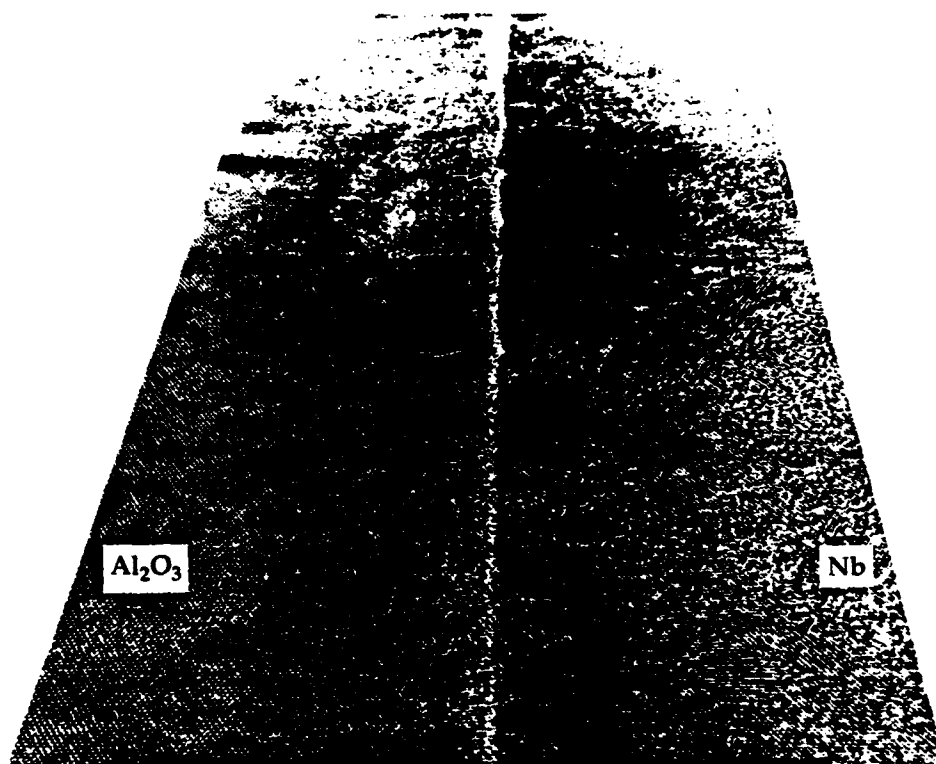


Fig. 9. High resolution micrograph imaged with "Scheimpflug" technique.  $(1\bar{1}00)_S \parallel (11\bar{2})_{Nb}$ , electron beam parallel  $[0001]_S \parallel [111]_{Nb}$ . Pyramidal elevations are clearly visible.

#### 4. Discussion

The observed OR for niobium films on differently oriented sapphire substrates is equivalent to results described in the literature [1, 2, 8]. The three-dimensional OR between niobium and  $Al_2O_3$  has been confirmed with  $(0001)_S \parallel (111)_{Nb}$  and  $[10\bar{1}0]_S \parallel [1\bar{2}1]_{Nb}$ . Knowles *et al.* [11] demonstrated by HREM that the same OR holds for (001) niobium films deposited epitaxially on  $(10\bar{1}2)R$  planes of sapphire. The characteristic misorientation from the "three-dimensional OR" is caused by small locally misoriented regions in the immediate vicinity of the Nb- $Al_2O_3$  interface.

Qualitatively the niobium film formation could be described as follows. The sapphire substrate was annealed at  $5 \times 10^{-8}$  Pa at 1500 K in a dynamic vacuum. The annealing leads to a reconstruction of the  $\alpha$ - $Al_2O_3$  surface to a  $(\sqrt{31} \times \sqrt{31})R \pm 9^\circ$  structure [25-27]. At the surface the Al:O ratio is about 1:1, and thus the sapphire is not stoichiometric at the surface. The RHEED studies performed at  $\alpha$ - $Al_2O_3$  surfaces prior to deposition of the niobium film indicate that a similar reconstruction is present. In addition, atomistic steps (facets) exist at the surface of sapphire because of small deviations between

surface orientations and the  $(0001)_S$  basal plane. Those steps may act as nucleation centers for the niobium film. The growth conditions are selected such that two-dimensional crystal growth occurs [8]. The reconstructed, aluminum-rich surface still possesses 3-fold symmetry with characteristic distances equivalent to atomistic distances of  $(111)_{Nb}$  planes. For symmetry reasons it is expected that the first deposited niobium layer has an OR which is dictated by the symmetry of the sapphire surface leading to  $(0001)_S \parallel (111)_{Nb}$ . No twins could be identified in the (nearly) perfect niobium film. It must be assumed that a unique atomistic relationship exists between the sapphire surface and the monoatomic niobium layer. There exists only one set of niobium atom positions on the non-reconstructed sapphire surface which leads to a twin-free film (Fig. 10). Niobium atoms must be located on the terminating  $O^{2-}$  layer of sapphire on top of "empty sites" (Fig. 10). A quantitative evaluation of the HREM images should verify this hypothesis.

The formation of the "core" of the misfit dislocations can be explained using Frank and Van der Merwe's model [28, 29]. Subsequent niobium layers bond to the first layer by metallic bonding, building up the misfit dislocation nucleated at the interface. This model may explain the growth on  $(0001)_S$  plane sapphire. It is, however, difficult to explain the (general) three-dimensional OR between niobium and  $Al_2O_3$  which develops also on other sapphire surfaces.

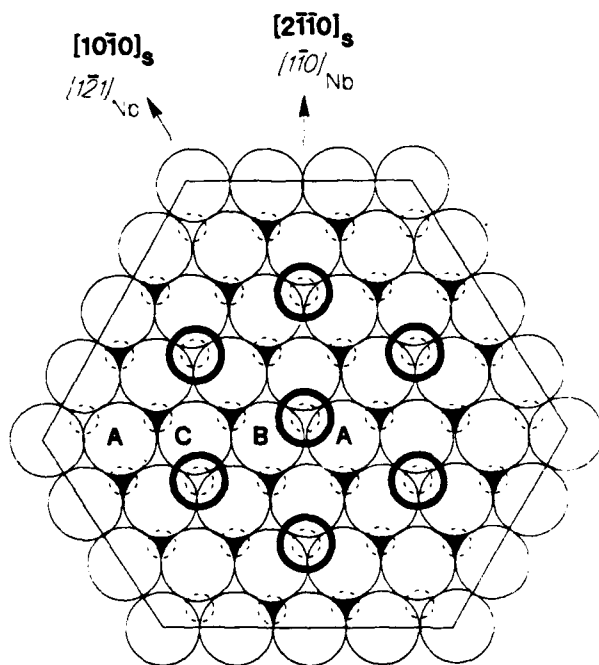


Fig. 10. Schematic drawing of non-reconstructed  $(0001)_S$  basal surface.  $\circ$ ,  $O^{2-}$  ions;  $\nabla$ ,  $Al^{3+}$ ;  $\circ$ , niobium atoms. It is assumed that the  $O^{2-}$  ions form the outermost layer. The niobium atoms of the first layer are positioned above the empty sites of the first  $Al^{3+}$  layer which lies immediately next to the outermost  $O^{2-}$  layer.

A careful inspection of HREM images taken under different focusing conditions of regions very close to the interface reveals that no reconstruction of sapphire close to the interface is recognizable. It must be assumed that the excess aluminum atoms of the reconstructed (0001) surface [25-27] diffuse into the niobium, which has a sufficiently high solubility for aluminum. Quantitative evaluation of the high resolution images will support this qualitative statement.

The observed OR, and hence the arrangements of the atoms at the interface, is different from the OR obtained at Nb-Al<sub>2</sub>O<sub>3</sub> interfaces in internally oxidized NbAl alloys. For both systems Al<sub>2</sub>O<sub>3</sub> is bound by an oxygen layer of the basal plane [12, 13, 15]. However, different niobium planes terminate at the interface. Typically, close-packed (110) planes juxtapose close-packed planes of Al<sub>2</sub>O<sub>3</sub> as interfaces formed by internal oxidation. The OR is symmetry dictated for epitaxial growth. It is not obvious which interface of the different ORs possesses the lower interfacial energy. Further experimental studies may answer this question.

The misfit dislocations observed in MBE grown niobium films do not show a "stand-off" which was observed at interfaces formed by internal oxidation or diffusion bonding [13, 15, 17]. The localization of the inserted plane is well defined (Fig. 7(a)) and a perfect match of the niobium atoms on the sapphire lattice is obtained within 0.5 nm on either side of the dislocation. Since the deposition of the niobium film was performed at much lower temperatures than the diffusion bonding or the internal oxidation this geometry (Fig. 7(a)) of the misfit dislocations might not be thermally stable. The dislocations could climb from the interface to a stable stand-off distance if the samples are heat treated or deposited at higher temperature. Such experiments would also show whether the OR observed in our studies is thermally stable or whether it is only formed at the given growth conditions as a result of the kinetics of the epitaxial growth process.

The niobium overlayers show an extremely high perfection which is typical for MBE grown films. However, stresses generated by unevenness of the substrate may extend up to 200 nm into the film and influence the properties of the film. The interfacial roughnesses may also be locations where dislocations nucleate when the film is stressed.

Tests for the decohesion of the niobium films from the sapphire substrate were not successful. After indentation experiments the niobium film deformed plastically and the sapphire cracked after application of a higher load. Evans and coworkers [23, 24] showed that decohesion is governed by a critical non-dimensional parameter, the decohesion number

$$\Omega = K_c / \sigma_0 \sqrt{h}$$

where  $\sigma_0$  is the stress in the film,  $h$  is the film thickness and  $K_c$  the fracture resistance. Internal stresses  $\sigma_0$  within the niobium films and the Al<sub>2</sub>O<sub>3</sub> substrate are practically zero since Al<sub>2</sub>O<sub>3</sub> and niobium possess the same thermal expansion coefficient so that no thermal stresses develop during cooling from fabrication temperature.

Perfect single-crystal films possess no internal stresses. This contrasts to fine-grained polycrystalline films [30]. In addition, the fracture toughnesses  $K_c$  of niobium and the interfaces are larger than  $K_c$  of sapphire which leads to an  $\Omega_c$  dictated by the fracture resistance of the substrate and not by the film or interface. These arguments explain the failure of the decohesion measurements.

### Acknowledgments

This work was supported in part by DARPA through the University Research Initiative Program at UCSB, ONR Contract N00014-86-K-0753 (J.M.), and by the Department of Energy under Contracts DE-FG03-88ER45351 (M.R.) and DE-AC02-76ER01198 (C.P.F.). The authors acknowledge the use of the Atomic Resolution Microscope at the National Center for Electron Microscopy in Berkeley, CA, U.S.A.

### References

- 1 S. M. Durbin, J. E. Cunningham, M. E. Mochel and C. P. Flynn, *J. Phys. F*, **11** (1981) L223.
- 2 S. M. Durbin, J. E. Cunningham and C. P. Flynn, *J. Phys. F*, **12** (1982) L75.
- 3 Y. Igarashi and M. Kanayama, *J. Appl. Phys.*, **57** (1985) 849.
- 4 S. A. Wolf, S. B. Quadri, J. H. Claassen, T. L. Francavillo and B. J. Dalrymple, *J. Vac. Sci. Technol. A*, **4** (1986) 524.
- 5 Y. Nishihata, N. Nakayama, H. Kato, N. Sano and H. Terauchi, *J. Appl. Phys.*, **60** (1986) 3523.
- 6 F. J. Camelas, H. He and R. Clarke, *Phys. Rev. B*, **38** (1988) 6334.
- 7 J. H. Claassen, S. A. Wolf, S. B. Quadri and C. D. Jones, *J. Cryst. Growth*, **81** (1987) 557.
- 8 C. P. Flynn, in M. Rühle, A. G. Evans, M. F. Ashby and J. P. Hirth (eds.), *Proc. Acta/Scripta Conf. on Metal/Ceramic Interfaces*, Pergamon, Oxford, 1990, p. 168.
- 9 M. Florjancic, W. Mader, M. Rühle and M. Turwitt, *J. Phys. Colloq. C4*, **46** (1985) 129.
- 10 W. Mader and M. Rühle, *Acta Metall.*, **37** (1989) 853.
- 11 K. M. Knowles, K. B. Alexander, R. E. Somekh and W. M. Stobbs, *Inst. Phys. Conf. Ser.* **90** (1987) 245.
- 12 J. Mayer, W. Mader, F. O. Philipp, C. P. Flynn and M. Rühle, *Inst. Phys. Conf. Ser.* **98** (1989) 349.
- 13 W. Mader, *MRS Symposia Proceedings*, Vol. 82, Materials Research Society, Pittsburgh, PA, 1987, p. 403.
- 14 W. Mader, *Z. Metallkd.*, **80** (1989) 139.
- 15 M. Kuwabara, J. C. H. Spence and M. Rühle, *J. Mater. Res.*, **4** (1989) 972.
- 16 D. Knauss and W. Mader, unpublished research, 1989.
- 17 D. B. McWhan, *MRS Symposia Proceedings*, Vol. 35, Materials Research Society, Pittsburgh, PA, 1985, p. 493.
- 18 A. Strecker, J. Mayer and M. Rühle, to be published.
- 19 C. J. D. Hetherington, E. C. Nelson, K. H. Westmacott, R. Gronsky and G. Thomas, *MRS Symposia Proceedings*, Vol. 139, Materials Research Society, Pittsburgh, PA, 1989, p. 277.
- 20 J. C. H. Spence, *Experimental High Resolution Electron Microscopy*, Clarendon, Oxford, 1981.
- 21 S. K. Kamat, J. P. Hirth and B. Carnahan, *MRS Symposia Proceedings*, Vol. 103, Materials Research Society, Pittsburgh, PA, 1988, p. 55.
- 22 L. Bitzek, W. E. Wunderlich and W. Mader, *Prakt. Metallogr.*, **25** (1988) 384.

## STRUCTURES OF Nb/Al<sub>2</sub>O<sub>3</sub> INTERFACES PRODUCED BY DIFFERENT EXPERIMENTAL ROUTES

J. MAYER\*, W. MADER, D. KNAUSS, F. ERNST, AND M. RÜHLE\*

Max-Planck-Institut für Metallforschung, D-7000 Stuttgart 1, FRG

\* Formerly with: Materials Department, University of California, Santa Barbara, CA 93106

### ABSTRACT

Nb/Al<sub>2</sub>O<sub>3</sub> interfaces were produced by (i) diffusion bonding of single crystalline Nb and Al<sub>2</sub>O<sub>3</sub> at 1973 K, (ii) internal oxidation of a Nb-3at.% Al alloy at 1773 K, and (iii) molecular beam epitaxy (MBE) growth of 500 nm thick Nb overlayers on sapphire substrates at 1123 K. Cross-sectional specimens were prepared and studied by conventional (CTEM) and high resolution transmission electron microscopy (HREM). The orientation relationships between Nb and Al<sub>2</sub>O<sub>3</sub> were identified by diffraction studies. HREM investigations revealed the structures of the different interfaces including the presence of misfit dislocations at or near the interface. The results for the different interfaces are compared.

### INTRODUCTION

The technical applications of modern engineering materials often require two different components (such as metals and ceramics) to be bonded. In studies of the atomistic structure of metal/ceramic interfaces niobium/sapphire has been used as a model system [1-4] since both components possess nearly the same thermal expansion coefficients and most thermodynamic quantities (solubility, diffusion data, etc.) are well established.

Investigations of Nb/Al<sub>2</sub>O<sub>3</sub> interfaces manufactured by different experimental routes may guide to an evaluation of energetically favourable atomic arrangements at the interface. In addition, the analysis of interfacial defects, such as misfit dislocations, may lead to a better understanding of the interface strength and processes occurring during the interface formation.

Three different routes have been used to produce the interfaces, namely diffusion bonding of single crystals [5], internal oxidation of metallic alloys [2], and epitaxial growth of a metallic overlayer on ceramic substrates [6-8]. The aim of the present studies was to characterize the orientation relationships and the atomic structures of the interfaces of specimens produced by all three methods and to compare the results.

### EXPERIMENTAL

**Specimen Production: Diffusion Bonding (Specimen I):** Single crystals of Nb and sapphire were diffusion bonded at 1973 K for 2 h in a vacuum of  $1.3 \times 10^{-3}$  Pa. A small compressive load of 10 MPa kept the polished surfaces in contact [4].

**Internal Oxidation (Specimen II):** A Nb-3at.%Al alloy was internally oxidized by exposing the material at 1723 K for 45 min to an oxygen atmosphere (pressure  $5 \times 10^{-3}$  Pa). This treatment produces Al<sub>2</sub>O<sub>3</sub> precipitates [2].

**Epitaxial Nb Layers on Sapphire (Specimen III):** Thin overlayers of Nb on  $\alpha$ -sapphire substrates were fabricated in an MBE growth chamber equipped with electron beam sources [8]. The growth of the Nb films was performed while the

substrate was heated to 1123 K. A combination of ion pumping and cryopumping was employed to maintain a vacuum in the  $10^{-6}$  Pa range during crystal growth. Typical growth rates were one monolayer/s.

**TEM Specimen Preparation:** Specimens I and III were cut perpendicular to the Nb/Al<sub>2</sub>O<sub>3</sub> interface to obtain cross-section specimens suitable for HREM. Special alumina cross-section holders were used for the embedding of Specimen III prior to cutting. Discs of 3 mm diameter were obtained which were carefully polished, dimpled, and ion thinned. During ion-milling shields were used to protect the interface and to reduce the effect of the different milling rates of Nb and Al<sub>2</sub>O<sub>3</sub>.

TEM samples of Specimen I were investigated in a 400 kV HREM instrument, Specimen II samples in a 200 kV HREM, and Specimen III samples in the ARM at Berkeley which was operated at 800 kV.

## EXPERIMENTAL RESULTS

The orientation relationships (OR) between Nb and Al<sub>2</sub>O<sub>3</sub> were evaluated from selected area diffraction (SAD) patterns. The results are summarized in Table 1 for the different specimens. No reaction layer formation could be detected in all three types of specimens.

**Structural Observations at Specimen I:** HREM investigations of the diffusion-bonded Nb/Al<sub>2</sub>O<sub>3</sub> interfaces revealed that the Al<sub>2</sub>O<sub>3</sub> lattice remains undistorted up to the interface. Facets are observed if the plane of the interface deviates from the basal plane of sapphire.

In contrast to earlier observations [4], misfit dislocations were observed at the diffusion-bonded Nb/Al<sub>2</sub>O<sub>3</sub> interface (see Fig. 1). The misfit dislocations accommodate the difference in lattice plane spacings of Nb and Al<sub>2</sub>O<sub>3</sub> (Nb:  $d_{110} = 0.2334$  nm and  $\alpha$ -Al<sub>2</sub>O<sub>3</sub>:  $d_{2110} = 0.2382$  nm) and their core is located in the Nb at a characteristic "stand-off" distance from the interface. The findings are very similar to those obtained for interfaces between Al<sub>2</sub>O<sub>3</sub> precipitates and Nb (see below).

**Structural Observations at Specimen II:** The Al<sub>2</sub>O<sub>3</sub> precipitates formed by internal oxidation of NbAl alloys are typically platelet-shaped with flat large interfaces [2,3]. The precipitates condense in a metastable rhombohedral structure denoted as  $\alpha'$ -Al<sub>2</sub>O<sub>3</sub> [2]. The lattice spacings of Nb and Al<sub>2</sub>O<sub>3</sub> are slightly different along the interface. This difference is accommodated by misfit dislocations which are arranged with approximately equal distances [2]. The distances of the dislocations can be explained by the misfit in the corresponding lattice spacings.

Table I Summary of observations (\* preset; S: sapphire)

Spec.	Prep. techn.	Orientation relationship	React. layer	Misf. disl.	stand-off
I	diff. - bonding	$(0001)_S \parallel (110)_{Nb}; [01\bar{1}0]_S \parallel [001]_{Nb}^*$	-	+	+
II	inter. - oxid.	$(0001)_S \parallel (110)_{Nb}; [01\bar{1}0]_S \parallel [001]_{Nb}$	-	+	+
III	epitax. films	$(0001)_S \parallel (111)_{Nb}; [2\bar{1}\bar{1}0]_S \parallel [\bar{1}\bar{1}0]_{Nb}$	-	+	-

Most of the core of the misfit dislocations does not lie within the interface, but is located a few layers away from the interface. The "stand-off" distance, measured from the interface, is approx. 0.9 nm.

**Structural Observations at Specimen III:** The HREM investigations show that in the Nb large regions of good matching (Fig. 2a) alternate with localized regions of poor matching (Fig. 2b) along the interface. Steps in the interface can also be identified. Fig. 2b shows that the lattice defect present in regions of poor matching can

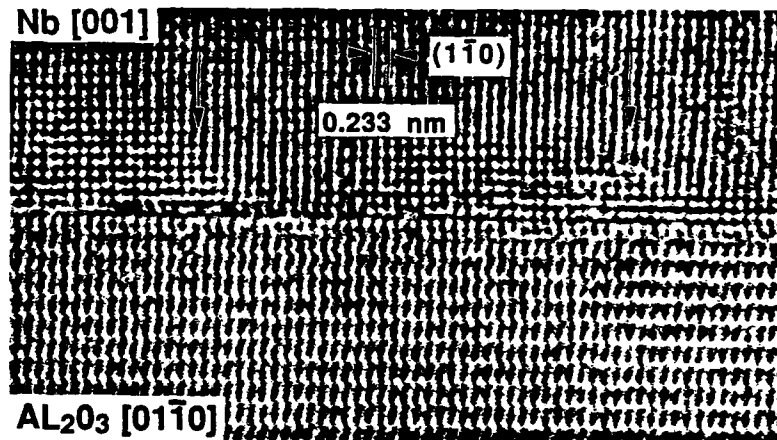


Fig. 1: Lattice image of a diffusion bonded Nb/Al<sub>2</sub>O<sub>3</sub> interface. Misfit dislocations (arrowed) with a characteristic "stand-off" distance were observed in this projection.

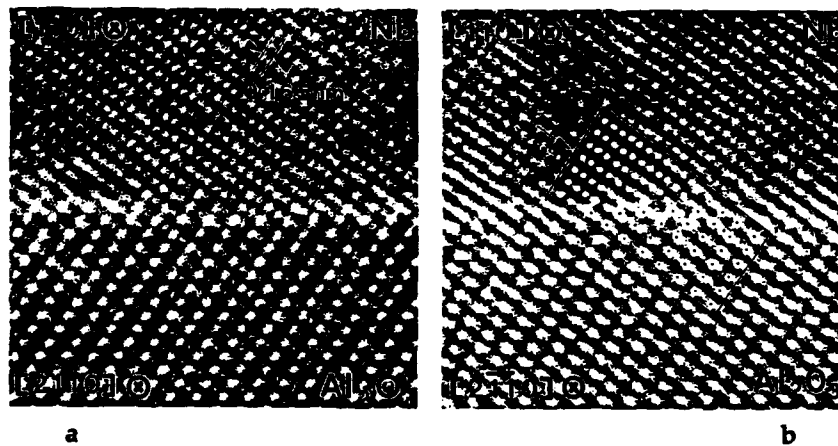


Fig. 2: High resolution image of a Nb/Al<sub>2</sub>O<sub>3</sub> interface produced by MBE growth. At the interface regions of good matching (a) and poor matching (b) alternate. In the regions of poor matching a misfit dislocation forms with no "stand-off" distance (b).

best be represented by a slightly delocalized misfit dislocation which does not show any "stand-off" distance. The misfit dislocations are spaced periodically with a distance of about 50 lattice planes in Nb. This can easily be explained by the 1.9% misfit between the corresponding  $(11\bar{2})_{\text{Nb}}$  and  $(0\bar{1}10)_{\text{S}}$  planes which lie perpendicular to the interface.

## DISCUSSION

The orientation relationship (OR) between Nb and  $\text{Al}_2\text{O}_3$  is prefixed in the diffusion-bonded specimens. However, it is expected that for Specimen II (internally oxidized) and Specimen III (epitaxial films) those ORs should develop which lead to a low energy configuration of the system. It is interesting to note that Specimen II and Specimen III possess essentially different ORs (Table I) indicating that different constraints exist during interface formation. The reasons for the occurrence of the different ORs are not yet revealed.

The OR observed in Specimen II is characterized by parallel close-packed planes of both materials forming the interface. However, the OR observed in Specimen III is not only determined by the interface planes but involves a unique three-dimensional relationship between the Nb and  $\text{Al}_2\text{O}_3$  crystal orientations which can be found for various choices of substrate orientation [7,8]. This special OR can be characterized by  $[0001]_{\text{S}} \parallel [111]_{\text{Nb}}$  which seems to be dictated by geometrical considerations.

Misfit dislocations could be observed in all specimens, in contrast to an earlier study [4] where diffusion bonds with a different OR had been investigated. However, no "stand-off" distance could be determined in Specimen III (see Fig. 2b). The temperature during interface formation (1123 K) is appreciably lower than the temperatures chosen for Specimen I and II. At this stage we assume that the lower temperature of Specimen III does not allow the dislocation to climb into the actual equilibrium position so that it stays (purely due to geometrical constraints) at the interface.

## ACKNOWLEDGEMENTS

The authors are thankful to C.P. Flynn for providing Specimen III and gratefully acknowledge the use of the Atomic Resolution Microscope at the National Center for Electron Microscopy in Berkeley/CA, USA.

## REFERENCES

1. M. Florjancic, W. Mader, M. Rühle, and M. Turwitt, *J. de Physique* **46**, C4-129 (1985).
2. W. Mader, *Mat. Res. Soc. Symp. Proc.* **82**, 403 (1987).
3. M. Kuwabara, J.C.H. Spence, and M. Rühle, *J. Mat. Res.* **4**, 972 (1989).
4. W. Mader and M. Rühle, *Acta metall.* **37**, 853 (1989).
5. M. Turwitt, G. Elssner, and G. Petzow, *J. de Physique* **46**, C4-123 (1985).
6. S.M. Durbin, J.E. Cunningham, M.E. Mochel, and C.P. Flynn, *J. Phys. F* **11**, L223 (1981).
7. S.M. Durbin, J.E. Cunningham, and C.P. Flynn, *J. Phys. F* **12**, L75 (1982).
8. C.P. Flynn in *Proc. Acta/Scripta Conf. on Structure, Chemistry and Fracture Resistance of Metal/Ceramic Interfaces*, edited by M. Rühle, A.G. Evans, M.F. Ashby, and J.P. Hirth, Pergamon Press (1990), Oxford, in press.

## HIGH-RESOLUTION ELECTRON MICROSCOPY STUDIES OF Nb/Al<sub>2</sub>O<sub>3</sub> INTERFACES

J. MAYER \*

*Materials Department, University of California, Santa Barbara, CA 93106, USA*

C.P. FLYNN

*Materials Research Laboratory, University of Illinois at Urbana-Champaign, Urbana, IL 61801, USA*

and

M. RÜHLE \*

*Materials Department, University of California, Santa Barbara, CA 93106, USA*

Received 23 March 1990

Dedicated to Professor J. Heydenreich on the occasion of his 60th birthday

Single-crystal niobium films were grown by molecular beam epitaxy (MBE) on (0001)<sub>S</sub>, (1 $\bar{1}$ 00)<sub>S</sub> and (1 $\bar{2}$ 10)<sub>S</sub> sapphire substrates. Cross-sectional specimens with thicknesses of < 20 nm were prepared so that the Nb/Al<sub>2</sub>O<sub>3</sub> interface could be investigated by high-resolution electron microscopy (HREM). The same unique orientation relationship is obtained for niobium films deposited on differently oriented sapphire substrates: (0001)<sub>S</sub>|| $\langle$ 111 $\rangle$ <sub>Nb</sub> and  $\langle$ 2 $\bar{1}$  $\bar{1}$ 0 $\rangle$ <sub>S</sub>|| $\langle$ 1 $\bar{1}$ 0 $\rangle$ <sub>Nb</sub>. The atomistic structure of the interface was identified by HREM. Defects at or close to the interface were analyzed. A model for the atomic arrangement at the interface will be proposed.

### 1. Introduction

The applications of modern engineering materials such as metals and ceramics often require two different components (metals and ceramics) to be bonded. The resultant interfaces must typically sustain mechanical and/or electrical forces without failure. Consequently, interfaces exert an important, and sometimes controlling, influence on performance in such applications as composites, electronic packaging systems used in information processing, thin-film technology and joining [1,2]. Furthermore, metal/ceramic interfaces play an important role in the internal and external oxidation or reduction of materials. A

knowledge of the atomistic structure of such interfaces is a prerequisite for an understanding of their properties.

Several methods are capable of generating well defined metal/ceramic interfaces. At the most fundamental level, ultra-clean, flat surfaces readily bond at moderate temperatures and pressures [3]. Interfaces can also be produced by internal oxidation of metallic alloys [4], where small oxide particles in different metals (Nb, Pd, Ag, ...) are formed by oxidation of a less noble alloying component such as Al, Cd, etc. Interfaces produced by the internal oxidation process usually show a well defined low-energy crystallographic orientation relationship between the two components and were thus used as model systems. A third method for manufacturing metal/ceramic interfaces is by evaporation of metals onto clean ceramic surfaces. This method allows control over both substrate

\* Present address: Max-Planck-Institut für Metallforschung, Institut für Werkstoffwissenschaft, 7000 Stuttgart 1, Fed. Rep. of Germany.

material/orientation and overlayer composition, and by this, well defined interfaces can be obtained [5]. However, only a few of the possible metal/ceramic combinations have been investigated. One of these is Nb/Al<sub>2</sub>O<sub>3</sub> which has been studied by many different authors [1–20].

Nb/Al<sub>2</sub>O<sub>3</sub> serves as an excellent “model” system since Nb and Al<sub>2</sub>O<sub>3</sub> possess nearly the same thermal expansion coefficients and most thermodynamic quantities (solubility, diffusion data, etc.) are well established for both components. Nb/Al<sub>2</sub>O<sub>3</sub> composites are used in different applications such as Josephson junctions and as components for structural materials. To date, only a few detailed studies have been reported concerning the atomistic structure of Nb/Al<sub>2</sub>O<sub>3</sub> interfaces formed after diffusion bonding [13,14,19], internal oxidation [4, 17,18], and after thin film deposition [15,16]. The studies were all performed by high-resolution electron microscopy (HREM). Orientation relationships (OR) were evaluated from diffraction studies, either by X-rays [6–12,20] or by selected area diffraction (SAD) patterns obtained in a transmission electron microscope (TEM) [4,13–19]. The OR between Nb and Al<sub>2</sub>O<sub>3</sub> is determined by the manufacturing route [16]. While the OR is preset for interfaces prepared by diffusion-bonding, topotaxial or epitaxial OR develops during internal oxidation and epitaxial growth, respectively. During internal oxidation a *topotaxial* relationship forms between Nb and Al<sub>2</sub>O<sub>3</sub> [4,17,18] so that close-packed planes of both systems are parallel to each other, i.e.:

$$(0001)_S \parallel (110)_{Nb} \quad \text{and} \quad [01\bar{1}0]_S \parallel [001]_{Nb}, \quad (1)$$

where

S = sapphire <sup>#1</sup>.

Epitaxial growth of very high quality single-crystalline overlayers of Nb on sapphire has been a subject of recent experiments [5–12]. There exists experimental evidence [6,7] that for most sap-

phire surfaces a unique three-dimensional *epitaxial* relationship between Nb and Al<sub>2</sub>O<sub>3</sub> develops which is given by two sets of zone axes:

$$[0001]_S \parallel [111]_{Nb} \quad \text{and} \quad [10\bar{1}0]_S \parallel [1\bar{2}1]_{Nb}. \quad (2)$$

The latter orientation relationship was determined by reflection high-energy electron diffraction (RHEED) and X-ray diffraction (XRD). Interestingly enough, (001)<sub>Nb</sub> films form on (1 $\bar{1}$ 0)<sub>S</sub>R planes with a distinct deviation from the exact orientation relationship [15,20] at rather low deposition temperatures.

The aim of the present studies was to characterize by HREM the orientation relationships and the atomistic structures of Nb/Al<sub>2</sub>O<sub>3</sub> interfaces formed by MBE growth of Nb layers on sapphire substrates with different orientations. The observations will be compared with results published in the literature.

## 2. Experimental details

The Nb layers were fabricated in a MBE growth chamber equipped with electron beam sources for evaporating refractory metals. The sapphire substrates were parallel to (0001)<sub>S</sub>, (1 $\bar{1}$ 00)<sub>S</sub> and (1 $\bar{2}$ 10)<sub>S</sub>, respectively. The substrates were preheated and cleaned by annealing at ~1500 K for 1 h in a dynamic vacuum of 5 × 10<sup>-8</sup> Pa. The growth of the Nb films was performed while the substrates were heated to 1123 K. Nb is a powerful getter. A combination of ion pumping and cryopumping was therefore employed to maintain a vacuum in the 10<sup>-6</sup> Pa range during crystal growth so that no niobium oxides could form. The crystal surface structure could be monitored with RHEED which showed that the initial diffraction spots elongated with growth into streaks characteristic of an atomically smooth surface. Typical growth rates were one monolayer/s. The films were grown to thicknesses ranging from 100 to 500 nm.

A special technique was used to obtain transmission electron microscopy (TEM) cross-section samples [21] of the Nb film and the Nb/Al<sub>2</sub>O<sub>3</sub> interface. Firstly, the sapphire plates carrying the

<sup>#1</sup> The orientation relationship (OR) between two crystals of different lattice structure is uniquely described by one coinciding plane (in both lattices) and one set of coinciding directions in that plane.

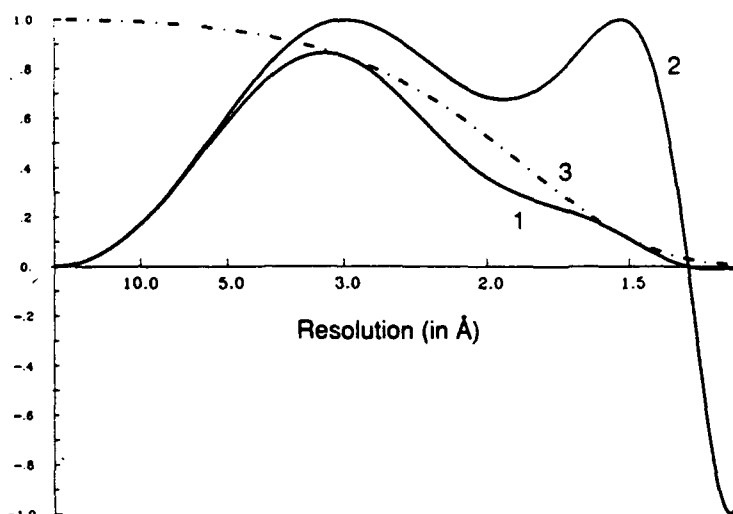


Fig. 1. Actual calculated contrast transfer function (CTF) (1), undamped CTF (2), and damping envelope (3) of the Atomic Resolution Microscope (ARM) at the Center for Electron Microscopy, Berkeley (Hetherington et al. [22]). Operating conditions: voltage 800 kV, defocus -55 nm.

Nb film were glued to another piece of sapphire to protect the thin metal layer. Then these "sandwiches" were cut into stripes and glued into a slit within a cylindrical alumina holder (2.0 mm diameter) which was stiffened by a thin alumina tube (outer diameter 3 mm). Discs were cut from these holders, carefully polished to a thickness of 0.2 mm and dimpled. During ion-milling shields were used to protect the interface and to reduce the effect of the different milling rates of Nb and Al<sub>2</sub>O<sub>3</sub>. This preparation technique resulted in specimens suitable for HREM studies. The foil thickness was less than 20 nm in regions which included the interface. Foil thicknesses down to 5 nm could frequently be obtained.

The HREM studies were performed at the Atomic Resolution Microscope (ARM) at the National Center for Electron Microscopy (NCEM), Berkeley, CA, USA. The microscope was operated at 800 kV [22]. The actual contrast transfer function (CTF) of the instrument is shown in fig. 1. The point-to-point resolution of the instrument is in the range of 0.18 nm. The CTF is mostly determined by the energy spread of the instrument (~15 nm). As a result of the chromatic aberration the CTF is damped as shown in fig. 1.

### 3. Experimental results

#### 3.1. Orientation relationships between Nb and Al<sub>2</sub>O<sub>3</sub>

The OR between Nb and Al<sub>2</sub>O<sub>3</sub> was evaluated from selected area diffraction (SAD) patterns taken from different Nb films on sapphire substrates in three different orientations. For all films a unique OR was evaluated which is characterized by the following coinciding planes:

$$(0001)_S \parallel (111)_{Nb}, \quad (3)$$

and coinciding directions:

$$[2\bar{1}10]_S \parallel [1\bar{1}0]_{Nb} \quad (\text{direction A}), \quad (4)$$

$$[10\bar{1}0]_S \parallel [1\bar{2}1]_{Nb} \quad (\text{direction B}). \quad (5)$$

The same OR was identified by Durbin et al. [6,7], see eq. (2). No deviation from this OR (eqs. (3)–(5)) could be identified within an experimental error of 0.5°.

From crystallographic symmetry arguments the angle between the directions A and B results in 30°. Figs. 2a and 2b illustrate the relative OR of

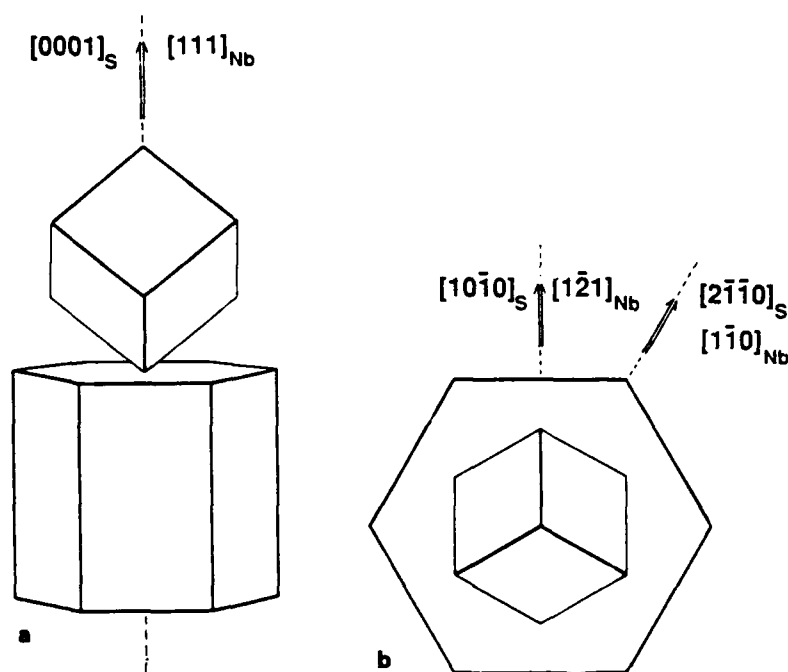


Fig. 2. Orientation relationship between sapphire substrates and niobium overlayers. (a) The three-dimensional orientation relationship  $[0001]_S \parallel [111]_{Nb}$  ( $S = \text{sapphire}$ ) holds for all substrate orientations. (b) Orientation relationship for different directions within the  $(0001)_S \parallel (111)_{Nb}$  plane.

the two crystals. From eq. (3) it follows that the normals on the plane are parallel:

$$[0001]_S \parallel [111]_{Nb}.$$

Thus, the three-fold axes of the two crystals, i.e. Nb and Al<sub>2</sub>O<sub>3</sub> (sapphire), are parallel.

It should be emphasized that the OR described by eqs. (3)–(5) is independently identified at epitaxially grown Nb/Al<sub>2</sub>O<sub>3</sub> interfaces for substrate surfaces parallel to  $(0001)_S$ ,  $(1\bar{1}00)_S$ , and  $(1\bar{2}10)_S$ . The following abbreviations will be used for the three resulting systems:

$$\begin{aligned} (0001)_S &: \text{specimen I,} \\ (1\bar{1}00)_S &: \text{specimen II,} \\ (1\bar{2}10)_S &: \text{specimen III.} \end{aligned} \quad (6)$$

### 3.2. Direct lattice images of the Nb/Al<sub>2</sub>O<sub>3</sub> near-interface regions: $(0001)_S$ substrate

Direct lattice imaging of near-interface regions allows the determination of the atomistic structure

of the interface as well as the analysis of defects associated with the interface, such as misfit dislocations, etc. To obtain interpretable HREM images the electron beam should be incident along high-symmetry directions in both crystals and should be parallel to the plane of the interface. A three-dimensional analysis of the structure requires HREM images taken under different directions of the incident electron beam with respect to the interface orientation. For specimen I (eq. (6),  $(0001)_S$  substrate) these conditions are fulfilled if the electron beam is parallel to direction A and B, respectively (eqs. (4) and (5), see fig. 2b). High-resolution electron micrographs were taken from the same interface in both directions by simply tilting the specimen inside the ARM.

Fig. 3 shows an overview of a large area of a near-interface region. The defocus of the objective lens is slightly more negative ( $\Delta f = -70$  nm) than the Scherzer defocus ( $\Delta f = -55$  nm). At this defocus the atomic distance corresponding to the  $(200)$  planes with  $d = 0.165$  nm becomes clearly visible [23]. Lattice planes can readily be identi-

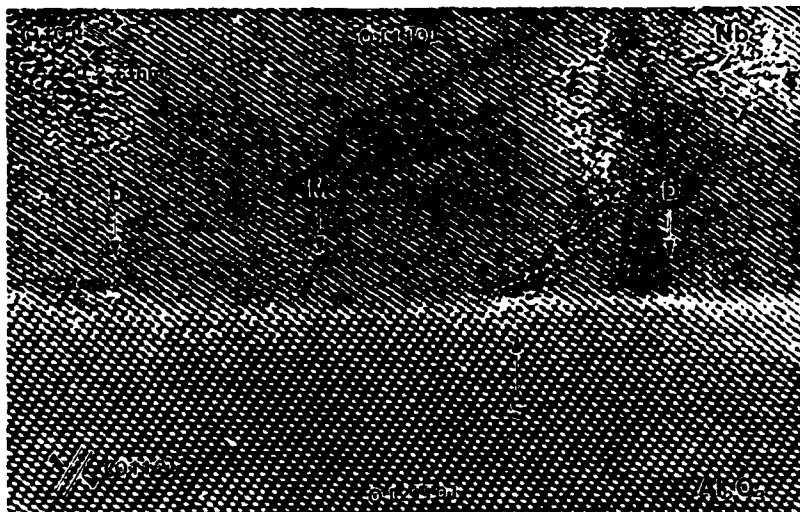


Fig. 3. High-resolution images of a Nb/Al<sub>2</sub>O<sub>3</sub> interface. Direction of incoming electrons parallel to [110]<sub>Nb</sub> and defocus value  $\Delta f = -70$  nm (Scherzer value  $-55$  nm). Lattice planes can clearly be identified in both, sapphire and Nb. Foil thickness  $\sim 10$  nm. At the interface regions of good matching (M) and poor matching (D) alternate; (S) step in the substrate.

fied in Al<sub>2</sub>O<sub>3</sub> and Nb. The foil thicknesses of Nb and Al<sub>2</sub>O<sub>3</sub> are identical. In Nb regions of good matching (M) and poor matching (D) alternate at the interface. Steps can also be identified (S). The

region of good matching (fig. 3, M) is imaged at a higher magnification in fig. 4. Fig. 4a shows the interface with the electron beam parallel to direction A. Nb and Al<sub>2</sub>O<sub>3</sub> possess the same thickness

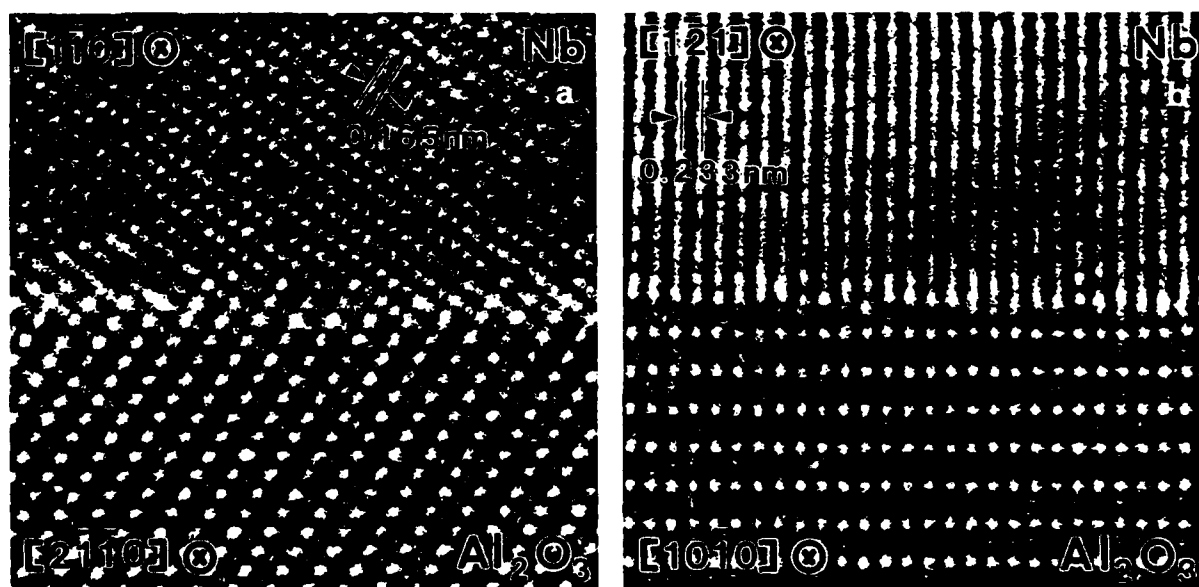


Fig. 4. High-resolution images of Nb/Al<sub>2</sub>O<sub>3</sub> interface. Region of good matching (M). (a) Direction A with [2110]<sub>S</sub> || [110]<sub>Nb</sub>. (b) Direction B with [1010]<sub>S</sub> || [121]<sub>Nb</sub>.

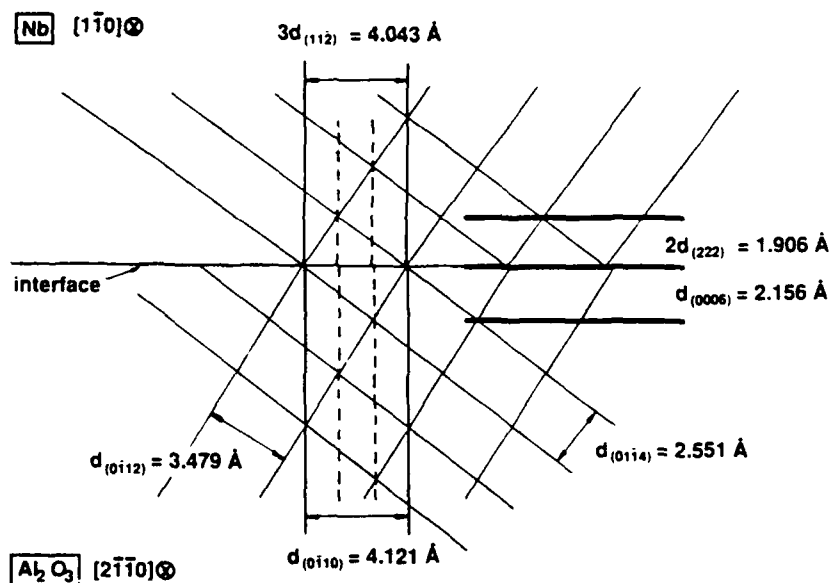


Fig. 5. Schematic drawing of selected lattice planes in Nb and Al<sub>2</sub>O<sub>3</sub> in direction A.

and lattice planes transfer continuously from Nb to Al<sub>2</sub>O<sub>3</sub>. Fig. 4b is a micrograph of the same interface viewed along orientation B. Only (10 $\bar{1}$ )

lattice planes with a spacing of 0.233 nm are visible in the Nb crystal in regions of good matching M. The (222) lattice planes (perpendicular to

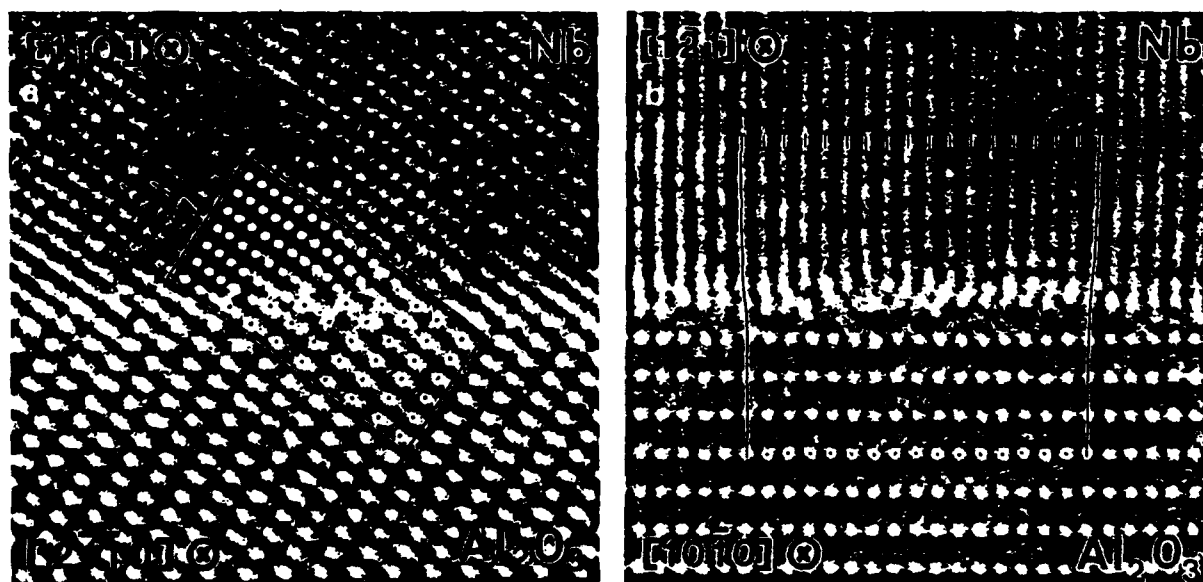


Fig. 6. High-resolution images of Nb/Al<sub>2</sub>O<sub>3</sub>, region of poor matching. A misfit dislocation forms with no stand-off distance. (a) Direction A; the core of the misfit dislocation can readily be identified. (b) Direction B; the core of the dislocation line is inclined with respect to the electron beam. The region of no matching of corresponding lattice planes is marked. This region corresponds to the projection width of the additional lattice plane.

(10 $\bar{1}$ ) possess a spacing of 0.095 nm which is beyond the resolution limit and information limit of the ARM. Therefore only (10 $\bar{1}$ ) lattice fringes are visible. In both orientations (figs. 4a and 4b) a perfect match of the Nb and Al<sub>2</sub>O<sub>3</sub> lattice at the interface is visible. Fig. 5 shows schematically several lattice planes in Nb and Al<sub>2</sub>O<sub>3</sub>, respectively, for an axis of the incident electron beam parallel to direction A. The lattice mismatch of the (0 $\bar{1}$ 10)<sub>S</sub> and (11 $\bar{2}$ )<sub>Nb</sub> planes perpendicular to the interface is 1.9%. The Nb lattice possesses the smaller spacing. The (0006)<sub>S</sub> and (222)<sub>Nb</sub> planes are parallel to the interface and possess a lattice mismatch of 11.9%. This larger mismatch is significant if steps are present at the interface, see section 3.4.

### 3.3. Localized misfit dislocations at the interface: (0001)<sub>S</sub> substrate

The misfit of 1.9% between the (11 $\bar{2}$ )<sub>Nb</sub> and (0 $\bar{1}$ 10)<sub>S</sub> planes perpendicular to the interface is accommodated by localized defects (misfit dislocations) in regions of poor matching (fig. 3).

These localized misfit dislocations at the interface are spaced periodically, about one every 50 lattice planes (fig. 3). A higher magnification of region D of fig. 3 is shown in fig. 6. Fig. 6a represents the images parallel to direction A. A

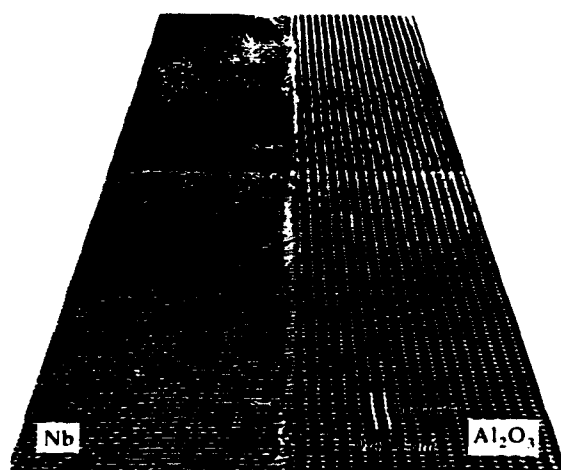


Fig. 7. "Scheimpflug image" [25] of HREM images in direction B (0001)<sub>S</sub> substrate. Steps can be observed (S). The step height corresponds to the (0006) plane distance.

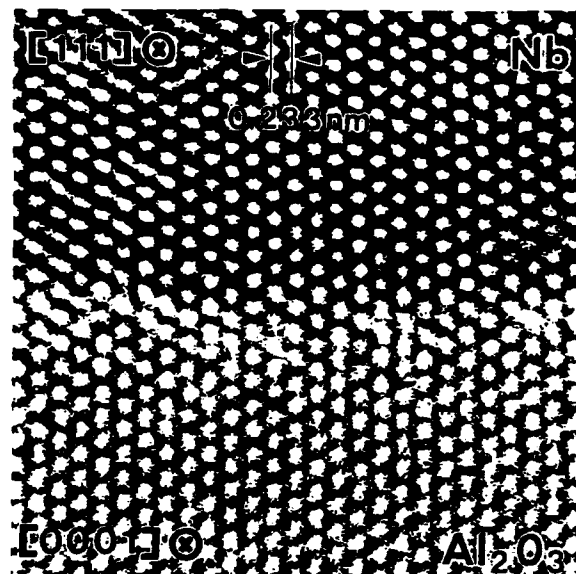


Fig. 8. High-resolution image of Nb/Al<sub>2</sub>O<sub>3</sub> interface; specimen II: (1 $\bar{1}$ 00)<sub>S</sub> || (2 $\bar{1}$  $\bar{1}$ )<sub>Nb</sub>. Direction of electron beam parallel to [0001]<sub>S</sub> || [111]<sub>Nb</sub>. Good matching of Nb and Al<sub>2</sub>O<sub>3</sub> is observed at the interface.

misfit dislocation can clearly be identified. The Burgers vector is  $\frac{1}{2}[110]_{Nb}$ . No "stand-off" distance [4,17,18,24] of the misfit dislocation can be identified.

The projection of the extra plane of the misfit dislocation is parallel to the electron beam in direction A. For direction B (fig. 6b) the extra Nb plane is inclined at an angle of 30°. There is no fit of corresponding planes in Nb and Al<sub>2</sub>O<sub>3</sub> along the projection of the inclined plane of the misfit dislocation which is clearly visible in fig. 7b. The projected length, x, can be measured:

$$x = (17 \pm 2) d_{110} \quad (d_{110} = 0.233 \text{ nm}),$$

and with the known tilt angle the thickness of the foil, t, can be evaluated:

$$t = 8.0 \pm 1.0 \text{ nm}.$$

### 3.4. Steps at the interface: (0001)<sub>S</sub> substrate

The sapphire surface will usually not be atomically flat over large distances. Steps are expected if, e.g., small deviations exist between the surface plane and the (0001)<sub>S</sub> basal plane of sapphire

prior to thin film evaporation. Such surface steps can be recognized at the interface (figs. 3 and 7). Careful inspection (especially on micrographs imaged under a grazing angle, "Scheimpflug technique" [25]) revealed that the step height of the sapphire is always a multiple of the distance of the O<sup>2-</sup> layers within the Al<sub>2</sub>O<sub>3</sub> structure parallel to (0001)<sub>S</sub>. This distance corresponds to (0006)<sub>S</sub> planes with  $d = 0.2165$  nm. The corresponding lattice spacing in Nb is  $d_{111} = 0.1906$  nm and is 11.9% smaller than the O<sup>2-</sup> spacing. Due to this mismatch (fig. 5), the Nb lattice is distorted adjacent to steps. The recognizable distortion extends up to about 10 nm into the Nb film.

### 3.5. Nb overlayers on (1 $\bar{1}00$ )<sub>S</sub> and (1 $\bar{2}10$ )<sub>S</sub> substrates

SAD studies on Nb films deposited on (1 $\bar{1}00$ )<sub>S</sub> and (1 $\bar{2}10$ )<sub>S</sub> substrates (specimens II and III) revealed the same unique orientation relationship as described in eqs. (3) and (4). Fig. 8 shows a micrograph of specimen II ((1 $\bar{1}00$ )<sub>S</sub> || (2 $\bar{1}\bar{1}$ )<sub>Nb</sub>) with the electron beam parallel to [0001]<sub>S</sub> || [111]<sub>Nb</sub>. Well defined atom rows and lattice planes can be identified. The thickness of both, Nb and Al<sub>2</sub>O<sub>3</sub> is the same at the interface. Good matching is reached in most areas of the film. The flatness of the (1 $\bar{1}00$ )<sub>S</sub> substrates for this orientation is not as



Fig. 9. High-resolution micrograph imaged with "Scheimpflug" technique. (1 $\bar{1}00$ )<sub>S</sub> || (2 $\bar{1}\bar{1}$ )<sub>Nb</sub>, electron beam parallel to [0001]<sub>S</sub> || [111]<sub>Nb</sub>. Pyramidal elevations are clearly visible.

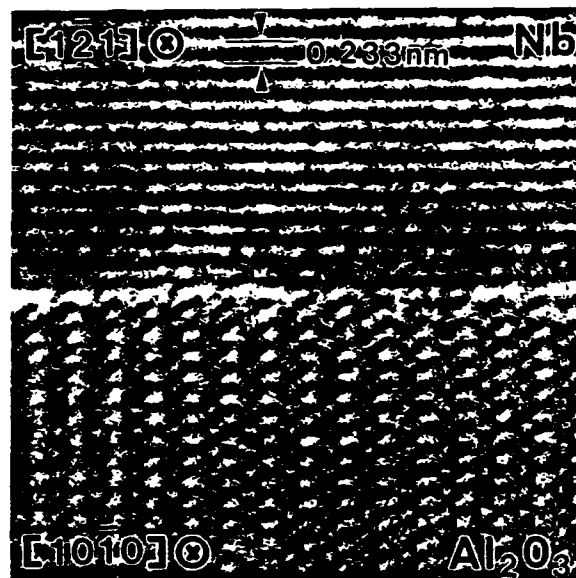


Fig. 10. High-resolution image of Nb/Al<sub>2</sub>O<sub>3</sub> interface; specimen III: (1 $\bar{2}10$ )<sub>S</sub> || (10 $\bar{1}$ )<sub>Nb</sub>. Direction of electron beam parallel to [10 $\bar{1}0$ ]<sub>S</sub> || [1 $\bar{2}1$ ]<sub>Nb</sub>.

good as the corresponding (0001)<sub>S</sub> surfaces. Pyramidal elevations can be seen (fig. 9) and these elevations cause strong distortions in the Nb lattice. The distortion reaches about 10 nm into the Nb film.

For specimen III the (10 $\bar{1}$ )<sub>Nb</sub> planes are parallel to (1 $\bar{2}10$ )<sub>S</sub> planes of the substrate surface. In fig. 10 a micrograph is shown with the direction of the incoming electron beam parallel to [10 $\bar{1}0$ ]<sub>S</sub> || [1 $\bar{2}1$ ]<sub>Nb</sub>. The interface is imaged along the same set of zone axes as specimen I in orientation B (eq. (5)), with the only difference that the interface plane lies perpendicular to the interface obtained in specimen I (see fig. 4b). This illustrates that the same OR is obtained for different substrate orientations. In fig. 10 only (10 $\bar{1}$ ) lattice fringes of Nb can be identified since the lattice spacing of (222)<sub>Nb</sub> planes is beyond the resolution limit of the microscope. The (222)<sub>Nb</sub> planes should be perpendicular to the interface. More detailed experimental studies are required for a full understanding of the interface.

## 4. Discussion

### 4.1. Orientation relationships

The observed orientation relationship (OR) for Nb films on differently oriented sapphire substrates is equivalent to results described in the literature [5–7]. The three-dimensional orientation relationship between Nb and Al<sub>2</sub>O<sub>3</sub> has been confirmed for the three different orientations of the sapphire substrates: (0001)<sub>S</sub> || (111)<sub>Nb</sub> and [10 $\bar{1}$ 0]<sub>S</sub> || [1 $\bar{2}$ 1]<sub>Nb</sub>. Knowles et al. [15] demonstrated by HREM that the same OR holds for (001) niobium films deposited epitaxially on (1 $\bar{1}$ 02)<sub>R</sub> planes of sapphire. The characteristic misorientation from the “three-dimensional OR” is caused by small locally misoriented regions in the immediate vicinity of the Nb/Al<sub>2</sub>O<sub>3</sub> interface.

The observed OR and hence the arrangements of atoms at the interface is different from the OR obtained at Nb/Al<sub>2</sub>O<sub>3</sub> interfaces in internally oxidized NbAl alloys. For both systems Al<sub>2</sub>O<sub>3</sub> is bound by an oxygen layer of the basal plane [12,13,15]. However, different Nb planes terminate at the interface. Typically, close-packed (110) planes juxtapose close-packed planes of Al<sub>2</sub>O<sub>3</sub> as interfaces formed by internal oxidation. The OR is symmetry-dictated for epitaxial growth. It is not obvious which interface of the different ORs possesses the lower interfacial energy. Further experimental studies may answer this question.

### 4.2. Film formation

Qualitatively the Nb film formation on (0001)<sub>S</sub> substrates (specimen I) could be described as follows. The sapphire substrate was annealed at  $5 \times 10^{-8}$  Pa at 1500 K in a dynamic vacuum. The annealing leads to a reconstruction of the  $\alpha$ -Al<sub>2</sub>O<sub>3</sub> surface resulting in a  $(\sqrt{31} \times \sqrt{31})\text{R} \pm 9^\circ$  structure [26–28]. At the surface the Al:O ratio is  $\approx 1:1$ , thus the sapphire is not stoichiometric at the surface. The RHEED studies performed at  $\alpha$ -Al<sub>2</sub>O<sub>3</sub> surfaces prior to deposition of the Nb film indicate that a similar reconstruction is present. In addition, atomistic steps (facets) exist at the surface of sapphire due to small deviations between the surface orientation and the (0001)<sub>S</sub>

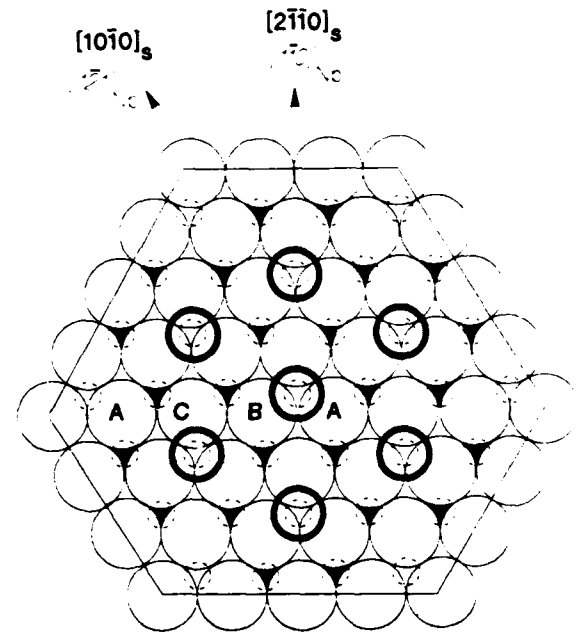


Fig. 11. Schematic drawing of an unreconstructed (0001)<sub>S</sub> basal surface. O<sup>2-</sup> ions: light large circles. Al<sup>3+</sup>: dark sections of small circles, Nb atoms: bold medium-sized circles. It is assumed that the O<sup>2-</sup> ions form the outermost layer. The Nb atoms of the first Nb layer are positioned above the empty sites of the first Al<sup>3+</sup> layer which lies immediately next to the outermost O<sup>2-</sup> layer.

basal plane. Those steps may act as nucleation centers for the Nb film. The growth conditions are selected such that two-dimensional crystal growth occurs [5]. The reconstructed, Al-rich surface still possesses three-fold symmetry with characteristic distances equivalent to atomistic distances of (111)<sub>Nb</sub> planes. For symmetry reasons it is expected that the first deposited monolayer of Nb atoms has an OR which is dictated by the symmetry of the sapphire surface leading (0001) || (111)<sub>Nb</sub>. No twins could be identified in the (nearly) perfect Nb film. It must be assumed that a unique atomistic relationship exists between the sapphire surface and the monoatomic Nb layer. There exists only one set of Nb atom positions on the unreconstructed sapphire surface which leads to a twin-free film (fig. 11). Nb atoms must be located on the terminating O<sup>2-</sup>-layer of sapphire on top of “empty sites” (fig. 11). A quantitative evaluation of the HREM images should verify this hypothesis.

### 4.3. Misfit dislocations

The formation of the "core" of the misfit dislocations can be explained using the Frank-Van der Merwe model [29,30]. Subsequent Nb layers bond to the first layer by metallic bonding building up the misfit dislocation nucleated at the interface. This model may explain the growth on (0001)<sub>s</sub> plane sapphire. It is, however, difficult to explain the (general) three-dimensional orientation relationship between Nb and Al<sub>2</sub>O<sub>3</sub> which develops also on other sapphire surfaces.

A careful inspection of HREM images taken under different focusing conditions of regions very close to the interface reveals that no reconstruction of sapphire close to the interface is recognizable. It must be assumed that the excess Al atoms of the reconstructed (0001) surface [26-28] diffuse into the Nb, which has a sufficiently high solubility for Al. Quantitative evaluation of the high-resolution images will support this qualitative statement.

The misfit dislocations observed in MBE-grown Nb films do not show a "stand-off" which was observed at interfaces formed by internal oxidation or diffusion bonding [4,17,18]. The localization of the inserted plane is well defined (fig. 6a) and a perfect match of the Nb atoms on the sapphire lattice is obtained within 0.5 nm on either side of the dislocation. Since the deposition of the Nb film was performed at much lower temperatures than either the diffusion bonding or the internal oxidation, this geometrical arrangement (fig. 6a) of the misfit dislocations might not be thermally stable. The dislocations could climb from the interface to a stable stand-off distance if the samples are heat-treated or deposited at higher temperature. Such experiments would also show if the OR observed in our studies is thermally stable or if it is only formed at the given growth conditions due to the kinetics of the epitaxial growth process.

The Nb overlayers shows an extremely high perfection which is typical for MBE-grown films. However, stresses generated by unevenness of the substrate may extend up to 200 nm into the film and influence its properties. This interfacial

roughness may also play a role in dislocation nucleation when the film is stressed.

### Acknowledgements

This work was supported in part by DARPA through the University Research Initiative Program at UCSB, ONR Contract Number N00014-86-K 0753 (J.M.) and by the Department of Energy under Contracts DE-FG03-88ER45351 (M.R.) and DE-AC02-76ER01198 (C.P.F.) and by the Bundesministerium für Forschung und Technologie (BMFT) Contract Number NTS 02300. The authors gratefully acknowledge the use of the Atomic Resolution Microscope at the National Center for Electron Microscopy in Berkeley, CA, USA.

### References

- [1] M. Rühle, A.G. Evans, M.F. Ashby and J.P. Hirth, Eds., *Structure, Chemistry and Fracture Resistance of Metal/Ceramic Interfaces* (Pergamon Press, New York, 1990).
- [2] M. Rühle and A.G. Evans, *J. Mater. Sci. Eng. A* 107 (1989) 187.
- [3] H. Fischmeister, W. Mader, B. Gibbesch and G. Ellsner, *Mater. Res. Soc. Symp. Proc.* 122 (1988) 529.
- [4] W. Mader, *Z. Metallk.* 80 (1989) 139.
- [5] C.P. Flynn, in: *Proc. Acta/Scripta Conf. on Structure, Chemistry and Fracture Resistance of Metal/Ceramic Interfaces*, Eds. M. Rühle, A.G. Evans, M.F. Ashby and J.P. Hirth (Pergamon Press, New York, 1990) in press.
- [6] S.M. Durbin, J.E. Cunningham, M.E. Mochel and C.P. Flynn, *J. Phys. F* 11 (1981) L223.
- [7] S.M. Durbin, J.E. Cunningham and C.P. Flynn, *J. Phys. F* 12 (1982) L75.
- [8] Y. Igarashi and M. Kanayama, *J. Appl. Phys.* 57 (1985) 849.
- [9] S.A. Wolf, S.B. Quadri, J.H. Claassen, T.L. Francavillo and B.J. Dalrymple, *J. Vac. Sci. Technol. A* 4 (1986) 524.
- [10] Y. Nishihata, N. Nakayama, H. Kato, N. Sano and H. Terauchi, *J. Appl. Phys.* 60 (1986) 3523.
- [11] F.J. Camelas, H. He and R. Clarke, *Phys. Rev. B* 38 (1988) 6334.
- [12] J.H. Claassen, S.A. Wolf, S.B. Quadri and C.D. Jones, *J. Cryst. Growth* 81 (1987) 557.
- [13] M. Florjancic, W. Mader, M. Rühle and M. Turwitt, *J. Phys. (Paris)* 46 (1985) C4-129.
- [14] W. Mader and M. Rühle, *Acta Met.* 37 (1989) 853.

- [15] K.M. Knowles, K.B. Alexander, R.E. Somekh and W.M. Stobbs, in: EMAG 87, Inst. Phys. Conf. Ser. 90 (1987) 245.
- [16] J. Mayer, W. Mader, F.O. Phillipp, C.P. Flynn and M. Rühle, in: EMAG 89, Inst. Phys. Conf. Ser. 98 (1989) 349.
- [17] W. Mader, Mater. Res. Soc. Symp. Proc. 82 (1987) 403.
- [18] M. Kuwabara, J.C.H. Spence and M. Rühle, J. Mater. Res. 4 (1989) 972.
- [19] D. Knauss and W. Mader, unpublished research.
- [20] D.B. McWhan, Mater. Res. Soc. Symp. 35 (1985) 493.
- [21] A. Strecker, J. Mayer and M. Rühle, to be published.
- [22] C.J.D. Hetherington, E.C. Nelson, K.H. Westmacott, R. Gronsky and G. Thomas, Mater. Res. Soc. Symp. Proc. 139 (1989) 277.
- [23] J.C.H. Spence, Experimental High Resolution Electron Microscopy (Clarendon Press, Oxford, 1981).
- [24] S.K. Kamat, J.P. Hirth and B. Carnahan, Mater. Res. Soc. Symp. Proc. 103 (1988) 55.
- [25] L. Bitzek, W.E. Wunderlich and W. Mader, Prakt. Metall. 25 (1988) 384.
- [26] T.M. French and G.A. Somorjai, J. Phys. Chem. 74 (1970) 2409.
- [27] C.C. Chang, J. Appl. Phys. 33 (1968) 5570.
- [28] M. Arbab, G.G. Chottimer and R.W. Hoffmann, Mater. Res. Soc. Symp. Proc. 153 (1989) 63.
- [29] F.C. Frank and J.H. van der Merwe, Proc. Roy. Soc. (London) A 198 (1949) 205.
- [30] J.W. Matthews, in: Epitaxial Growth, Part B, Ed. J.W. Matthews (Academic Press, New York, 1975) p. 559.

## STRUCTURE AND DEFECTS OF MBE GROWN Nb-Al<sub>2</sub>O<sub>3</sub> INTERFACES

J. MAYER,<sup>1</sup> G. GUTEKUNST,<sup>1</sup> G. MÖBUS,<sup>1</sup> J. DURA,<sup>2</sup> C. P. FLYNN<sup>2</sup> and M. RÜHLE<sup>1</sup>

<sup>1</sup>Max-Planck-Institut für Metallforschung, Institut für Werkstoffwissenschaft, Seestr. 92, D-7000 Stuttgart 1, Germany and <sup>2</sup>University of Illinois at Urbana-Champaign, Materials Research Laboratory, Urbana, IL 61801, U.S.A.

**Abstract**—Single crystal niobium films were grown by Molecular Beam Epitaxy (MBE) on (0001)<sub>s</sub> sapphire substrates. Cross-sectional and plan-view specimens of the films were prepared so that the Nb-Al<sub>2</sub>O<sub>3</sub> interface could be investigated by conventional transmission electron microscopy (CTEM) and high-resolution electron microscopy (HREM). The atomistic structure of the interface was identified by HREM. Regions of good matching and regions containing structural defects alternate at the interface. The defects can be described as misfit dislocations with no "stand-off" from the interface. The spacing of the defects corresponds to the 1.9% mismatch between the two lattices. In regions of good matching a fixed translational state between both lattices is established, which could be determined. Image simulations constructed with this translational state were in good agreement with experiment. In plan-view, periodic arrays of fringes were observed. These fringes are formed by a superposition of moiré fringes and dislocation contrast. Weak-beam techniques were used to separate these two contributions.

**Résumé**—On élabore des films monocristallins de Nb par épitaxie par jet moléculaire (EJM) sur des substrats de saphir (001)<sub>s</sub>. Des échantillons en section droite et en section plane sont préparés de telle façon que l'interface Nb/Al<sub>2</sub>O<sub>3</sub> puisse être observée par microscopie électronique en transmission classique et en haute résolution. La structure atomique de l'interface est identifiée en haute résolution. Des régions de bon accord et des régions contenant des défauts de structure alternent à l'interface. Les défauts peuvent être décrits comme des dislocations de désaccord qui ne s'écartent pas de l'interface. L'espacement des défauts correspond au désaccord de 1,9% entre les deux réseaux. Dans les régions de bon accord un état de translation fixe entre les deux réseaux est établi et peut être déterminé. Des simulations d'images construites avec cet état de translation sont en bon accord avec l'expérience. Dans les vues planes, des arrangements périodiques de franges sont observés. Ces franges sont formées par une superposition de franges de moiré et de contraste de dislocations. Les techniques de faisceau faible sont utilisées pour distinguer ces deux cas.

**Zusammenfassung**—Einkristalline Niobfilme werden mit der Molekularstrahlepitaxie auf (0001)<sub>s</sub>-Saphir-Substrate gezüchtet. Querschnitts- und Aufsichtspröben der Filme werden hergestellt, um die Nb/Al<sub>2</sub>O<sub>3</sub>-Grenzfläche mit hochauflösender und konventioneller Elektronenmikroskopie untersuchen zu können. Die hochauflösende Abbildung zeigt, daß sich Bereiche guter Passung und Bereiche mit strukturellen Defekten an der Grenzfläche abwechseln. Die Defekte können als Fehlpassungsversetzungen 'ohne Abstand zur Grenzfläche' beschrieben werden. Der Abstand der Defekte entspricht der Fehlpassung von 1,9% zwischen den beiden Gittern. In Bereichen guter Passung besteht eine feste Translation, die bestimmt werden konnte. Bildsimulation, die diese Translation berücksichtigen, stimmen mit dem Experiment gut überein. In Aufsichtspröben beobachtet man periodische Anordnungen von Streifungen. Diese Streifungen werden verursacht von einer Überlagerung aus Moiré-Streifen und Versetzungscontrast. Mit der Weak-beam-Technik werden diese beiden Beiträge getrennt.

### INTRODUCTION

A knowledge of the atomistic structure of metal-ceramic interfaces is a prerequisite for understanding their properties [1]. Determination of the atomistic structure of an interface by high resolution electron microscopy (HREM) imposes certain geometrical requirements on the interface: the interface has to be planar and a low indexed orientation relationship with parallel lattice planes must exist.

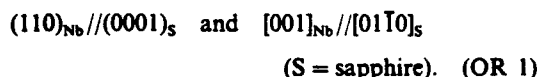
The three most important methods for generating well defined metal-ceramic interfaces are: bonding at moderate temperatures and pressures [2], internal

oxidation of metallic alloys [3], and evaporation of metals onto clean ceramic surfaces [4]. While all three methods result in well defined interfaces, the latter method is the only one which allows the metal to grow in a low-energy structural relationship with respect to the ceramic substrate.

Nb-Al<sub>2</sub>O<sub>3</sub> serves as an excellent "model" system since Nb and Al<sub>2</sub>O<sub>3</sub> possess nearly the same thermal expansion coefficients and no chemical reactions occur at the interface. Several HREM studies have been reported concerning the atomistic structure of Nb-Al<sub>2</sub>O<sub>3</sub> interfaces formed after diffusion bonding [5] and internal oxidation [3]. By comparing the

results from these studies with the results of our present investigations, further insight in the growth of metal-ceramic interfaces can be gained.

The orientation relationship (OR) between Nb and Al<sub>2</sub>O<sub>3</sub> is determined by the manufacturing route [6]. While the OR is preset for interfaces prepared by diffusion-bonding, topotaxial or epitaxial ORs develop during internal oxidation and epitaxial growth, respectively. A *topotaxial* relationship forms during internal oxidation [3] so that close-packed planes of Nb and Al<sub>2</sub>O<sub>3</sub> are parallel to each other at the interface, i.e.



The characterization of epitaxially grown very high quality single-crystalline overlayers of Nb on sapphire has been a subject of recent experiments [4, 7]. In these systems an *epitaxial* OR was determined with a (111)<sub>Nb</sub> plane parallel to the basal plane of the sapphire [4, 7]



The same well-defined OR is also established for various other substrate orientations, namely the (1 $\bar{1}$ 00)<sub>S</sub>, (1 $\bar{2}$ 10)<sub>S</sub> and (1 $\bar{1}$ 02)<sub>S</sub> planes [7]. This suggests that there is a unique three-dimensional way of interconnecting the lattices of both materials which dictates the OR formed during epitaxial growth.

In previous studies [7] we have obtained an understanding of the atomistic matching of the two lattices at the interface, including the occurrence of defects and steps at the interface. The misfit between the two lattices is accommodated by localized defects leading to extended regions of good matching between the defects. The aim of the present investigations was to characterize the atomistic structure of the interface in the areas of good matching by quantitative HREM. Nb films grown on basal plane (0001)<sub>S</sub> substrates were used because of the low mismatch of 1.9% in all directions parallel to the interface. Comparison of high-resolution micrographs with simulated images resulted in a determination of the translational state of the two lattices in the areas of good matching, and of the chemistry of the terminating plane of the Al<sub>2</sub>O<sub>3</sub>.

We also report on the results of our studies on the 2-dimensional arrangement of the misfit dislocations by conventional TEM in plan-view.

## EXPERIMENTAL

The Nb layers were fabricated in an MBE growth chamber as described elsewhere [4, 7]. Typical growth rates were one monolayer/s. The films were grown to thicknesses ranging from 10 to 500 nm. For the TEM specimen preparation a special technique was used which will be described in [8].

Conventional TEM studies were performed in a JEOL 200 CX transmission electron microscope. The HREM studies were performed at the Atomic Resolution Microscope (ARM) at the National Center for Electron Microscopy (NCEM), Berkeley, California, U.S.A. The microscope was operated at 800 kV. The point-to-point resolution of the instrument is in the range of 0.17 nm. Image simulations were performed using Stadelmann's program [9]. The experimental and simulated images were compared by inspection.

## EXPERIMENTAL RESULTS

### (a) HREM of the interface

Quantitative HREM of interfaces requires that the electron beam is incident along high symmetry directions in both crystals. Furthermore, the electron beam has to be parallel to the plane of the interface. For OR 2 these conditions are fulfilled along two sets of zone axes, i.e. if the electron beam is incident along [1 $\bar{1}$ 0]<sub>Nb</sub>//[2 $\bar{1}\bar{1}$ 0]<sub>S</sub> (direction A) or along [1 $\bar{2}$ 1]<sub>Nb</sub>//[10 $\bar{1}$ 0]<sub>S</sub> (direction B) [7]. High resolution electron micrographs were taken from the same interface area in both directions A and B by simply tilting the specimen inside the ARM.

Figure 1(a) shows the interface with the electron beam parallel to direction A. Lattice planes transfer continuously from Nb to Al<sub>2</sub>O<sub>3</sub>. Figure 1(b) is a micrograph of the same interface area viewed along orientation B. Only (10 $\bar{1}$ )<sub>Nb</sub> lattice planes with a spacing of 0.233 nm are visible in the Nb crystal. The (222) lattice planes [perpendicular to (10 $\bar{1}$ )<sub>Nb</sub>] possess a spacing of 0.095 nm which is beyond the information limit of the ARM. In both orientations [Fig. 1(a, b)] a perfect match of the Nb and Al<sub>2</sub>O<sub>3</sub> lattice at the interface is visible. The mismatch of the (0 $\bar{1}$ 10)<sub>S</sub> and (11 $\bar{2}$ )<sub>Nb</sub> planes which are perpendicular to the interface is only ~1.9% and this misfit is accommodated by localized defects (misfit dislocations) in the regions of poor matching (Fig. 2). This allows the Nb lattice in between these defects to expand slightly along the interface (the Nb lattice possesses the smaller lattice plane spacing) resulting in extended regions of perfect matching. The expansion of the lattice plane spacings parallel to the interface is limited to regions close to the interface. The lattice planes of the Nb, especially near the misfit dislocations, are bent resulting in a continuous transition to the undistorted Nb lattice further away from the interface (this can be seen by viewing Fig. 2 under grazing incidence). No dislocations or lattice distortions could be seen in the Al<sub>2</sub>O<sub>3</sub> lattice. The misfit dislocations in the Nb do not show any "stand-off" distance from the interface.

In HREM images only projections of the foil on its exit surface can be analyzed. Dislocations can thus only be identified if viewed edge on, i.e. if the dislocation line lies parallel to the beam. The dislocation shown in Fig. 2 fulfils this requirement and by

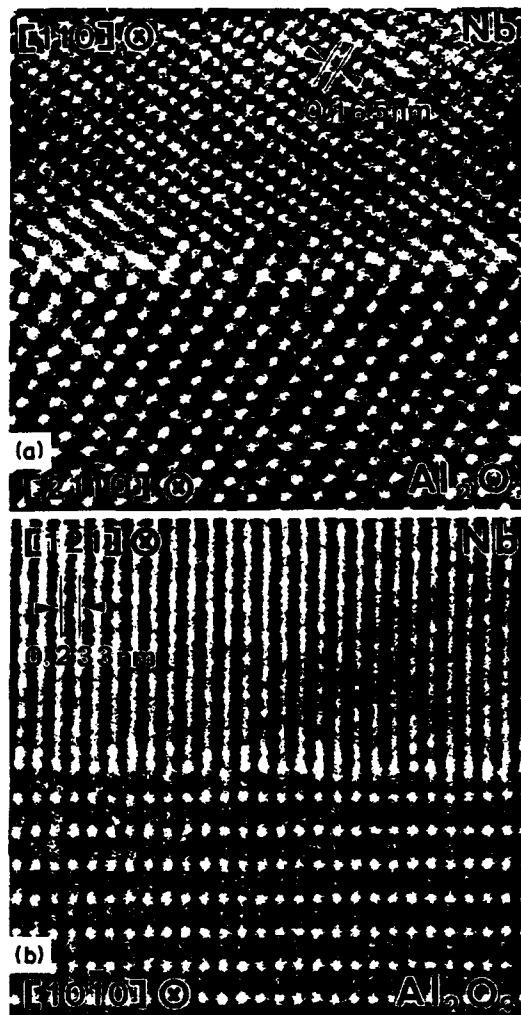


Fig. 1. High resolution image of the Nb-Al<sub>2</sub>O<sub>3</sub> interface. The images were taken in a region of good matching along two different sets of zone axes. (a) Direction A with  $[1\bar{1}0]_{\text{Nb}}//[2\bar{1}1]_{\text{Al}_2\text{O}_3}$ . (b) Direction B with  $[1\bar{2}1]_{\text{Nb}}//[10\bar{1}]_{\text{Al}_2\text{O}_3}$ . Both images were obtained from the same area by tilting the sample in the microscope. The tilt angle was 30°. Note that the contrast fringes cross the interface continuously and without steps.

making use of the continuous transition of lattice planes between the niobium and the sapphire a Burgers circuit can be performed. A projected Burgers vector of  $b = 1/2[11\bar{1}]_{\text{Nb}}$  was determined. Since only the projection can be seen in the HREM image this does not preclude a possible screw component parallel to the viewing direction.

#### (b) CTEM of plan-view specimens

While in HREM individual dislocations can be viewed edge-on, imaging of a two-dimensional array of dislocations lying parallel to an interface requires that this interface be inspected in plan-view. The dislocations can then be imaged with conventional TEM techniques.

In the case of our system two difficulties arise: (1) All the low-indexed reflections of the Nb which

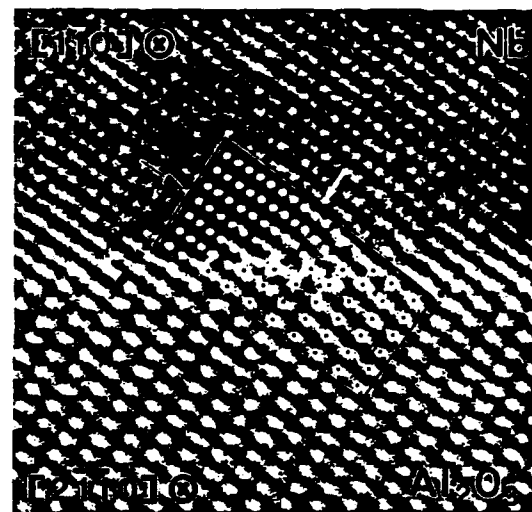


Fig. 2. High resolution image of a region of poor matching. A misfit dislocation forms with no stand-off distance from the interface. The core of the misfit dislocation can readily be identified, as outlined in the picture. The arrows indicate inserted planes in the Nb; black and white arrow: additional (110) plane, white arrow: additional (002) plane.

can be used to image the dislocations are very close to corresponding reflections of the sapphire (the distances between the reflections are given by the 1.9% misfit). In bright-field or dark-field images this causes strong moiré contrast with the same periodicity as the misfit dislocations. (2) In order to obtain strong diffraction contrast of the dislocations (utilising dark field imaging techniques) bent lattice planes have to be present in the vicinity of the dislocation core. In our system the core of the misfit dislocations is located directly at the interface. The bent lattice planes around the dislocation core terminate abruptly at the interface and additional relaxations have to be expected in the niobium at the interface to the rigid sapphire lattice. It is thus not clear whether the simple  $g \cdot b$  criterion which is used to select possible imaging conditions for bulk dislocations is also valid in the case of misfit dislocations without "stand-off".

A schematic drawing of the atomistic structure of a  $1/2[11\bar{1}]_{\text{Nb}}$  dislocation in bulk Nb is shown in Fig. 3. The model is purely geometrical and relaxations in the vicinity of the dislocation core have not been taken into account. The dislocation core consists of three inserted (22 $\bar{2}$ ) planes. The position of the (111) plane forming the terminating plane at the interface is indicated in Fig. 3. In the experimental image (Fig. 2) it is virtually impossible to identify geometrically the three additional (22 $\bar{2}$ ) planes forming the dislocation core. However, if viewed along the arrowed directions an additional (110) plane (corresponding to a Burgers vector of  $1/2[110]_{\text{Nb}}$ ) and an additional (002) plane (corresponding to a Burgers vector of  $1/2[001]_{\text{Nb}}$ ) can clearly be identified in both the experimental image (Fig. 2) and the schematical

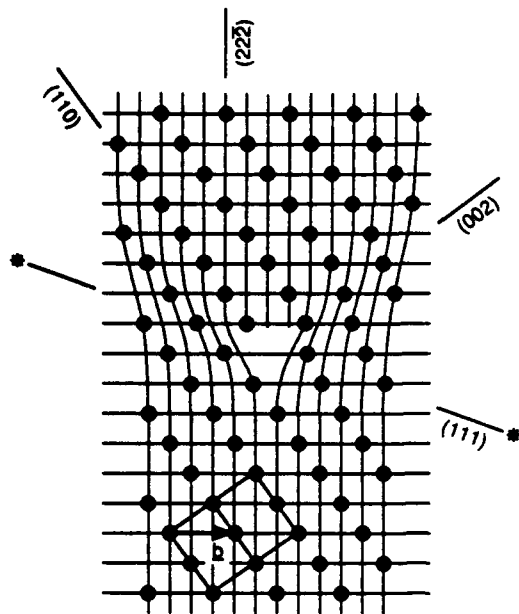


Fig. 3. Schematic drawing of a  $1/2 [111]$  dislocation in bulk Nb. Relaxations of the three inserted  $(22\bar{2})$  planes have not been taken into account. One unit-cell including the Burgers-vector is outlined. The position of the terminating  $(111)$  plane at the Nb-sapphire interface is marked ( $\ast$ ).

drawing (Fig. 3). This description is equivalent to decomposing the Burgers vector into two components according to:  $1/2[11\bar{1}]_{\text{Nb}} = 1/2[110]_{\text{Nb}} + 1/2[00\bar{1}]_{\text{Nb}}$ . Especially for the  $1/2[110]_{\text{Nb}}$  component strong bending of the lattice planes and a strong localization of the dislocation core can be recognized in the HREM image (Fig. 2).

Bright field images showing strong moiré contrast are depicted in Fig. 4(a-c). The images were taken under dynamical scattering conditions which were obtained by tilting only slightly away from the  $[111]$  zone axis so that a  $110$  systematic row of reflections was excited. The tilt angle was about  $10^\circ$  and the same tilt was applied in three different directions related by symmetry. In these projections the dislocation lines should be inclined by  $30^\circ$  with respect to the moiré fringes. However, under the given imaging conditions the contrast of the dislocations is almost extinct and the dislocations cannot be seen due to the strong moiré contrast.

The diffraction contrast caused by the dislocations and the moiré fringes can only be distinguished by weak-beam imaging [10]. In weak-beam images diffraction contrast is caused by a specific strain component [11]. The image obtained from a dislocation is narrower (1–2 nm) because the imaging conditions are such, that only areas close to the dislocation core, where lattice planes are strongly bent, contribute to the image. As stated above the strong bending required to produce weak-beam images might not be present in the case of misfit dislocations. We have thus tried a variety of  $g$ -vectors which could be used to image bulk dislocations with

$b = 1/2\langle 111 \rangle_{\text{Nb}}$ . We failed to detect the dislocations with  $g$ -vectors of type  $1\bar{1}0$ ,  $11\bar{2}$  and  $2\bar{2}\bar{2}$  in orientations close to the  $[111]$  zone axis. Only images which were obtained by tilting to a  $110$  systematic orientation close to the  $[001]$  zone axis revealed the arrangement of the dislocation lines. Figure 5 shows a bright field image obtained under kinematical (equivalent to weak beam) conditions. The specimen area is bent leading to a variation of the excitation error across the image. In the dark bend contour strong moiré fringes can be seen whereas sharp dislocation lines become visible in the areas adjacent to the bend contour. The visibility in this orientation is in agreement with our observation that strong bending of lattice planes can only be seen in the HREM images if the dislocation is viewed in grazing incidence along a  $[001]$  direction. In Fig. 5 only one set of the misfit dislocations forming the complete array can be seen. It consists of a parallel arrangement of continuous dislocation lines. The other two sets are related to the set shown by the threefold symmetry, i.e. two  $120^\circ$  rotations. From this we can conclude that the misfit dislocations are forming a triangular array at the interface between the Nb and the sapphire. We were not able to image the other two sets of parallel dislocations in one sample area because of the limited tilt angle capacity of the microscope.

### (c) Image simulation and interpretation

Quantitative HREM requires computer simulation. The atomistic configuration is obtained if experimental images are identical to images simulated for specific atomistic models. The analysis requires the knowledge of the exact focusing value and the foil thickness. These values have to be determined in a first step [12]. The determination of the foil thickness is most accurate if observed images of the Nb and Al<sub>2</sub>O<sub>3</sub> are compared to tableaux of calculated lattice images for varying thicknesses and focus values [9]. Good agreement between the simulated images and the experimental image is obtained for a defocus of  $\Delta f = -40$  nm and a foil thickness of  $t = 7$  nm in Nb and Al<sub>2</sub>O<sub>3</sub>. From the simulated images it is also possible to determine the positions of the atoms in both crystals with respect to the intensity distribution in the experimental image. The next step is to identify the translational state  $T$  of the two crystals with respect to each other. Such a translational state only exists in the areas of good matching. In these areas the two crystals become commensurate at the interface by expanding the lattice plane spacing of the Nb (Fig. 6). The translational vector  $T$  ( $T_1, T_2, T_3$ ) can be constructed so that the components  $T_1$  and  $T_2$  lie within the interface plane and  $T_3$  is perpendicular to it.

An inspection of the HREM images (Figs 1 and 2) reveals that certain lattice fringes in Nb and Al<sub>2</sub>O<sub>3</sub> transfer continuously into each other across the interface. Furthermore, the positions of the atoms



Fig. 4. Bright field images of a plan-view specimen of the interface. The images were taken along systematic orientations close to the  $[111]$  zone axis of Nb. Moiré fringes parallel to the  $\{110\}$  planes indicate that the mismatch is distributed evenly in all three directions. In this projection dislocation lines should be inclined with respect to moiré fringes. However, under the given imaging conditions their contrast is almost extinct and thus can not be seen due to the strong contrast of the moiré.



Fig. 5. Bright field image in a systematic orientation close to the [001] zone axis (tilt angle 55° from [111] foil normal) with  $g = 110$ . In the dark bend contours (Bragg condition) only moiré fringes can be seen whereas sharp dislocation lines (arrowed) become visible in the areas adjacent to the bent contour (kinematical diffraction condition).

with respect to these lattice fringes in the experimental images are known. However, due to the noise present in the experimental image the position of the atomic columns can not be located very accurately [Fig. 7(a)]. In order to reduce the noise of our experimental images we have applied a Fourier filtering technique, which has recently been developed for interfaces. Details of the technique will be published

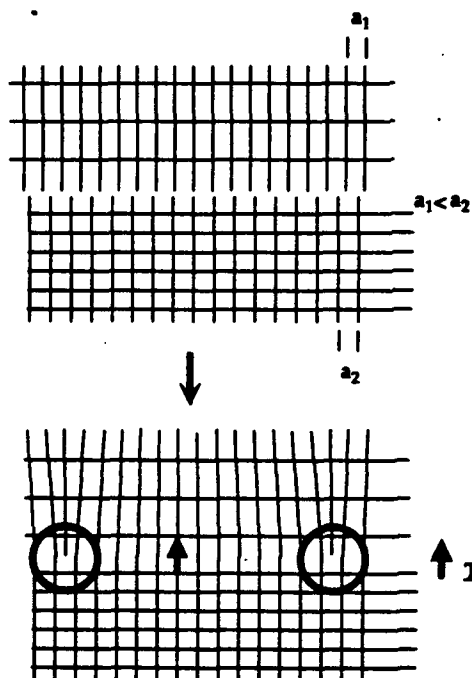


Fig. 6. The lattice plane spacings of two different materials are incommensurate. If two lattice planes of both materials are brought together in one point the same match will never occur again along the interface. Due to relaxations along the interface an epitaxial fit can be achieved at metal-ceramic interfaces. The mismatch is accommodated by localized misfit dislocations in the metal (in circles). In the regions of good matching between these defects a unique translational state is obtained between both lattices which can be described by a translational vector  $T$ .

elsewhere [13]. The result is shown in [Fig. 7(b)]. From the known positions of the atoms in both the Nb and the Al<sub>2</sub>O<sub>3</sub> we have determined the translational state of both lattices across the interface. From this a model of the atomic structure at the interface can be derived. If we assume that the lattice continues undisturbed up to the interface, then the atomistic structure represented in Fig. 8 is obtained: the Al<sub>2</sub>O<sub>3</sub> is terminated by an oxygen layer and the Nb atoms of the first Nb layer fit accurately in the A sites [Fig. 8(b)] of the oxygen layer under which no Al ions are positioned. An obvious choice for the origin of the translational vector  $T$  is given by one of the Al-sublattices as indicated in Fig. 8(a) and (b). The first Nb layer possesses exactly the same three-fold symmetry and the same atomic distances as the individual layers of the Al-sublattice parallel to the interface.

The third and final step is to simulate HREM images for the structure model shown in Fig. 8 and to vary the individual parameters until a best fit is obtained. Four examples of the simulated images for different parameters are shown in Fig. 7(c-f). Figure 7(c) shows the image with the best fit from which we determined the translational vector  $T$ . Figure 7(d) and (e) show the result for a decrease or an increase of the distance between the two lattices, i.e. the component  $T_3$ , by 0.04 nm. The relative shift of the lattice planes can be seen by viewing the images under grazing incidence. Figure 7(f) shows an image which was obtained by removing the last oxygen layer of the sapphire lattice. This results in a contrast along the interface which is clearly different from the one in the experimental image and also leaves a gap at the interface where the atoms would not be in touch with each other.

From Fig. 7(c) the components  $T_1$ ,  $T_2$  and  $T_3$  of the translational vector result in

$$T_1 = a_0 \sqrt{3}/6 = 0.137 \text{ nm}, \quad T_2 = a_0/2 = 0.238 \text{ nm},$$

$$T_3 = c_0/6 = 0.216 \text{ nm}$$

where  $a_0$  and  $c_0$  are the lattice constants of sapphire. The experimental error in determining each individual component is  $\pm 0.02$  nm. The vector  $(T_1, T_2, T_3)$  given above is a lattice vector of the Al sublattice indicated in Fig. 8(a). Therefore, within the experimental error, the Nb atoms of the first layer are positioned exactly in the sites where the Al-ions of the next layer would be placed if the sapphire lattice would be continued.

## DISCUSSION

Qualitatively, the Nb film formation on (0001)<sub>s</sub> substrates was described in Ref. [4]. Steps exist at the sapphire surface which may act as nucleation centers for the Nb film. The growth conditions are selected such that two-dimensional crystal growth (ledge growth) occurs. The initially reconstructed, Al rich

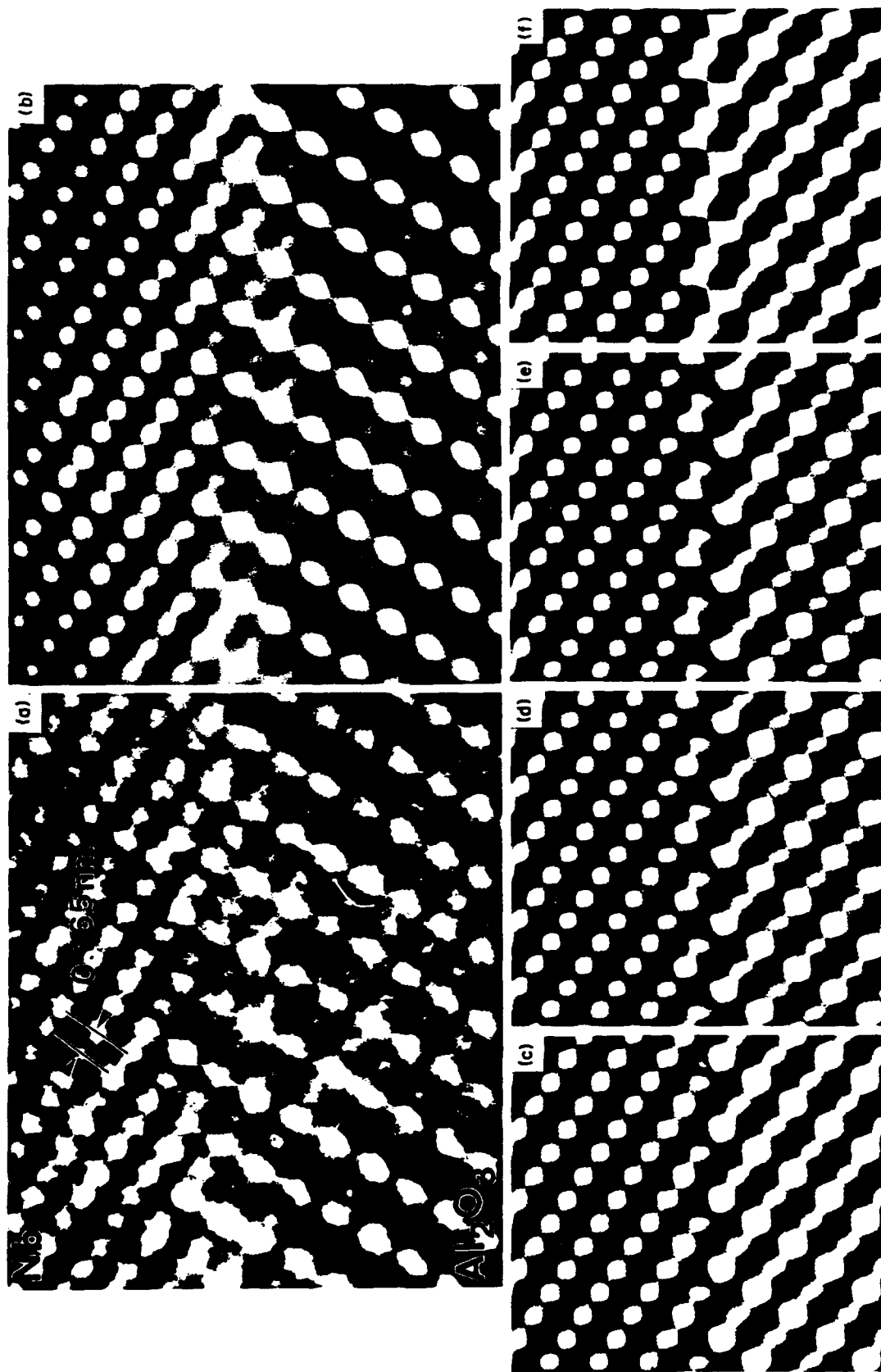


Fig. 7. Comparison between (a) the experimental image taken along direction A, (b) the same image after Fourier-filtering and (c-f) simulated images for various conditions: (c) simulated image showing the best fit to the experimental image, (d) 0.04 nm shorter distance between the two lattices, (e) 0.04 nm longer distance and (f) after removing the terminating oxygen layer of the sapphire.

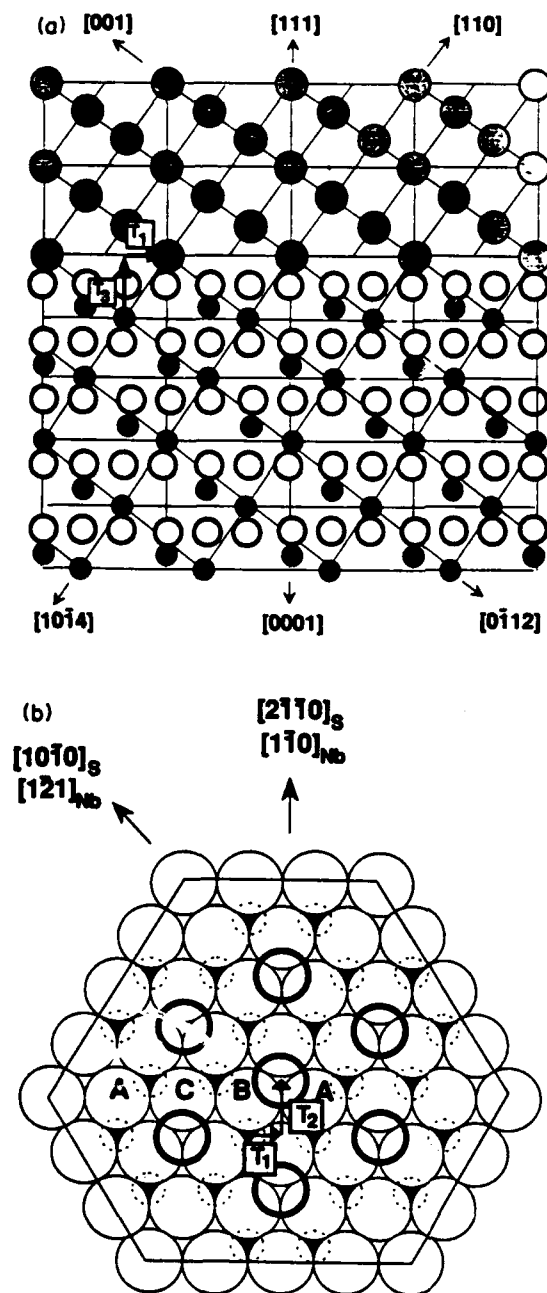


Fig. 8. Schematic drawings of the atomic positions at the Nb-Al<sub>2</sub>O<sub>3</sub> interface. (a) View parallel to the interface. O<sup>2-</sup> ions: light large circles; Al<sup>3+</sup>: black circles; Nb atoms: grey circles. Note the continuous transition of (110)<sub>Nb</sub> to (10 $\bar{1}$ 4)<sub>S</sub> planes and (001)<sub>Nb</sub> to (0 $\bar{1}$ 12)<sub>S</sub> planes. (b) View perpendicular to the interface. O<sup>2-</sup> ions: light large circles; Al<sup>3+</sup>: dark sections of small circles; Nb atoms: bold medium sized circles. It is assumed that the O<sup>2-</sup> ions form the outermost layer. The Nb atoms of the first Nb layer are positioned above the empty sites of the first Al<sup>3+</sup> layer.

surface of the sapphire [14] still possesses 3-fold symmetry with characteristic distances equivalent to atomistic distances of (111)<sub>Nb</sub> planes. For symmetry reasons it is expected that the first deposited monolayer of Nb atoms has an OR which is dictated by the symmetry of the sapphire surface leading to

(111)<sub>Nb</sub>/(0001)<sub>S</sub>. Our experiments show no evidence that the surface reconstruction is still present at our Nb-Al<sub>2</sub>O<sub>3</sub> interface. From this we conclude that a transformation to the bulk structure occurs during growth of the Nb film, thus lowering the energy of the interface.

No twins could be identified in the (nearly) perfect Nb film. It was demonstrated that a unique atomistic relationship exists between the sapphire surface and the monoatomic Nb layer. There exists only one set of Nb atom positions on the unreconstructed sapphire surface which leads to a twin free film [Fig. 8(b)]. Nb atoms must be located on the terminating O<sup>2-</sup> layer of sapphire on top of "empty sites". Comparison of experimental HREM images with the corresponding simulated images verified this hypothesis. For the first time all three components of the translational vector between the two lattices joining at a metal-ceramic interface could be determined.

The location of the Nb atoms on top of the terminating O<sup>2-</sup> layer is such that the Al sublattice which would form the next layer of the sapphire is continued. This implies that the distance between a Nb atom of the first layer and the three neighbouring O<sup>2-</sup> ions is shorter than the distance which would be expected for neutral Nb atoms. However, a good match is obtained for the radius of the Nb<sup>3+</sup> ion. A layer of Nb<sup>3+</sup> would also account for the charge balance across the interface assuming that a complete O<sup>2-</sup> layer is terminating the sapphire at the interface.

In conclusion the epitaxial growth of Nb on basal plane sapphire seems to be dictated by a continuation of the cation sublattice of the sapphire in both location and ionicity of the Nb atoms of the first layer. Nb grows well on sapphire because the resulting first layer has the same symmetry and atomic arrangement as the (111) plane of bulk Nb, with only a 1.9% mismatch. The model we present here was derived mainly from a geometrical evaluation of the HREM images. It therefore does not take into account the effects of possible interdiffusion leading to a partial substitution of e.g. Nb by Al near the interface. HREM as a method is fairly insensitive to such a change in chemistry which leaves the structure unaffected. The chemistry of the interface therefore will have to be studied by high resolution chemical analysis.

*Acknowledgements*—This work was supported in part by the Department of Energy under contract DE-AC02-76ER01198 (CPF) and by the Bundesministerium für Forschung und Technologie (BMFT), contract NTS 0230 0 (MR). The authors gratefully acknowledge the use of the Atomic Resolution Microscope at the National Center for Electron Microscopy in Berkeley, Calif., U.S.A.

## REFERENCES

1. M. Rühle, A. G. Evans, M. F. Ashby and J. P. Hirth (editors), *Metal-Ceramic Interfaces*. Pergamon Press, New York (1990).

2. H. Fischmeister, W. Mader, B. Gibbesch and G. Elssner, *Mater. Res. Symp. Proc.* **22**, 529 (1988).
3. W. Mader, *Z. Metallk.* **80**, 139 (1989).
4. C. P. Flynn, in [1] p. 168.
5. D. Knauß and W. Mader, *Ultramicroscopy*. **37**, 247 (1991).
6. J. Mayer, W. Mader, F. O. Philipp, C. P. Flynn and M. Rühle, *Inst. Phys. Conf. Ser.* **98** (EMAG 89), 349 (1989).
7. J. Mayer, C. P. Flynn and M. Rühle, *Ultramicroscopy* **33**, 51 (1990).
8. A. Strecker, U. Salzberger and J. Mayer, to be published.
9. P. H. Stadelmann, *Ultramicroscopy* **21**, 131 (1987).
10. R. C. Pond, *J. Microsc.* **135**, 213 (1984).
11. D. J. H. Cockayne, *Z. Naturf.* **27a**, 452 (1972).
12. J. C. H. Spence, *Experimental High Resolution Electron Microscopy*, 2nd edn. Clarendon Press, Oxford (1987).
13. G. Möbus, G. Necker and M. Rühle, *Ultramicroscopy*, to be published.
14. T. M. French and G. A. Somorjai, *J. Phys. Chem.* **74**, 2409 (1970).

## HIGH RESOLUTION ELECTRON MICROSCOPY STUDIES OF INTERFACES BETWEEN $\text{Al}_2\text{O}_3$ SUBSTRATES AND MBE GROWN NB FILMS

J. MAYER,\* J. DURA,\*\* C.P. FLYNN\*\* AND M. RÜHLE\*

\*Max-Planck-Institut für Metallforschung, Institut für Werkstoffwissenschaft,  
7000 Stuttgart, FRG

\*\*University of Illinois at Urbana-Champaign, Materials Research Laboratory,  
Urbana, IL 61801, USA

### ABSTRACT

Single crystal niobium films were grown by Molecular Beam Epitaxy (MBE) on  $(0001)_S$  sapphire substrates. Cross-sectional specimens with thickness of  $< 20$  nm were prepared so that the Nb/ $\text{Al}_2\text{O}_3$  interface could be investigated by high resolution electron microscopy (HREM). The orientation relationship between the metal film and the ceramic substrate was verified by selected area diffraction:  $(111)_{\text{Nb}} \parallel (0001)_S$  and  $[\bar{1}\bar{1}0]_{\text{Nb}} \parallel [2\bar{1}\bar{1}0]_S$ . The atomistic structure of the interface was identified by HREM.

### INTRODUCTION

Metal/ceramic interfaces exert an important, and sometimes controlling, influence on the performance of engineering materials in many different applications in materials science [1]. A knowledge of the atomistic structure of such interfaces is a prerequisite for an understanding of their properties. Three methods are capable of generating well defined metal/ceramic interfaces: bonding at moderate temperatures and pressures [2], internal oxidation of metallic alloys [3], and evaporation of metals onto clean ceramic surfaces [4]. While with all three methods well defined interfaces could be obtained, the latter method allows control over both substrate material/orientation and overlayer composition.

Nb/ $\text{Al}_2\text{O}_3$  serves as an excellent "model" system since Nb and  $\text{Al}_2\text{O}_3$  possess nearly the same thermal expansion coefficients and most thermodynamic quantities are well established for both components. Several HREM studies have been reported concerning the atomistic structure of Nb/ $\text{Al}_2\text{O}_3$  interfaces formed after diffusion bonding [5]. The orientation relationship (OR) between Nb and  $\text{Al}_2\text{O}_3$  is determined by the manufacturing route [6]. While the OR is preset for interfaces prepared by diffusion-bonding, topotaxial or epitaxial OR develops during internal oxidation and epitaxial growth, respectively. During internal oxidation a topotaxial relationship forms between Nb and  $\text{Al}_2\text{O}_3$  [3] so that close-packed planes of both systems are parallel to each other, i.e.:

$$(110)_{\text{Nb}} \parallel (0001)_S \text{ and } [011]_{\text{Nb}} \parallel [01\bar{1}0]_S \quad (S=\text{sapphire}) \quad (1)$$

Epitaxial growth of very high quality single-crystalline overlayers of Nb on sapphire has been a subject of recent experiments [4,6]. An OR was determined with a  $(111)_{\text{Nb}}$  plane parallel to the basal plane of the sapphire [4]:

$$(111)_{\text{Nb}} \parallel (0001)_S \text{ and } [\bar{1}\bar{1}0]_{\text{Nb}} \parallel [2\bar{1}\bar{1}0]_S \quad (2)$$

The aim of the present study was to characterize by HREM the atomistic structures of Nb/Al<sub>2</sub>O<sub>3</sub> interfaces formed by MBE growth of Nb layers on a (0001)<sub>S</sub> sapphire substrate. Quantitative HREM resulted in a determination of the translational state of the two crystals close to the interface and of the chemistry of the terminating plane of Al<sub>2</sub>O<sub>3</sub>.

#### EXPERIMENTAL DETAILS

The Nb layers were fabricated in an MBE growth chamber as described elsewhere [4]. Typical growth rates were one monolayer/s. The films were grown to thicknesses ranging from 100 nm to 500 nm. For the TEM specimen preparation a special technique was used which is described in [4].

The HREM studies were performed at the Atomic Resolution Microscope (ARM) at the National Center for Electron Microscopy (NCEM), Berkeley, CA, USA. The microscope was operated at 800 kV. The point-to-point resolution of the instrument is in the range of 0.17 nm. Image simulations were performed using Stadelmann's program [7]. The comparison between experimentally obtained and simulated images was performed by optical inspections.

#### EXPERIMENTAL RESULTS

Quantitative HREM of interfaces requires that the electron beam is incident along high symmetry directions in both crystals. Furthermore, the electron beam has to be parallel to the plane of the interface. For OR(2) these conditions are fulfilled if the electron beam is incident along  $[1\bar{1}0]_{\text{Nb}} \parallel [2\bar{1}\bar{1}0]_{\text{S}}$  (direction A) or along  $[1\bar{2}1]_{\text{Nb}} \parallel [10\bar{1}0]_{\text{S}}$  (direction B) [4]. High resolution electron micrographs were taken from the same interface area in both directions A and B by simply tilting the specimen inside the ARM.

Fig. 1 shows an overview of a large area of a near interface region. The defocus of the objective lens is slightly more positive ( $\Delta f = -40$  nm) than the Scherzer defocus ( $\Delta f = -55$  nm). Lattice planes can be readily identified in Nb and Al<sub>2</sub>O<sub>3</sub>. The foil thicknesses of Nb and Al<sub>2</sub>O<sub>3</sub> are identical. In Nb regions of good matching (M) and poor matching (D) alternate at the interface. Steps can also be identified (S). The regions of poor matching (D) cover less than 10% of the interface plane and can be described as slightly delocalized misfit dislocations [4]. This paper deals only with the regions of good matching, which cover more than 90% of the interfacial area.

The region of good matching (Fig. 1, M) is imaged at a higher magnification in Fig. 2. Fig. 2a shows the interface with the electron beam parallel to direction A. Lattice planes transfer continuously from Nb to Al<sub>2</sub>O<sub>3</sub>. Fig. 2b is a micrograph of the same interface viewed along orientation B. Only  $(10\bar{1})_{\text{Nb}}$  lattice planes with a spacing of 0.233 nm are visible in the Nb crystal. The (222) lattice planes (perpendicular to  $(10\bar{1})$ ) possess a spacing of 0.095 nm which is beyond the information limit of the ARM. In both orientations (Figs. 2a and 2b) a perfect match of the Nb and Al<sub>2</sub>O<sub>3</sub> lattice at the interface is visible. The lattice mismatch of the  $(0\bar{1}10)_{\text{S}}$  and  $(1\bar{1}\bar{2})_{\text{Nb}}$  planes which are perpendicular to the interface is only ~1.9% and this misfit is accommodated by localized defects (misfit dislocations) in the regions of poor matching. This allows the Nb lattice in between these defects

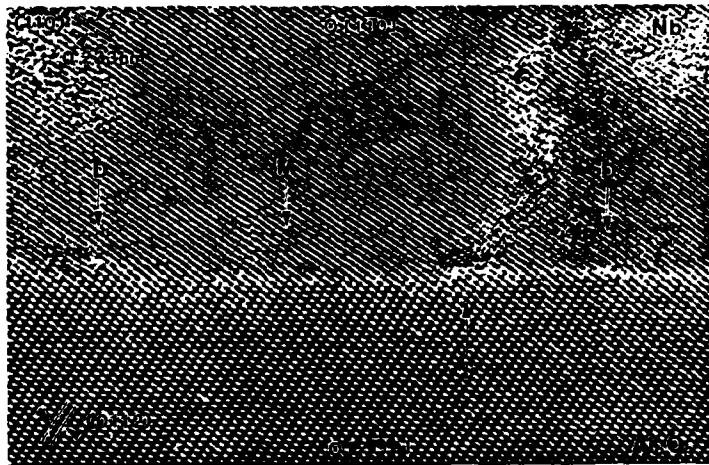


Fig. 1: High resolution image of a Nb/Al<sub>2</sub>O<sub>3</sub> interface. Lattice planes can clearly be identified in both, sapphire and Nb. Foil thickness ~ 10 nm. At the interface regions of good matching (M) and poor matching (D) alternate. S: step in the substrate.

to expand slightly along the interface (the Nb lattice possesses the smaller lattice plane spacing) resulting in extended regions of perfect matching. The expansion of the lattice plane spacing parallel to the interface is limited to regions close to the interface. The lattice planes of the Nb, especially near the misfit dislocations, are bent resulting in a continuous transition to the undistorted Nb lattice further away from the interface (this can be seen by viewing Fig. 1 under grazing incidence). No dislocations or lattice distortions could be seen in the Al<sub>2</sub>O<sub>3</sub> lattice.

#### IMAGE SIMULATION AND INTERPRETATION

Quantitative HREM requires computer simulation. The atomistic configuration is obtained if experimental images are identical to images simulated for specific atomistic model configurations. The analysis requires the knowledge of the exact focusing value and the foil thickness [8]. The determination of the foil thickness is most accurate if observed images of the Nb and Al<sub>2</sub>O<sub>3</sub> are compared to tableaus of calculated lattice images for varying thicknesses and focus values for both, Nb and Al<sub>2</sub>O<sub>3</sub> [7]. Fig. 3 shows that good agreement between the simulated images and the experimental image is obtained for a defocus of  $\Delta f = -40$  nm and a foil thickness of  $t = 7$  nm in Nb and Al<sub>2</sub>O<sub>3</sub>. From the simulated images it is also possible to determine the positions of the atoms in both crystals with respect to the intensity distribution in the experimental image (Fig.3).

The next step is to identify the translational state  $\mathbf{T}$  of the two crystals with respect to each other. Such a translational state only exists in the areas of good matching because the two crystals become commensurate at the interface by expanding the lattice plane spacing of the Nb. The vector  $\mathbf{T}$  ( $T_1, T_2, T_3$ ) can be constructed so that the components  $T_1$  and  $T_2$  lie within the interface plane and  $T_3$  is perpendicular to it.

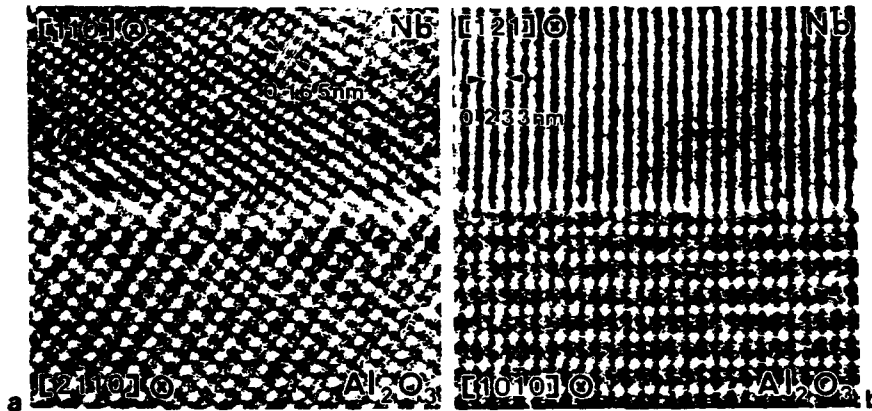


Fig. 2: High resolution image of Nb/Al<sub>2</sub>O<sub>3</sub> interface. Region of good matching (M).

a.) Direction A with  $[1\bar{1}0]_{\text{Nb}} \parallel [2\bar{1}1]_s$

b.) Direction B with  $[\bar{1}21]_{\text{Nb}} \parallel [10\bar{1}]_s$

Note that contrast fringes cross the interfaces without steps of interphases.

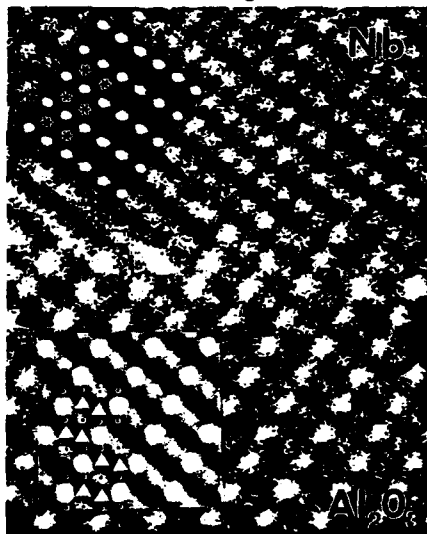


Fig. 3: High resolution image of Fig. 2a at higher magnification. The inserts represent simulated images for a specimen thickness  $t = 7$  nm and a defocus value of  $\Delta f = -40$  nm. The atom positions are marked. Nb: stars, Al: white triangles, O: black on white dots.

An inspection of the HREM images (Figs. 1, 2) reveals that certain lattice fringes in Nb and Al<sub>2</sub>O<sub>3</sub> transfer continuously into each other across the interface. Furthermore, the positions of the atoms with respect to these lattice fringes in the experimental images are known (Fig. 3). If we assume that the lattice continues undisturbed up to the interface, then the atomistic structure represented in Fig. 4 and 5 is obtained: the Al<sub>2</sub>O<sub>3</sub> is terminated by an oxygen layer and the Nb atoms of the first Nb layer fit accurately in the A sites (Fig. 5) of the oxygen layer under which no Al ions are positioned. An obvious choice for the origin of the translation vector  $\mathbf{I}$  is given by one of the Al-sublattices as indicated in Figs. 4 and 5. The first Nb layer has exactly the same threefold symmetry and the same atomic

Fig. 4: Schematic drawing of the atomic positions at the Nb/Al<sub>2</sub>O<sub>3</sub> interface. The result is obtained by quantitative HREM. O<sup>2-</sup> ions: light large circles, Al<sup>3+</sup>: black circles, Nb atoms: grey circles. Note the approximate parallelism of [110]<sub>Nb</sub> to [10 $\bar{1}$ 4]<sub>S</sub> planes and [001]<sub>Nb</sub> to [0 $\bar{1}$ 12]<sub>S</sub> plane.

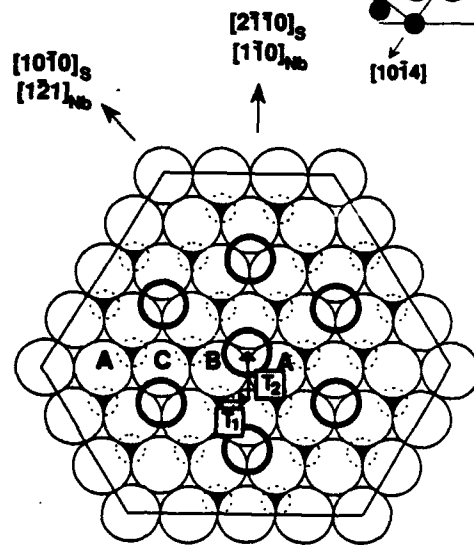


Fig. 5: Schematic drawing of a non-reconstructed (0001)<sub>S</sub> basal surface. O<sup>2-</sup> ions: light large circles, Al<sup>3+</sup>: dark sections of small circles, Nb atoms: bold medium sized circles. It is assumed that the O<sup>2-</sup> ions form the outermost layer. The Nb atoms of the first Nb layer are positioned above the empty sites of the first Al<sup>3+</sup> layer.

distances as the individual layers, parallel to the interface. From this T<sub>1</sub>, T<sub>2</sub> and T<sub>3</sub> result in:

$$T_1 = a_0 \sqrt{3}/6 = 0.137 \text{ nm}, T_2 = a_0/2 = 0.238 \text{ nm}, T_3 = c_0/6 = 0.216 \text{ nm}$$

where  $a_0$  and  $c_0$  are the lattice constants of sapphire. The values of T<sub>1</sub>, T<sub>2</sub>, T<sub>3</sub> were calculated according to the model shown in Fig. 4, not taking into account an experimental error of  $\pm 0.02$  nm in determining the location of the lattice planes from the high resolution images.

## DISCUSSION

Qualitatively, the Nb film formation on (0001)<sub>S</sub> substrates was described in [4]. Steps exist at the sapphire surface which may act as nucleation centers for the Nb film. The growth conditions are selected such that two-dimensional crystal growth (ledge growth) occurs. The initially reconstructed, Al rich surface of the sapphire [9] still possesses 3-fold symmetry with characteristic distances equivalent to atomistic distances of (111)<sub>Nb</sub> planes. For symmetry reasons it is expected that the first deposited monolayer of Nb atoms has an OR which is dictated by the symmetry of the sapphire surface leading to (111)<sub>Nb</sub> || (0001)<sub>S</sub>. Our experiments show no evidence that the surface reconstruction is still present at our Nb/Al<sub>2</sub>O<sub>3</sub> interface. From this we conclude that a transformation back to the bulk structure occurs during growth of the Nb film, by this presumably lowering the energy of the interface.

No twins could be identified in the (nearly) perfect Nb film. It was demonstrated that a unique atomistic relationship exists between the sapphire surface and the monoatomic Nb layer. There exists only one set of Nb atom positions on the unreconstructed sapphire surface which leads to a twin free film (Fig. 5). Nb atoms must be located on the terminating O<sup>2-</sup> layer of sapphire on top of "empty sites." The quantitative evaluation of the HREM images verified this hypothesis. In a concluding step, experimental HREM images of regions which included the interface have to be compared to corresponding simulated images [10].

## ACKNOWLEDGEMENTS

This work was supported in part by the Department of Energy under contract DE-AC02-76ER01198 (CPF) and by the Bundesministerium für Forschung und Technologie (BMFT), contract NTS 0230 0 (MR). The authors gratefully acknowledge the use of the Atomic Resolution Microscope at the National Center for Electron Microscopy in Berkeley, CA, USA.

## REFERENCES

- [1] M. Rühle, A.G. Evans, M.F. Ashby, and J.P. Hirth (eds.), Structure, Chemistry and Fracture Resistance of Metal/Ceramic Interfaces, (Pergamon Press, 1990).
- [2] H. Fischmeister, W. Mader, B. Gibbesch, and G. Elssner, Mater. Res. Symp. Proc. **22**, 529 (1988).
- [3] W. Mader, Z. Metallkunde **80**, 139 (1989).
- [4] J. Mayer, C.P. Flynn, and M. Rühle, Ultramicroscopy **33**, 51 (1990).
- [5] D. Knauß and W. Mader, Ultramicroscopy, submitted.
- [6] J. Mayer, W. Mader, F.O. Phillipp, C.P. Flynn, and M. Rühle, Inst. Phys. Conf. Ser. **98** (EMAG 89), 349 (1989).
- [7] P.H. Stadelmann, Ultramicroscopy **21**, 131 (1987).
- [8] J.C.H. Spence, Experimental High Resolution Electron Microscopy, 2nd ed. (Clarendon Press, Oxford, 1987).
- [9] T.M. French and G.A. Somorjai, J. Phys. Chem. **74**, 2409 (1970).
- [10] J. Mayer, to be published.

## High-resolution transmission electron microscopy studies of structural modifications in Pd-Al<sub>2</sub>O<sub>3</sub> interfaces

By T. MUSCHIK† and M. RÜHLE†

Materials Department, University of California,  
Santa Barbara, California 93106, USA

[Received 27 February 1991 and accepted 20 April 1991]

### ABSTRACT

High-resolution transmission electron microscopy (HRTEM), in conjunction with extensive image simulation, has been applied to topotaxial Al<sub>2</sub>O<sub>3</sub>-Pd interfaces formed by the internal oxidation of Pd-Al alloys. The Al<sub>2</sub>O<sub>3</sub> phase has been characterized as  $\eta$ -Al<sub>2</sub>O<sub>3</sub> from HRTEM images. We conclude that the Al<sub>2</sub>O<sub>3</sub> is terminated by O ions after oxidation and by Al ions after a subsequent annealing in Al vapour. This structural modification is consistent with earlier H-trapping experiments. The origin of the ceramic precipitates in relation to the transmission electron microscopy and complementary X-ray measurements and the difficulties of applying HRTEM to an incoherent topotaxial interface are discussed.

### §1. INTRODUCTION

The mechanical behaviour of metal-ceramic composites is strongly dependent on the properties of the heterophase boundaries in the material. Therefore an understanding of the relationship between interfacial structure and interface properties is essential. In addition, it is most desirable to understand how structure and properties may be modified, for example by segregation or interphase formation.

Metal-ceramic interfaces can be produced by diffusion bonding (Fischmeister, Mader, Gibbesch and Ellsner 1988), epitaxial growth of a metal (ceramic) film on a ceramic (metal) substrate or by internal oxidation of metal alloys (Meijering 1971). It is expected that during internal oxidation, special low-energy interface configurations develop. Recently, high-resolution transmission electron microscopy (HRTEM) studies were performed at metal-metal oxide interfaces produced by internal oxidation. Quantitative HRTEM studies revealed that in the Ag-CdO system (Necker and Mader 1988), as well as in Cu-Al<sub>2</sub>O<sub>3</sub> (Ernst, Pirouz and Heuer 1991), O forms the outermost layer of the precipitates formed at 'high' O<sub>2</sub> partial pressure, that is during annealing in air at ambient pressure. In contrast, Huang, Mader, Eastman and Kirchheim (1988) gave experimental evidence that the composition of the outermost layer of the ceramic at Pd-Al<sub>2</sub>O<sub>3</sub> interfaces depends on the ratio of the chemical activities of O and Al, respectively, in Pd. From H-trapping experiments (Huang *et al.* 1988) it was concluded that after oxidation (high ratio of O to Al activity) the ceramic precipitates are bounded by O anions, whereas Al cations form the outermost layer of the particles when the Al activity in the metal was increased by annealing the oxidized material in Al vapour (the case of low ratio of O to Al activity). The conclusions of Huang *et al.* (1988) are experimentally well supported, consistent with thermodynamic

† Present address: Max-Planck-Institut für Metallforschung, W-7000 Stuttgart 1, Germany.

‡ Received in final form 16 April 1991.

considerations, and give averaged chemical information about the interfaces. However, H-trapping experiments cannot provide structural information about the Pd-Al<sub>2</sub>O<sub>3</sub> interface on an atomic scale, which would include not only the chemical nature of an ion or atom, but also the atomistic structure at the interface. So far, only conventional transmission electron microscopy (TEM) studies have been performed at Pd-Al<sub>2</sub>O<sub>3</sub> interfaces formed by internal oxidation (Eastman and Rühle 1989). No quantitative HRTEM structural studies have been conducted.

The aim of the present work is to determine, by quantitative HRTEM, the atomistic structure of Pd-Al<sub>2</sub>O<sub>3</sub> interfaces formed at different O to Al activity ratios in Pd, that is in both internally oxidized alloys and alloys that have subsequently been annealed in Al vapour. X-ray diffraction and conventional TEM studies provide information about the nucleation of the precipitates, their morphology and phase distribution. Structural information is obtained by quantitative HRTEM where experimental HRTEM images are compared with simulated HRTEM images calculated for different interface models using the multislice method (for example, Buseck, Cowley and Eyring (1988)). The system Pd-Al<sub>2</sub>O<sub>3</sub> is expected to be suitable for this investigation since good lattice matching of close-packed planes in Pd and close-packed planes in the O sublattice of Al<sub>2</sub>O<sub>3</sub> favours the formation of geometrically simple interfaces during internal oxidation (Eastman and Rühle 1989). Furthermore, no reaction layers are expected to form between Pd and Al<sub>2</sub>O<sub>3</sub> (DeBruin, Moodie and Warble 1972). Simple epitaxial relationships and interface structures facilitate the HRTEM work and the modelling of the interface and thus the calculation of simulated images, which are necessary for a correct interpretation of most HRTEM images.

## §2. EXPERIMENTAL PROCEDURES

Pd-Al alloys with 0.3, 3.0 and 6.0 at.% Al were produced by arc melting 99.999% Pd powder and 99.999% Al granules in argon (Eastman and Rühle 1989). The alloy buttons were homogenized for 20 days at 1273 K in Ar and subsequently cold rolled to about 60 µm thickness. Recrystallization (24 h at 1273 K in Ar atmosphere) produced foils with an average grain size of 100 µm and a distinct [110] texture. Al<sub>2</sub>O<sub>3</sub> precipitates within the foils were produced by internal oxidation in air at ambient pressure for 24 h at 1273 K. The as-oxidized foils are referred to as 'type I specimens' in the following discussion. Some type I foils (40 µm thick) were subsequently annealed for 1 h at 1273 K in Al vapour. These are referred to as 'type II specimens'. Details of the annealing treatment are described by Huang *et al.* (1988) who provided the 'type II' foils. The lattice parameter of Pd was determined by X-ray diffraction prior to and after the internal oxidation.

TEM specimens were prepared by punching discs of 3 mm diameter out of the foils. The discs were then ion milled (5.5 kV Ar<sup>+</sup> at a 17° angle until perforation and finished with 3.5–1.5 kV Ar<sup>+</sup> at the same angle). Conventional TEM investigations were performed on microscopes operated at 200 kV (JEOL 2000 FX) and at 400 kV (JEOL 4000 FX). The atomic resolution microscope (ARM) at the National Center for Electron Microscopy in Berkeley, U.S.A., was used for the HRTEM investigation. The ARM, operated at 800 kV, possesses a spherical aberration coefficient  $C_s$  of 1.93 mm and a focus spread of about 14 nm. Knowledge of these microscope parameters and of experimental parameters such as the specimen thickness  $t$  and the defocus  $\Delta f$  are necessary prerequisites for each quantitative HRTEM study. In quantitative HRTEM (for example, Bourret 1989) the entire experimental imaging process is simulated in a

computer. A model electron beam (characterized by its wavelength, energy spread and beam convergence angle) penetrates a model structure. The scattered electrons exiting the model structure are collected by the 'simulation microscope' (characterized by the spherical aberration coefficient  $C_s$ , the defocus  $\Delta f$  and the radius of the objective aperture) to form the simulated image. The appearance of the simulated image depends on the model structure and the parameters mentioned above. With the parameters of the image formation process known, the model structure can be modified until the simulated image matches the experimental image. The model structure which results in the best matching is then assumed to closely represent the atomistic structure in the real specimen.

The image simulations and the image processing were performed on a Vax Station 3200 using the software packages EMS (Stadelmann 1987) and IDL (VAX IDL, Research Systems, Inc., Denver, Colorado). Some experimental images were digitized using an Eikonix camera linked to the Vax Station 3200.

### §3. RESULTS AND DISCUSSION

In this section, results are reported and discussed for four aspects of the research separately. In §3.1 the identification and selection of Al<sub>2</sub>O<sub>3</sub> phases in the internally oxidized Pd-Al alloy after internal oxidation are described. The phases were identified by inspection of selected-area diffraction (SAD) patterns. We discuss briefly how the precipitate phases and morphologies shed light on the factors controlling the precipitation process and what information X-ray measurements provide.

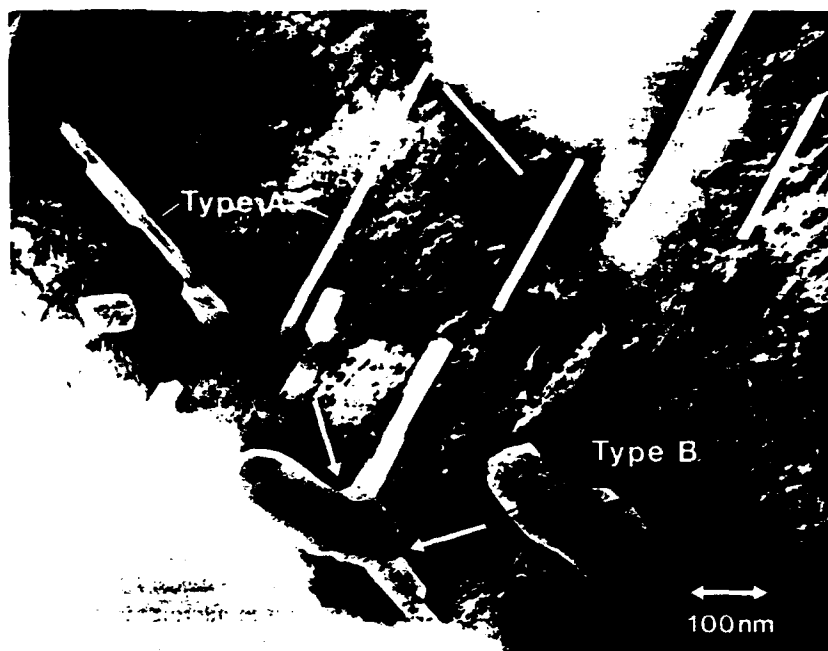
In §3.2 the identification of the phase of Al<sub>2</sub>O<sub>3</sub> precipitates suitable for the HRTEM study of Pd-Al<sub>2</sub>O<sub>3</sub> interfaces is dealt with. Interfaces suitable for HRTEM must fulfil two requirements. Firstly, quantitative HRTEM requires that the interface is planar and that the crystals on either side of the interphase boundary must have a low-index zone axis parallel to the incident electron beam in order to resolve atomic positions in and close to the interface. A sufficient number of suitable precipitates is present in Pd-3 at.% Al oxidized at 1273 K. Secondly, the crystal structure of both adjoining materials must be known. Whereas Pd has a f.c.c. lattice, the structure of suitable Al<sub>2</sub>O<sub>3</sub> particles had to be characterized by a combination of processing of the experimental images and image simulation of hypothetical Al<sub>2</sub>O<sub>3</sub> phases. Together with the phase of the particles a set of consistent values for the specimen thickness  $t$  and the defocus  $\Delta f$  is obtained in an iterative process.

The interface structure determination for an interface in a type II specimen is described in §3.3. Finally, section 3.4 covers a qualitative comparison between interface characteristics of 'type I' and 'type II' specimens. Furthermore, the limitations of HRTEM studies on incoherent interfaces are addressed.

#### 3.1. Phase selection of Al<sub>2</sub>O<sub>3</sub> particles in internally oxidized Pd-Al

During internal oxidation, different Al<sub>2</sub>O<sub>3</sub> phases precipitate in the Pd matrix.  $\alpha$ -Al<sub>2</sub>O<sub>3</sub> particles precipitate only at the grain boundaries (GBs) in Pd-3 at.% Al alloys. The particles possess an approximately ellipsoidal shape and their average size is of the order of 1  $\mu$ m. In contrast, intragranular ellipsoidal  $\alpha$ -Al<sub>2</sub>O<sub>3</sub> particles were observed in Pd-6 at.% Al alloys. The increase in the thermodynamic activity of Al in the alloy from Pd-3 at.% Al to Pd-6 at.% Al is apparently sufficient to overcome energetic and kinetic barriers that prevent  $\alpha$ -Al<sub>2</sub>O<sub>3</sub> from nucleating in the Pd matrix in Pd-3 at.% Al. This

Fig. 1



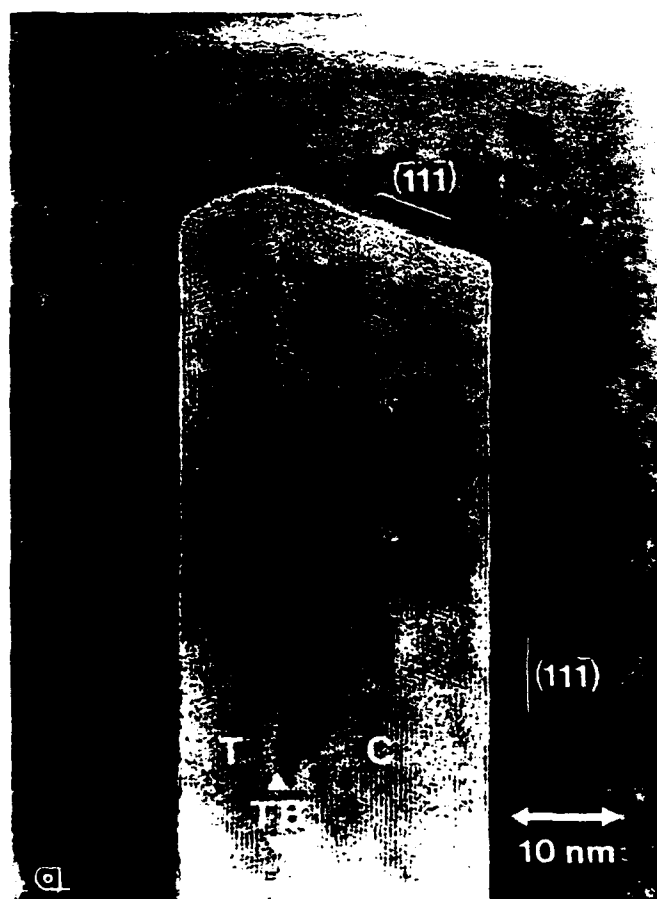
Bright-field image of a typical microstructure inside a grain in a type I specimen (Pd-3 at.% Al, oxidized at 1273 K for 24 h). The observation direction is Pd<110> and the long planar faces of regularly shaped type A precipitates are parallel to Pd{111} planes. The structure of type A particles is generally different from that of irregular shaped type B particles. Note that a type B particle is growing on type A particles (arrows).

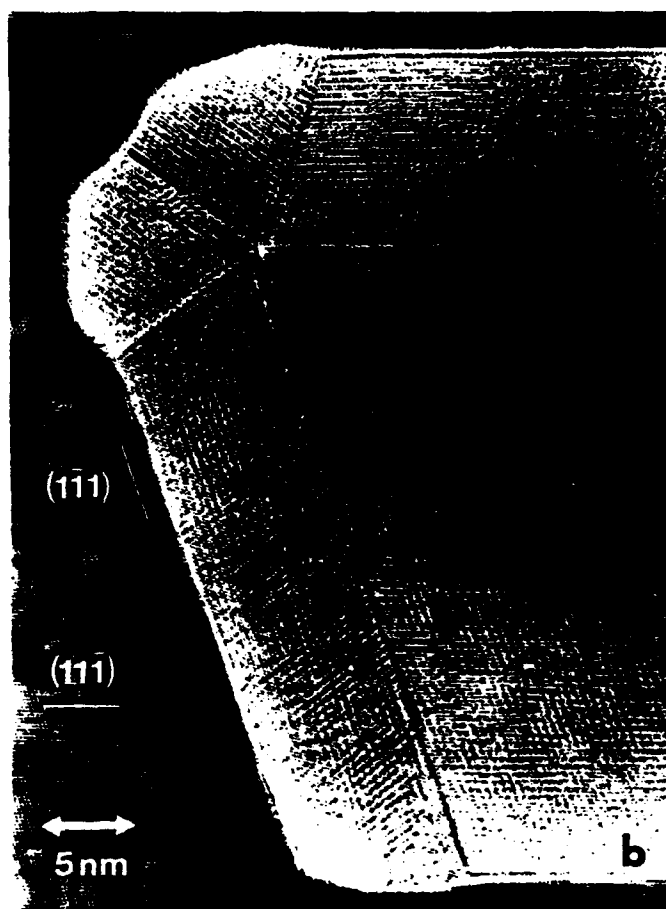
suggests that at 1273 K the nucleation and growth of the thermodynamically stable  $\alpha$ -Al<sub>2</sub>O<sub>3</sub> are favoured by the open structure of the GBs and a high activity of Al in the alloy. In addition, the O activity may be higher in the GBs owing to preferential transport of O into the foils by GB diffusion.

A characteristic distribution of intragranular oxide particles is shown in fig. 1, where two types of precipitates can be distinguished. Irregularly shaped type B precipitates contain stacking faults and appear to be incoherent with the matrix. However, they possess a unique orientation relationship with the matrix. They are frequently found to grow on the regularly shaped type A particles (see arrow in fig. 1). It is not known which type of precipitate forms first. The structure of the type B Al<sub>2</sub>O<sub>3</sub> particles has not yet been reported in the literature. The stability of this phase must be attributed both to the special nucleation-and-growth conditions under the constraint of the Pd matrix and to the specific supply of its constituents, that is to the Al and O activities.

The majority of the regularly shaped type A particles are either twinned or multiply twinned (fig. 2). With few exceptions (see fig. 2(c)) the large planar faces are parallel to Pd{111} planes. The precipitates do not show one single, well developed Al<sub>2</sub>O<sub>3</sub> phase. Selected-area electron diffraction shows that type A particles possess different

Fig. 2





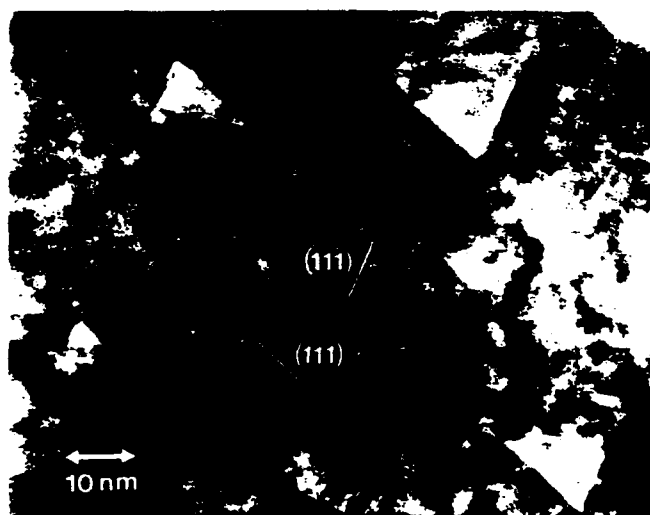


(a) HRTEM image in Pd<110> projection of a typical twinned type A particle with a cubic spinel structure. The twin boundary (TB) separates the part with the cube-on-cube orientation relationship with the matrix (C) from the twin related part (T). (b) HRTEM image in Pd<110> projection showing fivefold twinning at the edge of a type A particle. (c) HRTEM image in Pd<110> projection of a multiply twinned Al<sub>2</sub>O<sub>3</sub> particle with planar faces parallel to Pd{200} planes. This orientation relationship is very rare.

structures which are either  $\eta$ - ( $\gamma$ -),  $\delta$ - or  $\theta$ - $\text{Al}_2\text{O}_3$ . The structures of these types of metastable transition  $\text{Al}_2\text{O}_3$  have in common a more or less distorted f.c.c. stacking of close-packed O anions. The differences between these metastable compounds occurring in the so-called ' $\gamma$  series' of  $\text{Al}_2\text{O}_3$  ( $\gamma$ -,  $\eta$ -,  $\delta$ - and  $\theta$ - $\text{Al}_2\text{O}_3$ ) arise from the Al cation distribution in the octahedral and tetrahedral interstices of the f.c.c. O anion sublattice (for details see for example, Levy, Jayaram, Valencia and Mehrabian (1988) and Wilson and McConnell (1980)). Depending on the degree of order in the cation distribution, different cation distributions lead to different unit-cell descriptions of the various  $\text{Al}_2\text{O}_3$ . It is generally accepted that  $\eta$ - $\text{Al}_2\text{O}_3$  has a cubic spinel structure (Shirasuka, Yanagida, and Yamaguchi 1976), whereas  $\gamma$ - $\text{Al}_2\text{O}_3$  has been reported as either cubic (Lejus 1964) or tetragonal (Saalfeld and Mehrotra 1965) spinel.  $\delta$ - $\text{Al}_2\text{O}_3$  shows a multiple of the spinel unit cell in one direction, leading to a tetragonal (Lippens and DeBoer 1964) or orthorhombic (Jayaram and Levy 1989) unit cell, and  $\theta$ - $\text{Al}_2\text{O}_3$  is monoclinic with a structure isomorphic to  $\beta$ - $\text{Ga}_2\text{O}_3$  (Yamaguchi, Yasui and Chiu 1970). Ernst *et al.* (1991) recently reported a  $\eta'$ -phase which is structurally similar to  $\eta$ - $\text{Al}_2\text{O}_3$ .

All type A precipitates have a cubic close-packed O ion sublattice. This suggests that it may be energetically and/or kinetically favourable for the system to continue the f.c.c. structure of the Pd matrix in the structure of the O sublattice of the intragranular precipitates. X-ray scattering experiments on Pd-3 at.% Al foils oxidized at 1273, 1473 and 1773 K for 24 h indicate that the particles nucleate parallel to  $\{111\}$  planes of the metal. After oxidation at 1273 and 1473 K respectively, the X-ray spectra showed minor peak broadening and dramatically decreased heights of Pd(111) peaks compared with spectra obtained from pure Pd or from Pd-Al foils oxidized at 1773 K. It seems reasonable to assume that a bending of the  $\{111\}$  planes of the metal in the vicinity of

Fig. 3



HRTEM image in Pd $\langle 110 \rangle$  projection of thin  $\text{Al}_2\text{O}_3$  precipitates in  $\{111\}$  planes of Pd after oxidation of a Pd-3 at.% Al alloy at 991 K for 18 h. The planar facets are parallel to Pd $\{111\}$  planes.

the nuclei is responsible for the decrease in the peak intensities. This may indicate that intragranular precipitates preferentially nucleate parallel to {111} planes of Pd and that nuclei might still be present in the alloys after 24 h at 1273 and 1473 K, but not at 1773 K. HRTEM observation of thin precipitates (edge length, about 20 nm) in {111} planes of Pd-3 at.% Al foils oxidized at 991 K for 18 h (fig. 3) also support the idea of the nucleation of type A precipitates parallel to Pd{111} planes. Thus, the nucleation of thin precipitates in {111} planes of Pd and the growth of the particles under the constraint of a f.c.c. metal matrix seem to determine the orientation relationship between matrix and precipitate (parallel close-packed planes) and the precipitate structure.

Practically, only the precipitates with a cubic spinel-type structure are suitable for this HRTEM study, since the cation distribution in  $\delta$ -Al<sub>2</sub>O<sub>3</sub> is unknown and since the frequency of  $\theta$ -Al<sub>2</sub>O<sub>3</sub> particles in the specimens is too small to allow for a systematic study. A typical cubic spinel-type particle is shown in fig. 2(a). The orientation relationship of the twinned cubic spinel particle with the Pd matrix is  $\{111\}_{\text{Pd}} \parallel \{111\}_{\text{Al}_2\text{O}_3}$  and  $\langle 110 \rangle_{\text{Pd}} \parallel \langle 110 \rangle_{\text{Al}_2\text{O}_3}$  for the cube-on-cube part of the particle. The corresponding twin relationship results from a 180° rotation of the Al<sub>2</sub>O<sub>3</sub> lattice around  $\langle 111 \rangle_{\text{Al}_2\text{O}_3}$ . It will be shown in the next section that the cubic spinel-type particles were identified as  $\eta$ -Al<sub>2</sub>O<sub>3</sub>.

### 3.2. Characterization of the cubic spinel-type phase

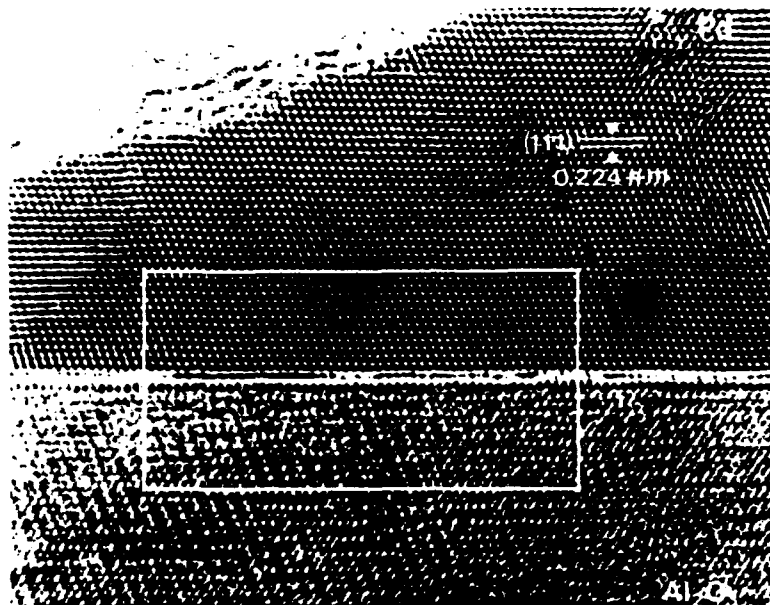
The actual phase of the cubic spinel-type particles in Pd-Al<sub>2</sub>O<sub>3</sub> cannot be determined from simple inspection of SAD patterns, since the SAD patterns of  $\gamma$  and  $\eta$  differ only in the intensities of weak diffraction spots. However, as Pirouz and Ernst (1990) demonstrated recently, HRTEM images are sensitive to slight changes in the distribution of ions in closely related phases. In this section a method will be described which allows the extraction of reliable structural information from HRTEM images either by simple inspection or by comparison of simulated and processed experimental images.

Figure 4 shows the HRTEM micrograph of a Pd-spinel interface in a type II specimen. The lattice parameter of the Al<sub>2</sub>O<sub>3</sub> particle was determined by directly measuring crystallographically corresponding distances (e.g. the average over 50 {111} plane spacings) in Pd and in the adjoining Al<sub>2</sub>O<sub>3</sub>. This simple method is justified as long as no region of contrast reversal is contained in the measuring area even if specimen thickness and defocus are not known. The lattice parameter of the alumina in fig. 4 is 2.7% larger than twice the lattice parameter of the surrounding Pd matrix, which was assumed to be that of pure Pd ( $a=0.3891$  nm). Thus  $a(\text{spinel})=0.799 \pm 0.004$  nm.

The image in fig. 4 is part of a through-focus series of eight HRTEM images with calibrated defocus steps of about 8 nm between subsequent images. The series includes an image taken at minimum contrast (defocus  $\Delta f = -23$  nm). This value was used as a reference for all other images of the defocus series. The appearance of the images of the series together with the respective defocus values obtained by this method are consistent with simulated defocus series of Pd and the Al<sub>2</sub>O<sub>3</sub> phase. The analysis shows that the image in fig. 4 was taken at  $\Delta f = -80$  nm which is close to the first inverse contrast band of the ARM operated at 800 kV.

In fig. 4 there is no contrast reversal in the Pd between the specimen edge and the interface. A comparison of the experimental contrasts with contrasts in a calculated thickness-defocus 'map' of a wedge-shaped Pd crystal then shows that the thickness of

Fig. 4



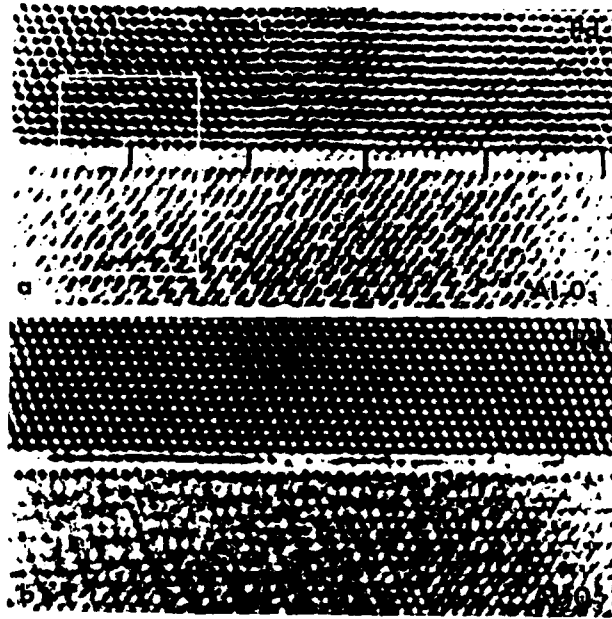
HRTEM image in Pd<110> projection of a Pd- $\eta$ -Al<sub>2</sub>O<sub>3</sub> interface in an Al annealed type II specimen at defocus  $\Delta f = -80$  nm. The marked area was chosen for further study and it is depicted as a digitized image in fig. 5(a).

Pd at the interface is less than about 16 nm if it is assumed that the thickness at the edge of the Pd is less than about 35 nm. For  $\Delta f = -80$  nm the first contrast reversal occurs at about 16 nm thickness and the next at about 35 nm thickness. Furthermore, the simulation shows that the bright dots correspond to atom columns of Pd in the <110> direction. The best match between the experimental and simulated contrast of Pd at different defocus values were simultaneously obtained for  $t = 10 \pm 3$  nm. According to the image simulations, the thickness of the Al<sub>2</sub>O<sub>3</sub> close to the interface is between 7 and 16 nm, and the best match between experimental and simulated contrast is again obtained for  $t = 10 \pm 3$  nm. 10 nm is therefore regarded as the correct specimen thickness at both sides of the interface in the region of interest.

In the next step the structure of the Al<sub>2</sub>O<sub>3</sub> particles was obtained from the experimental images. Obviously, only that part of the experimental image which reflects the periodicity of the crystalline structure is significant. For example, noise introduced by contamination, amorphization of the material during specimen preparation or due to electron damage in the microscope is not significant and should be reduced by processing the experimental image. The filtering of images in reciprocal space (Fourier filtering (for example, Krakow and Smith (1986)) is one suitable processing method; however, it can easily destroy valuable information if not performed carefully. In contrast, a simple method to extract periodic information from noisy experimental images is to calculate 'average images' from suitable regions of digitized images (for example, Smith and Eyring (1982)).

Figure 5 shows digitized images of identical sections of the near interface region in fig. 4 for two different defocus values. The area selected for image averaging is indicated

Fig. 5

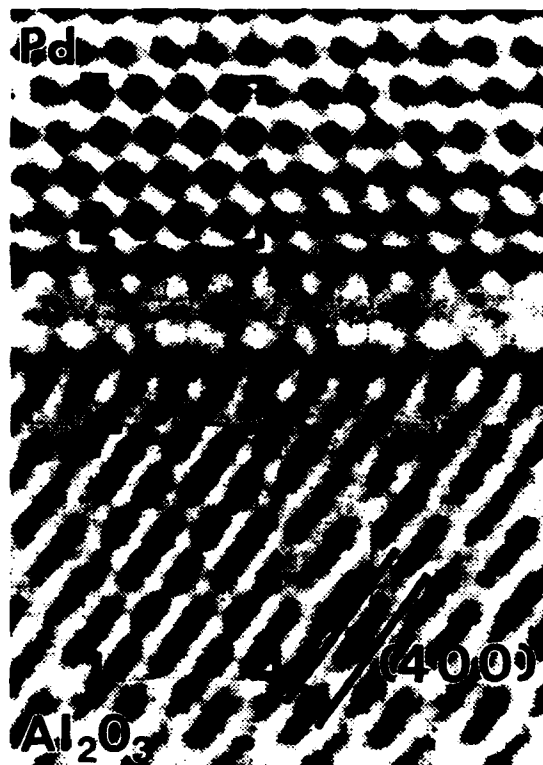


Digitized HRTEM images of identical parts of the interface in a type II specimen shown in fig. 4 for (a)  $\Delta f = -48$  nm and (b)  $\Delta f = -80$  nm. The marked area in (a) was selected for the image averaging (see fig. A 1 (a) in the Appendix). The black bars crossing the interface in (a) connect every tenth Pd atom column with every tenth O ion column in the Al<sub>2</sub>O<sub>3</sub> and demonstrate the continuous change in the interfacial geometry along the interface. There are no localized misfit dislocations with a line direction parallel to Pd<110> (see also fig. 4). The implications of this apparent incoherence are discussed in detail in §3.3.

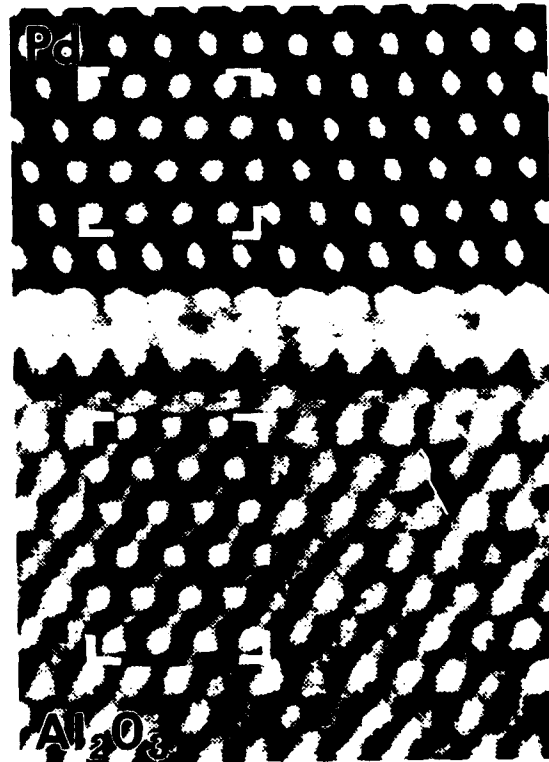
in fig. 5(a). The averaging procedure is explained in detail in the Appendix. The corresponding average image (fig. A 1 (c) and background of fig. 6(a)) can be regarded as an idealized experimental image for  $\Delta f = -48$  nm and is used to compare experimental and simulated images for the determination of the Al<sub>2</sub>O<sub>3</sub> structure (see fig. 6(a)). The image in fig. 6(b) is an average image for  $\Delta f = -80$  nm obtained in a similar manner.

The spinel phase is now characterized using the improved (averaged) experimental HRTEM images. The SAD patterns indicate a cubic spinel-type structure. Different Al<sub>2</sub>O<sub>3</sub> phases of this type, namely  $\gamma$ -,  $\eta$ - and  $\eta'$ -Al<sub>2</sub>O<sub>3</sub>, have been reported, whose main difference is the distribution of cations in the 64 tetrahedral and 32 octahedral interstices in the cubic close-packed O sublattice of spinel. In normal spinel (space group, Fd3m, No. 227 in the *International Tables for Crystallography* (Hahn 1987)) with stoichiometry AB<sub>2</sub>O<sub>4</sub>, only 16 octahedral (d) and 8 tetrahedral (a) sites are occupied by cations. The O anions occupy 32 (e) sites, and the octahedral 16 (c) and the tetrahedral 8 (b) and 48 (f) sites remain vacant. The symbols (a), (b), etc., denote the Wyckoff notation used in the *International Tables for Crystallography*. Since Al<sub>2</sub>O<sub>3</sub> is exactly stoichiometric there are only 21½ cations to be distributed on the interstices provided by the 32 oxygen ions of the anion sublattice of the spinel structure, and the

Fig. 6



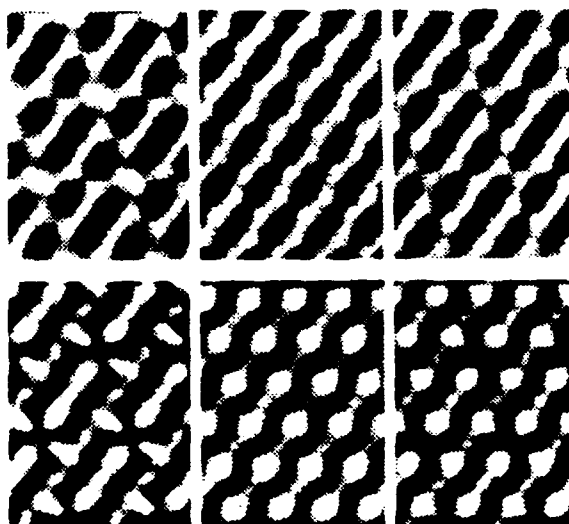
(a)



(b)

- (a) The background shows the enlarged average image from fig. A 1(c) in a type II specimen for  $\Delta f = -48$  nm. The insets are simulated images of Pd and  $\eta$ -Al<sub>2</sub>O<sub>3</sub> for  $t = 10$  nm and  $\Delta f = -48$  nm. The simulated images almost merge with the experimental image, indicating that the Al<sub>2</sub>O<sub>3</sub> phase is  $\eta$ -Al<sub>2</sub>O<sub>3</sub> (compare fig. 7). Since this particular contrast of the Al<sub>2</sub>O<sub>3</sub> does not reappear at greater thicknesses, the agreement between experiment and simulation indicates that the Al<sub>2</sub>O<sub>3</sub> and Pd have the same thicknesses close to the interface. In the Pd image the black dots correspond to Pd atom columns. In the Al<sub>2</sub>O<sub>3</sub> image the dark contrast between the bright diagonal {400} fringes corresponds to O and octahedral Al ions, whereas the bright {400} fringes indicate the location of tetrahedral Al cations. In particular, the tetrahedral 8 (a) sites are located at the bright links in the chains. (b) The background shows the average image of a detail from the right-hand side of the interface in the type II specimen shown in fig. 5(b) for  $\Delta f = -80$  nm. The insets are simulated images for Pd and  $\eta$ -Al<sub>2</sub>O<sub>3</sub> for  $t = 10$  nm and  $\Delta f = -80$  nm. The bright dots in the Pd image correspond to Pd atom columns in a  $\langle 110 \rangle$  direction. In the image of the Al<sub>2</sub>O<sub>3</sub> the bright dots indicate the location of O ion columns.

Fig. 7



Simulated images for  $\gamma$ -,  $\eta'$ - and  $\eta$ - $\text{Al}_2\text{O}_3$  (from left to right) for thickness  $t = 10$  nm for  $\Delta f = -48$  nm (upper row) and  $\Delta f = -80$  nm (lower row). The images of  $\eta$ - $\text{Al}_2\text{O}_3$  are the insets in figs. 6(a) and (b).

resulting phases are defective spinels. In  $\gamma$ - $\text{Al}_2\text{O}_3$  the Al cations are randomly distributed with an equal probability of 0.889 on 16(d) and 8(a) interstices (Wilson and McConnell 1980). In the cubic  $\eta'$ - $\text{Al}_2\text{O}_3$  phase (Ernst *et al.* 1990) the cations occupy 16(d) and 16(c) sites with an equal probability of 0.41. The occupancy of tetrahedral 8(a) and 48(f) sites is 0.14. Note that in  $\eta'$ - $\text{Al}_2\text{O}_3$  the cations are partially located in sites not belonging to the spinel structure. The same is true for  $\eta$ - $\text{Al}_2\text{O}_3$ , where the occupancies are 0.563 in 16(d), 0.269 in 16(c), 0.500 in 8(a) and 0.083 in 48(f) interstices (Shirasuka *et al.* 1976).

Image simulations for a range of thickness and defocus values were conducted for all three types of  $\text{Al}_2\text{O}_3$ . The following parameters were used for the image simulations with EMS: acceleration voltage, 800 kV; spherical aberration coefficient, 1.93 mm; focus spread, 14 nm; beam semiconvergence, 0.8 mrad; objective aperture radius,  $8 \text{ nm}^{-1}$ . The sampling frequency for all calculated images presented in this paper is such that the size of each sample is less than  $1 \times 10^{-2}$  nm in both the x and the y direction. In fig. 7 the results for  $t = 10$  nm and  $\Delta f = -48$  nm (upper row) and  $\Delta f = -80$  nm (lower row) are given for  $\gamma$ -,  $\eta'$ - and  $\eta$ - $\text{Al}_2\text{O}_3$ . A comparison with the averaged images in figs. 6(a) and (b) clearly shows that  $\gamma$ - $\text{Al}_2\text{O}_3$  can immediately be rejected, since the simulated images of  $\gamma$ - $\text{Al}_2\text{O}_3$  for both defocus values contain details that are not observed experimentally. The differences between the simulated images of  $\eta$  and  $\eta'$  are not very significant for  $\Delta f = -80$  nm. The experimentally observed chain-like bright contrast between every second pair of diagonal {400} fringes (see fig A 1(a)-(c)), however, is only present in the simulated image of  $\eta$ - $\text{Al}_2\text{O}_3$  for  $\Delta f = -48$  nm. This bright contrast is attributed to the high occupancy of tetrahedral 8(a) interstices which belong to the spinel structure. Therefore we conclude that the cubic spinel phase is  $\eta$ - $\text{Al}_2\text{O}_3$ .

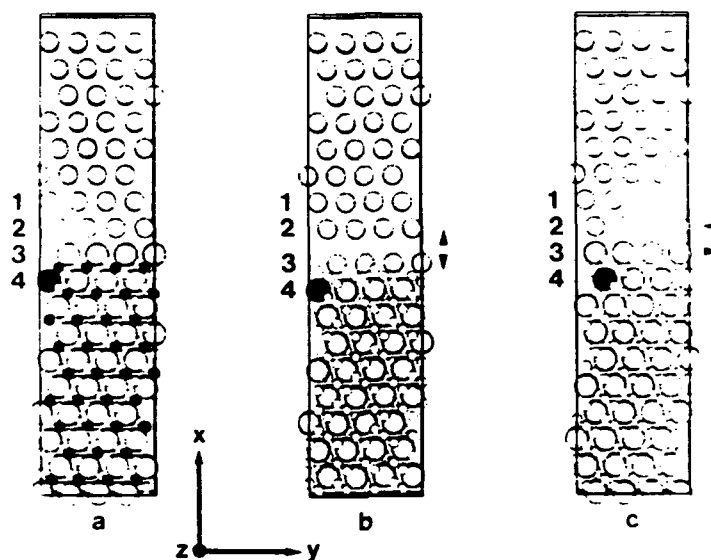
In addition, particles are observed which generate a HRTEM contrast close to that of  $\eta'$ -Al<sub>2</sub>O<sub>3</sub>. This observation requires a comment on the stability of the cubic spinel alumina particles under electron irradiation at 800 kV. HRTEM images were taken from the same particle at constant defocus but after different electron irradiation times (10 min between subsequent exposures). A dramatic change in contrast of the Al<sub>2</sub>O<sub>3</sub> is observed. This observation might indicate that electron irradiation at 800 kV induces a redistribution of Al cations in the metastable Al<sub>2</sub>O<sub>3</sub> compounds. Intuitively a redistribution of cations will lead to more disordered structures such as  $\eta'$ -Al<sub>2</sub>O<sub>3</sub>. Moreover, simulations for a  $\eta$ -Al<sub>2</sub>O<sub>3</sub> particle 10 nm thick revealed that a contrast similar to that of  $\eta'$ -Al<sub>2</sub>O<sub>3</sub> can be produced if the  $\eta$ -Al<sub>2</sub>O<sub>3</sub> particle is rotated by about 0.5° around a  $\langle 100 \rangle$  axis so that the incident electron beam is inclined by about 0.5° with respect to the  $\langle 110 \rangle$  zone axis. Therefore the characteristic contrast of  $\eta$ -Al<sub>2</sub>O<sub>3</sub> can only be observed after very short exposure times in particles with a  $\langle 110 \rangle$  zone axis exactly parallel to the electron beam. Practically these conditions cannot always be fulfilled. Consequently, it is assumed for the present study that particles with a HRTEM contrast close to that of  $\eta'$ -Al<sub>2</sub>O<sub>3</sub> were  $\eta$ -Al<sub>2</sub>O<sub>3</sub> particles prior to electron irradiation.

### 3.3. Structure of the Pd-Al<sub>2</sub>O<sub>3</sub> interface in a type II specimen

As shown before, there exists a fixed orientation relationship between Pd and  $\eta$ -Al<sub>2</sub>O<sub>3</sub>; however, the Pd- $\eta$ -Al<sub>2</sub>O<sub>3</sub> interface is incoherent. Firstly, this can be concluded from the absence of localized misfit dislocations (Eastman and Rühle 1989). An equivalent formulation would be that the misfit dislocations are delocalized. In addition, the inspection of HRTEM images shows almost no distortion in the metal near the interface and an atomic registry which is a linear function of the position at the interface (one example is shown in fig. 5(a)). Both features are typical of incoherent (incommensurate) interfaces (Gibson 1987). The incoherent nature of the interface makes image simulations difficult. Idealizing assumptions have to be made in the construction of the interface models for the image simulations. This may limit the validity of the present results. However, our simulations were performed for a large number of interface models, including models with grooves along the interface, with steps in the interface perpendicular to the electron beam and with various atomic distributions in the vicinity of the interface. Most models could immediately be rejected owing to obvious discrepancies between simulated and experimental images. It is therefore assumed that the real structure of the interface is closely approximated by the models discussed in the next section, where we use the interface in a type II specimen shown in figs. 4 and 5 for a detailed description of our image simulations.

Once the correspondence between the experimental contrast and the atomic positions in Pd and  $\eta$ -Al<sub>2</sub>O<sub>3</sub> is established (see figs. 6(a) and (b)), the relative positions of the Pd and Al<sub>2</sub>O<sub>3</sub>, that is the translation state of the adjoining lattices, can easily be determined. We first compare the experimentally observed geometries with idealized interface geometries using fig. 8 as an illustration. Different lattice planes parallel to the interface are numbered. In an idealized interface the f.c.c. lattice of Pd and the f.c.c. O ion sublattice of  $\eta$ -Al<sub>2</sub>O<sub>3</sub> would directly interpenetrate across the interface and the distance between the outermost Pd(111) plane (plane 2) and the outermost O(111) plane of  $\eta$ -Al<sub>2</sub>O<sub>3</sub> (plane 3) across the interface would be equal to the distance between Pd{111} planes (i.e.  $d_{111} = 0.224$  nm). This idealized configuration (coherent case) is depicted in fig. 8(a). The coherent case was not observed experimentally. Close inspection of the left-hand part of the interface in fig. 5 shows instead that there is an

Fig. 8



Three models of the Pd- $\eta$ -Al<sub>2</sub>O<sub>3</sub> interface in Pd<110> projection. The {111} planes close to the interface are numbered. (a) Coherent interface with the Al<sub>2</sub>O<sub>3</sub> terminated by O ions (large spheres in plane 3). The small black spheres are Al cations in octahedral interstices; the small bright spheres correspond to Al ions in tetrahedral interstices. (b) Geometrically correct model for the left-hand side of the interface in fig. 5 with a distance  $1.3d_{111}$  between planes 2 and 3. The outermost O ions in plane 3 are replaced by Pd atoms. This is the basic model for the simulations depicted in fig. 9. (c) Geometrically correct model of the right-hand side of the interface in fig. 5. Corresponding O ions in (a), (b) and (c) are marked black to indicate the relative translations parallel and perpendicular to the interface.

additional 'gap' of  $0.3d_{111}$  between the Pd and Al<sub>2</sub>O<sub>3</sub> lattices perpendicular to the interface. This geometry is depicted in fig. 8(b). On the right-hand part this 'gap' is not present but owing to the lattice parameter mismatch between metal and ceramic the Al<sub>2</sub>O<sub>3</sub> lattice is now shifted parallel to the interface when compared with the situation on the left-hand side (fig. 8(c)). Replacing the O ions in plane 3 by Pd atoms leaves the outermost Pd plane close to the octahedral and tetrahedral Al ions between planes 3 and 4, as shown in fig. 8(b). This replacement of O ions in plane 3 by Pd atoms is the basic difference in the models for Pd- $\eta$ -Al<sub>2</sub>O<sub>3</sub> interfaces with O-terminated and Al-terminated Al<sub>2</sub>O<sub>3</sub>. So far, the actual occupancies of atomic and ionic sites in the interfacial region have not yet been considered.

The models in fig. 8 represent the <110> projections of the 'supercells' used for the multislice calculations with EMS. The small lattice mismatch between Pd and  $\eta$ -Al<sub>2</sub>O<sub>3</sub> is compensated in the models by compressing the Al<sub>2</sub>O<sub>3</sub> unit cell by 2.7%. Then the required width of the model parallel to the interface (in the y direction) becomes rather small (0.953 nm). The interface is obtained by repetition of the supercell in the y direction. The correct distribution of Al ions in the <110> direction of the spinel (i.e. the z direction in the models) requires the construction of four different types of slice, each

with dimensions  $x=4.0403$  nm,  $y=0.9530$  nm and  $z=0.1376$  nm. The multislice iteration with the slice sequence A, B, C, D, A, B, ... was then repeated until the desired specimen thickness was reached.

The results of the simulations are now compared with the experimental images of the left-hand part of the interface in fig. 5. The translation state in this region of the interface is represented by the model in fig. 8(b) which stays fixed for all simulated images discussed below. The models for which the images in fig. 9 were calculated differ only in the occupancies of the atomic sites near the interface. The occupancies are varied until the optimum match between the simulated and the experimental image is reached for two different defocus values. In figs. 9(a)-(d) the simulated images are shown next to the respective portions of the experimental image in fig. 9(e). The characteristic features of the experimental images are

- (1) the bright, almost continuous contrast on the Pd side of plane 3 at  $\Delta f = -80$  nm,
- (2) the slightly smeared row of bright dots (corresponding to Pd atom columns) in plane 2 at  $\Delta f = -80$  nm,
- (3) the dark single dots on the Al<sub>2</sub>O<sub>3</sub> side of plane 3 at  $\Delta f = -80$  nm,
- (4) the bright contrast on the Pd and Al<sub>2</sub>O<sub>3</sub> sides of plane 2 at  $\Delta f = -48$  nm and
- (5) the slight truncation of the diagonal dark oval contrast between planes 3 and 4 at  $\Delta f = -48$  nm.

These features must be present in simulated images for both defocus values in order to show that a chosen model is consistent with the actual interfacial structure.

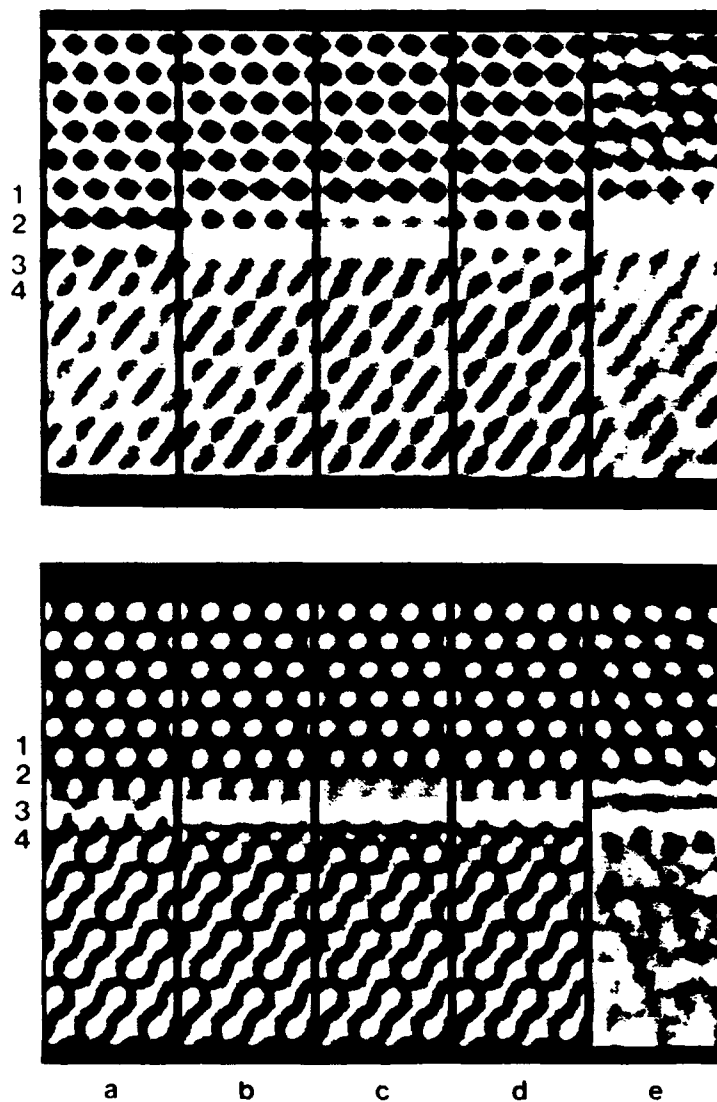
Figure 9(a) shows the results for the *O-terminated*  $\eta$ -Al<sub>2</sub>O<sub>3</sub>. At  $\Delta f = -48$  nm the  $\eta$ -Al<sub>2</sub>O<sub>3</sub> periodicity in the  $y$  direction (similarity of contrast between every second pair of {400} fringes) is maintained up to the terminating O layer. The gap between planes 2 and 3 appears as a bright band between the Pd and the Al<sub>2</sub>O<sub>3</sub>. At  $\Delta f = -80$  nm the gap creates bright contrast between planes 2 and 3, and the O ion columns are represented by bright dots in plane 3. Neither the  $\eta$ -Al<sub>2</sub>O<sub>3</sub> periodicity nor the distinct bright dots are observed experimentally at these locations. Therefore an O termination of the Al<sub>2</sub>O<sub>3</sub> particle is dismissed.

The results for different interfaces with *Al-terminated* Al<sub>2</sub>O<sub>3</sub> are given in figs. 9(b)-(d). Although the origin and the physical meaning of the 'gap' in the Pd close to the interface is not understood, the Al<sub>2</sub>O<sub>3</sub> side of the model for the simulations shown in fig. 9(b) is physically meaningful since it is expected that the Al ions adjacent to (noble) Pd atoms are in an ionization state different from that of Al ions in the Al<sub>2</sub>O<sub>3</sub>. Therefore they are probably 'larger' and thus more likely to occupy the larger octahedral sites. Al atoms are also assumed to occupy some of the Pd lattice sites in plane 3 owing to Al segregation to the interface. The lowered Pd occupancies in planes 3 and 2 account for this replacement of relatively heavy Pd atoms by Al atoms with a smaller scattering power. The models in figs. 9(b) and (c) differ only in the Pd occupancy in plane 2 which is 0.700 in fig. 9(b) and 0.600 in fig. 9(c).

The change from O to Al termination effects the simulated images in a characteristic way.

For  $\Delta f = -48$  nm, the even distribution of Al ions in all octahedral sites between planes 3 and 4 destroys the periodicity in the  $y$  direction typical of  $\eta$ -Al<sub>2</sub>O<sub>3</sub> and the contrast between each pair of {400} fringes looks alike. Furthermore, the length of the diagonal black ovals between planes 3 and 4 is reduced on the Pd side when compared

Fig. 9



Comparison of experimental and simulated HRTEM images of an interface in an Al annealed type II specimen for  $\Delta f = -48$  nm (upper row) and  $\Delta f = -80$  nm (lower row). (a)-(d) Simulated images for different interfacial compositions. (e) Detail of the experimental image (see the left-hand side of fig. 5). (a) O-terminated  $\eta$ - $\text{Al}_2\text{O}_3$ . (b) Al-terminated  $\text{Al}_2\text{O}_3$ . The O ions in plane 3 are replaced by Pd atoms which now sit next to the interstitial Al ions between planes 3 and 4 (compare model in fig. 8 (b)). The Pd occupancy in plane 3 is 0.600. Between plane 3 (Pd) and plane 4 (O), only the octahedral interstices are occupied with Al ions with a 40% probability. The Pd occupancy in plane 2 is 0.700. (c) Al-terminated  $\text{Al}_2\text{O}_3$  like (b). The Pd occupancy in plane 2 is reduced to 0.600. (d) Al-terminated  $\text{Al}_2\text{O}_3$  like (b). The tetrahedral sites between plane 4 and the occupied octahedral sites half-way between planes 3 and 4 are occupied with 0.200 probability, and the likelihood for lattice sites in the adjacent plane 4 to be occupied with O ions is 0.900. The Pd occupancy in plane 3 is set to 0.650. The Al-terminated models in (b) and (c) give the closest resemblance to the experimentally observed contrasts in (e); models (a) (O-termination) and (d) are dismissed.

with the image in fig. 9(a). Both features are observed experimentally (see figs. 5(a) and 6(a)). On the Pd side the decreasing site occupancy in plane 2 from 0.700 to 0.600 causes the distinct black contrast in plane 2 to disappear, so that fig. 9(c) matches perfectly with the experimental image.

For  $\Delta f = -80$  nm, the almost continuous bright contrast in plane 3 and the smeared bright dots in plane 2 are closely reproduced in the simulated images of the model in fig. 9(b). The further reduction in scattering power in plane 2 between the models in figs. 9(b) and (c), however, produces a wide bright band parallel to the interface in the simulated image in fig. 9(c). This is not observed experimentally. On the Al<sub>2</sub>O<sub>3</sub> side of the interface the experimentally observed row of dark contrasts between planes 3 and 4 is approximately reproduced by the simulations. The models in figs. 9(b) and (c) for the Al-terminated Al<sub>2</sub>O<sub>3</sub> described above are therefore believed to describe well the structure of the Al<sub>2</sub>O<sub>3</sub> close to the interface. As expected, the  $\eta$ -Al<sub>2</sub>O<sub>3</sub> precipitates in the type II specimen are bounded by Al ions and Al seems to segregate in the two near-interface {111} planes of Pd. The latter conclusion, however, is not unambiguous since it is not clear what the structure of the Pd is in the vicinity of the Al<sub>2</sub>O<sub>3</sub>.

In fig. 9(d) the effects of small changes in the models are demonstrated in order to prove the sensitivity of image simulations. The occupation of tetrahedral interstices close to plane 4 with Al ions and the reduction of the O occupancy from 1 to 0.900 in plane 4 darkens the contrast in this region for  $\Delta f = -48$  nm. This is not observed experimentally and it indicates that the changes in the Al<sub>2</sub>O<sub>3</sub> structure are restricted to the two outermost {111} planes next to the interface. For  $\Delta f = -80$  nm the intensity of the bright dots representing O ion columns in plane 4 is slightly decreased. With reference to fig. 6(b) it can be seen that this is not apparent in the experimental image. The increased occupancy for Pd sites in plane 3 darkens the location of the respective atom columns for  $\Delta f = -48$  nm, and more distinct white dots develop for  $\Delta f = -80$  nm. This example demonstrates that local changes in a model affect the HRTEM image only locally which reflects the 'projection character' of HRTEM microscopy. It also demonstrates that the changes in the structure of the Al<sub>2</sub>O<sub>3</sub> are restricted to the outermost region between the O ions in plane 4 and the interface.

The aperiodic character of the Pd- $\eta$ -Al<sub>2</sub>O<sub>3</sub> interface makes image simulations with reasonably sized structure models difficult and a perfect match between experimental and simulated images cannot be reached. This is especially true for the Pd image close to the interface, since it can be expected that most of the accommodation between metal and ceramic takes place in the (elastically soft) metal. It appears that there are no preferred atom-to-atom positions at the interfaces of the particles. This can be rationalized by considering the bond strength between Pd and the atoms at the ceramic side of the interface. No stable Pd oxide exists above about 1143 K (Raub and Plate 1957). This supports our intuition of a weak bond between the noble Pd and O at the temperatures used for the oxidation. The (presumably) weak Pd-O bonds at the interface allow for small changes of relative positions of Pd atoms and O ions without a dramatic increase in interfacial energy. Therefore it is energetically favourable for the system to form an interface with a variety of relative positions for Pd atoms and O ions. This is consistent with the apparent absence of misfit dislocations in the Pd- $\eta$ -Al<sub>2</sub>O<sub>3</sub> interfaces. Interestingly, Anderson, Ravimohan and Mehandru (1987) also do not find 'strong support for the pre-eminence of the importance of lattice matching' from their structure calculations of Pt- $\alpha$ -Al<sub>2</sub>O<sub>3</sub> interfaces where Pt bonds weakly to the O at the interface. In contrast, in systems with strong metal-O bonds, such as Nb-Al<sub>2</sub>O<sub>3</sub> (Mader and Necker 1990, Meyer, Flynn and Rühle 1990), small changes in relative

positions of metal and O away from the arrangement with the lowest free energy will lead to a high-energy configuration. Therefore this system prefers to form large approximately coherent interfacial areas, and the mismatch is accommodated by misfit dislocations at the interface (Mayer *et al.* 1990) or at a small stand-off distance away from the interface (Mader 1987).

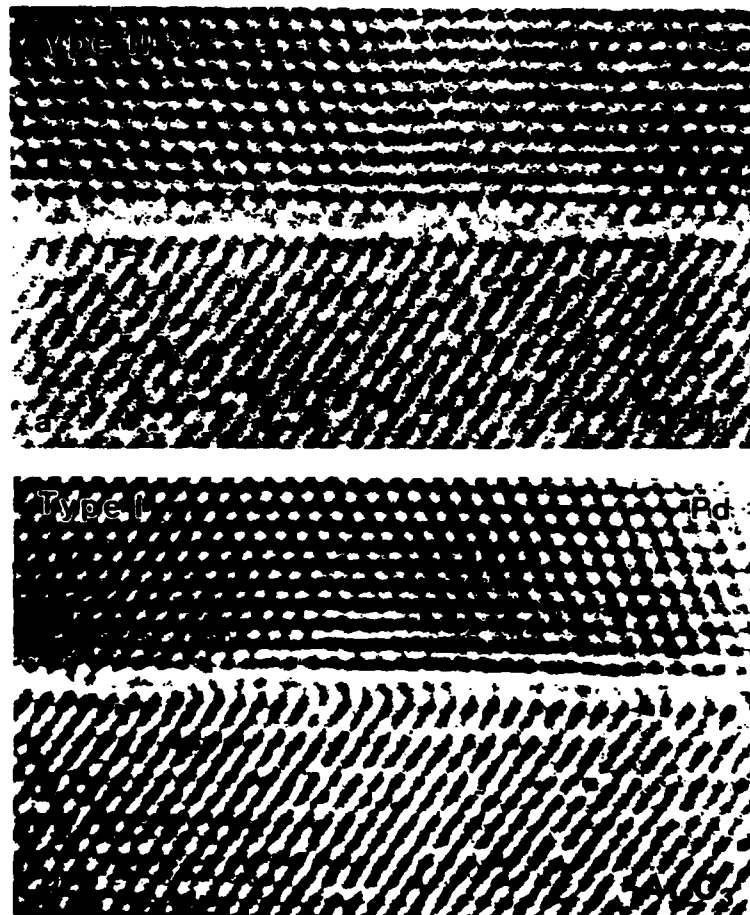
The above reasoning is based on the assumption of a weak Pd–O bond and might therefore hold for Pd–Al<sub>2</sub>O<sub>3</sub> interfaces formed under O excess during the initial oxidation process. Pd and O atoms are then expected to be in contact at the interfaces. The bonding situation at the interfaces is more complex after the annealing under Al excess. The simulations show that then Pd and Al are close neighbours at the interface, and one has to take into consideration that Pd forms strong bonds with Al. Strong Pd–Al bonds can be expected from the large heat of solution of Al in Pd (Klomp 1987) and from the fact that there exist several intermetallic phases in the Pd–Al system (Massalski, Murray, Bennett and Baker 1986). Fischmeister (1987) used the high affinity between Al and Pd to rationalize the unexpectedly strong bonds that form between Pd (and Pt) and Al<sub>2</sub>O<sub>3</sub> (McLean and Hondros 1971, Klomp 1972). The basic argument is that O ions in the alumina form bonds with Al atoms bound in the noble metal close to the interface. The strength of the Pd–Al bond might imply that our purely geometric approach, used to construct the Pd side of the model interfaces for the simulations, is too simple. Owing to the formation of strong Pd–Al bonds the positions of Pd and Al atoms in planes 2 and 3 might deviate from the Pd positions in pure Pd. The existence of the 'gap' on the Pd side of the model in fig. 9(b) may therefore be attributed to strong Pd–Al bonds between the terminating Pd plane and the adjacent interstitial Al ions. The simulation models used so far do not include geometric rearrangements of atoms at the interface. More realistic (and consequently larger) models should account for atomic rearrangements. The nature of possible relaxations might be elucidated by structure calculations of Pd– $\eta$ -Al<sub>2</sub>O<sub>3</sub> interfaces.

#### 3.4. Comparison between interfaces in type I and type II specimens

The structures on the Pd side of the interfaces deviate from the idealized structures assumed in the simulations. Relative shifts between the lattices of Pd and Al<sub>2</sub>O<sub>3</sub> parallel and perpendicular to the interfaces have been observed in type I and type II specimens. It has not been possible to obtain a through-focus series of HRTEM images from a Pd– $\eta$ -Al<sub>2</sub>O<sub>3</sub> interface in a type I specimen with an interface geometry and thickness directly comparable with the interface described in § 3.3. Therefore we restrict ourselves to a qualitative comparison between HRTEM images of Pd– $\eta$ -Al<sub>2</sub>O<sub>3</sub> interfaces in type I and type II specimens and concentrate on the contrast in the Al<sub>2</sub>O<sub>3</sub> close to the interface.

The image of the Pd– $\eta$ -Al<sub>2</sub>O<sub>3</sub> interface in a type II specimen is shown in fig. 10 together with a representative HRTEM image of a Pd– $\eta$ -Al<sub>2</sub>O<sub>3</sub> interface in a type I specimen. For the type I interface (fig. 10(b)) the length of the diagonal black ovals near the interface (arrows) equals the length of the ovals in the Al<sub>2</sub>O<sub>3</sub> away from the interface, and neighbouring black ovals look alike (no  $\eta$  periodicity parallel to the interface). In the type II specimen (fig. 10(a)) there is also no  $\eta$  periodicity parallel to the interface, but the ovals appear to be shortened adjacent to the interface. These differences are presumably due to differences in the near-interface compositions of the Al<sub>2</sub>O<sub>3</sub>, as can be seen from the simulated images (fig. 11). Figure 11(a) shows the O-terminated Al<sub>2</sub>O<sub>3</sub>, if the cation distribution of  $\eta$ -Al<sub>2</sub>O<sub>3</sub> is maintained up to the terminating O ions in plane 3. The  $\eta$  periodicity parallel to the interface is maintained

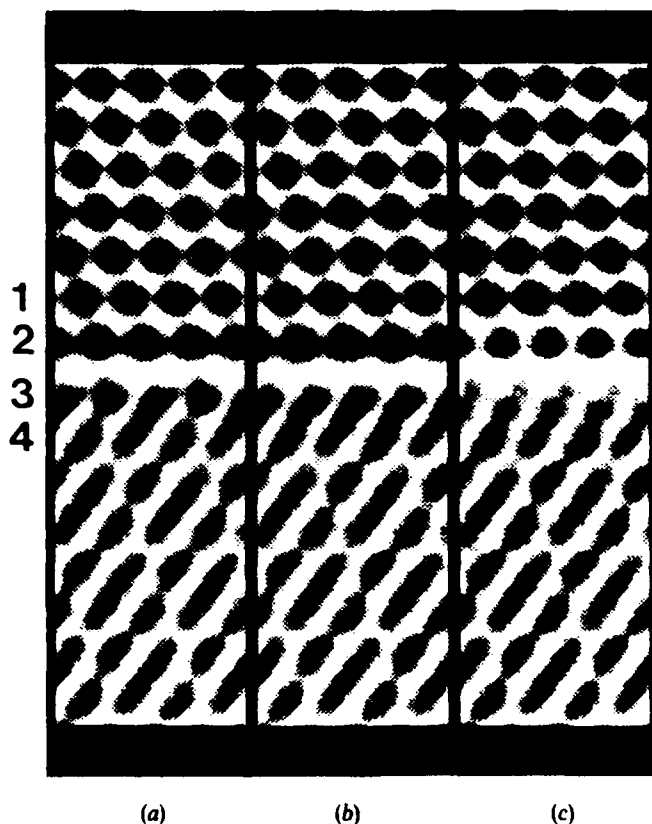
Fig. 10



Comparison between the near-interface contrast in (a) an Al annealed type II specimen and (b) an as-oxidized type I specimen. The interfaces have approximately the same thicknesses and the HRTEM images were taken at about the Scherzer focus of the ARM. Note the differences in the lengths of the diagonal oval contrasts close to the interfaces (arrows). Compare these with the corresponding features in the simulated images in fig. 11.

up to the outermost O layer, which is not found experimentally. The periodicity  $d_{11}$  appears if Al ions are evenly distributed in all octahedral sites between planes 3 and 4. In the model corresponding to the simulated image in fig. 11 (b) these sites have an occupancy of 0.600. This value is approximately consistent with the Al<sub>2</sub>O<sub>3</sub> bulk stoichiometry. The even distribution of Al ions in octahedral sites between planes 3 and 4 destroys the  $\eta$  periodicity parallel to the interface and produces the experimentally observed contrast. The experimental images of interfaces in type I specimens are therefore consistent with an Al<sub>2</sub>O<sub>3</sub> in which firstly the Al<sub>2</sub>O<sub>3</sub> is terminated by O ions, and secondly the Al cation distribution close to the terminating O layer is not equal to

Fig. 11



Simulated images of (a), (b) two different O-terminated  $\text{Al}_2\text{O}_3$  compounds and (c) the Al-terminated  $\text{Al}_2\text{O}_3$  which is also shown in fig. 9(b). All simulations are for  $\Delta f = -48$  nm and  $t = 10$  nm. (a) O-terminated  $\eta\text{-Al}_2\text{O}_3$ . (b) O-terminated  $\eta\text{-Al}_2\text{O}_3$ , where only the octahedral interstices between the close-packed O ion planes 3 and 4 are occupied with Al ions with occupancy 0.600. The even distribution of Al ions in octahedral sites between planes 3 and 4 destroys the  $\eta$  periodicity parallel to the interface. This contrast is typical of that observed in type I specimens. (c) Al-terminated  $\eta\text{-Al}_2\text{O}_3$ . This contrast with the truncated dark ovals was observed in type II specimens.

the cation distribution in the  $\text{Al}_2\text{O}_3$  away from the interface. The contrast of the Al-terminated  $\text{Al}_2\text{O}_3$  with the shortened black ovals is given in fig. 11(c) for a direct comparison. This contrast is not observed in type I specimens.

The comparison of type I (O) and type II (Al) specimens leads to the following conclusions. After oxidation the ceramic particles are terminated by O ions, as has been found for alumina precipitates in Cu (Ernst *et al.* 1991) and for CdO particles in Ag (Necker and Mader 1988). The cation distribution between the two close-packed O planes closest to the interface differs from that of bulk  $\eta\text{-Al}_2\text{O}_3$ . This suggests that interactions between Pd and Al at the interface are possible even if Pd and Al atoms are separated by a close-packed O layer. This interaction might be a direct long-range interaction between Pd and Al, analogous to that which emerged from theoretical

calculations on  $\alpha$ -Al<sub>2</sub>O<sub>3</sub>-Pt interfaces (Anderson *et al.* 1987). The interaction can also be thought of as an oxidation of Pd, which in turn alters the bonding between O ions in the outermost layer and adjacent Al ions. The characteristic contrast differences at the interfaces in type I and type II specimens suggest that the annealing in Al vapour actually modifies the composition of the interfaces in internally oxidized Pd-Al. This is consistent with the conclusions of Huang *et al.* (1988).

#### §4. SUMMARY AND CONCLUSIONS

- (1) During internal oxidation the nucleation and growth of the thermodynamically stable  $\alpha$ -Al<sub>2</sub>O<sub>3</sub> is favoured at grain boundaries owing to their open structure and high Al and O activities in these two-dimensional defects. The unknown structure of the incoherent intragranular type B particles is assumed to be caused by the specific nucleation-and-growth conditions within the matrix of the Pd-Al alloy during internal oxidation. All intragranular type A particles in Pd-3 at.% Al alloys internally oxidized at 1273 K have a cubic close packing of O anions. Generally, close-packed planes of the ceramic are parallel to close-packed planes in Pd. It is concluded that type A particles nucleate parallel to {111} planes of Pd and that the nucleation and growth of precipitates with a f.c.c. anion sublattice is favoured within the f.c.c. Pd matrix. From a comparison of simulated and processed experimental images the cubic spinel-type phase was identified as  $\eta$ -Al<sub>2</sub>O<sub>3</sub>.
- (2) The changes in the structure of  $\eta$ -Al<sub>2</sub>O<sub>3</sub> due to annealing in air and Al respectively are restricted to the two outermost {111} planes of the alumina in both cases. A subtle difference can be identified between HRTEM images of the Pd- $\eta$ -Al<sub>2</sub>O<sub>3</sub> interfaces in as-oxidized (type I) and Al annealed (type II) samples.
- (3) The experimental contrast of the Pd- $\eta$ -Al<sub>2</sub>O<sub>3</sub> interface in an Al annealed (type II) specimen has been analysed in detail. It is similar to the calculated contrast of a model structure in which the Al<sub>2</sub>O<sub>3</sub> is terminated by Al ions located in octahedral interstices between a close-packed plane in the metal and a close-packed O ion plane in the Al<sub>2</sub>O<sub>3</sub> and where Al is segregated in the metal close to the interface. The experimental contrast of Pd- $\eta$ -Al<sub>2</sub>O<sub>3</sub> interfaces in oxidized (type I) samples are qualitatively consistent with the expected O termination of the alumina. Our results therefore support the interpretation of the H-trapping experiments by Huang *et al.* (1988).
- (4) Pd- $\eta$ -Al<sub>2</sub>O<sub>3</sub> interfaces are difficult to study using HRTEM because of the instability of  $\eta$ -Al<sub>2</sub>O<sub>3</sub> under electron irradiation at 800 kV, which limits the observation time to a few minutes. In addition, relaxations at the interface and the incoherent nature of the phase boundary require idealizing assumptions to be made in the interface modelling. Therefore a quantitative unambiguous determination of the interface structure has not yet been possible.

#### ACKNOWLEDGMENTS

This work was supported by the Office of Naval Research under Contract No. N00014-89-J-1764 and by the Volkswagen Stiftung under Contract No. I162802. The authors gratefully acknowledge the use of the ARM at the National Center for Electron Microscopy in Berkeley, U.S.A., and the assistance of Chris Nelson during the

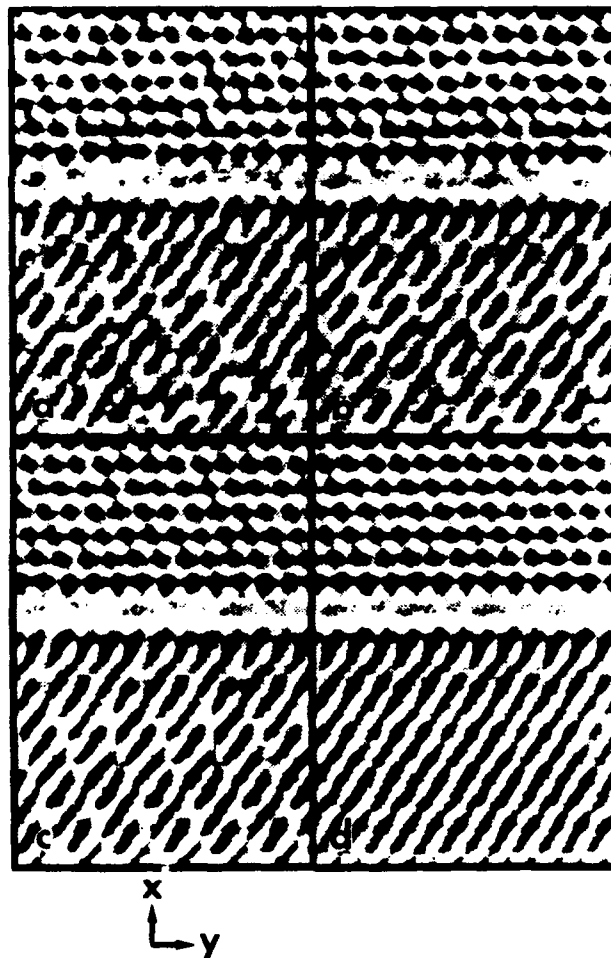
experiments. They also thank X. Y. Huang for providing the Al annealed samples, J. Mayer for valuable discussions and D. Loretto for critical comments on the manuscript.

## APPENDIX

### *Computerized image averaging*

Image details with a size of  $13\text{ nm} \times 13\text{ nm}$  were digitized from the micrograph negatives and stored into arrays of  $512 \times 512$  image points (pixels). The grey values of the pixels vary between 0 and 255. The images (cf. fig. 5) were digitized with this

Fig. A 1



The effect of computerized image averaging. The images in (b), (c) and (d) are averaged images of the unprocessed image area in (a) which is a detail of fig. 5(a). See text for details of the averaging procedure.

resolution, and the boxed detail from fig. 5(a) (see fig. A 1(a)) is used for the demonstration. The selected area is sufficiently small that a constant thickness and defocus can be assumed for the entire area. In addition, the effect of the lattice mismatch between the Pd and the Al<sub>2</sub>O<sub>3</sub> is negligible on this small scale, so that the averaging of the contrast in the Pd and the Al<sub>2</sub>O<sub>3</sub> can be performed in one procedure.

The selected area contains 12 Pd atom columns in a Pd{111} plane parallel to the interface (in the *y* direction). The image is divided into *n<sub>y</sub>* subimages with identical width in the *y* direction and the intensities (grey values) of corresponding locations in the subimages are added and finally normalized. The averaged image then contains *n<sub>y</sub>* times the normalized sum of intensities patched together in *y* direction. Figures A 1(b), (c) and (d) show the average images for *n<sub>y</sub>* = 2, 3 and 4 respectively. It can be seen that for *n<sub>y</sub>* = 2 and *n<sub>y</sub>* = 3 the average image reproduces the periodic information contained in fig. A 1(a) for Pd as well as for the Al<sub>2</sub>O<sub>3</sub>, and that the quality of the image is improving with increasing *n<sub>y</sub>*. In fig. A 1(d) the Pd image is further improved, but there is a loss of information for the Al<sub>2</sub>O<sub>3</sub>. Thus *n<sub>y</sub>* = 4 is obviously not compatible with the periodicity of the Al<sub>2</sub>O<sub>3</sub> image parallel to the interface. In fact, the characteristic feature of the image, namely the chain-like contrast between every second pair of diagonal {400} fringes is repeated six times in the *y* direction in fig. A 1(a), and 4 is not an integer divisor of 6. Consequently, the subimages obtained for *n<sub>y</sub>* = 2 and *n<sub>y</sub>* = 3 are two-dimensional 'unit cells' in the *y* direction of the image in fig. A 1(a), and the subimage obtained for *n<sub>y</sub>* = 4 is not. It must be emphasized that these arguments do not apply for the interfacial region, for which the periodicity can be quite different from that of Pd or Al<sub>2</sub>O<sub>3</sub>. Note that fig. A 1(a) shows dark contrast details in the interfacial region which are completely lost in fig. A 1(d).

#### REFERENCES

- ANDERSON, A. B., RAVIMOHAN, C., and MEHANDRU, S. P., 1987, *Surf. Sci.*, **183**, 438.  
 BOURRET, A., 1989, *High Resolution Microscopy of Materials*, Materials Research Society Symposium Proceedings, Vol. 139, edited by W. Krakow, F. A. Ponce and D. A. Smith (Pittsburgh, Pennsylvania: Materials Research Society), p. 3.  
 BUSECK, P. R., COWLEY, J. M., and EYRING, L., 1988, *High Resolution Transmission Electron Microscopy* (Oxford: Oxford University Press).  
 DEBRUIN, H. J., MOODIE, A. F., and WARBLE, C. E., 1972, *J. Mater. Sci.*, **7**, 909.  
 EASTMAN, J. A., and RÜHLE, M., 1989, *Ceram. Eng. Sci. Proc.*, **10**, 1515.  
 ERNST, F., PIROUZ, P., and HEUER, A., 1991, *Phil. Mag.*, **A**, **63** 259.  
 FISCHMEISTER, H. F., 1987, *Ceramic Microstructures '86, Role of Interfaces*, edited by J. A. Pask and A. G. Evans (New York: Plenum), p. 1.  
 FISCHMEISTER, H. F., MADER, W., GIBBESCH, B., and ELSSNER, G., 1988, *Interfacial Structure, Properties and Design*, Materials Research Society Symposium Proceedings, Vol. 122 (Pittsburgh, Pennsylvania: Materials Research Society), p. 529.  
 GIBSON, J. M., 1987, *Silicon Molecular Beam Epitaxy*, edited by J. C. Bean and E. Kasper (Boca Raton, Florida: Chemical Rubber Company Press), chap. 3.  
 HUANG, X. Y., MADER, W., EASTMAN, J. A., and KIRCHHEIM, R., 1988, *Scripta metall.*, **22**, 1109.  
 HAHN, T., 1987, *International Tables for Crystallography*, second edition (Dordrecht: Reidel).  
 JAYARAM, V., and LEVY, C. G., 1989, *Acta metall.*, **37**, 569.  
 KLOMP, J. T., 1972, *Bull. Am. Ceram. Soc.*, **51**, 683; 1987, *Fundamentals of Diffusion Bonding*, edited by Y. Ichida (Amsterdam: Elsevier), p. 3.  
 KRAKOW, W., and SMITH, D. A., 1986, *J. Mater. Res.*, **1**, 47.  
 LEJUS, A. M., 1964, *Rev. Int. Hautes Temp. Réfract.*, **1**, 53.  
 LEVY, C. G., JAYARAM, V., VALENCIA, J. J., and MEHRABIAN, R., 1988, *J. Mater. Res.*, **3**, 969.  
 LIPPENS, B. C., and DEBOER, H. J., 1964, *Acta crystallogr.*, **17**, 1312.

- MADER, W., 1987, *Characterization of Defects in Materials*, Materials Research Society Symposium Proceedings, Vol. 82 (Pittsburgh, Pennsylvania: Materials Research Society), p. 403.
- MADER, W., and NECKER, G., 1990, *Metal-Ceramic Interfaces*, edited by M. Rühle, A. G. Evans, M. F. Ashby and J. P. Hirth (Oxford: Pergamon), p. 222.
- MASSALSKI, T. B., MURRAY, J. L., BENNETT, L. H., and BAKER, H., 1986, *Binary Alloy Phase Diagrams* (Metals Park, Ohio: American Society for Metals), p. 148.
- MAYER, J., FLYNN, C. P., and RÜHLE, M., 1990, *Ultramicroscopy*, **33**, 51.
- MCLEAN, M., and HONDROS, E. D., 1971, *J. Mater. Sci.*, **6**, 19.
- MEIJERING, J. L., 1971, *Adv. Mater. Res.*, **5**, 1.
- NECKER, G., and MADER, W., 1988, *Phil. Mag. Lett.*, **58**, 205.
- PIROUZ, P., and ERNST, F., 1990, *Metal-Ceramic Interfaces*, edited by M. Rühle, A. G. Evans, M. F. Ashby and J. P. Hirth (Oxford: Pergamon), p. 199.
- RAUB, E., and PLATE, W., 1957, *Z. Metallk.*, **48**, 529.
- SAALFELD, H., and MEHROTRA, B., 1965, *Ber. Deut. Keram. Ges.*, **42**, 161.
- SHIRASUKA, K., YANAGIDA, H., and YAMAGUCHI, G., 1976, *J. Ceram. Soc. Japan*, **84**, 610.
- SMITH, A. R., and EYRING, L. R., 1982, *Ultramicroscopy*, **8**, 65.
- STADELMANN, P. A., 1987, *Ultramicroscopy*, **21**, 131.
- WILSON, S. J., and MCCONNELL, J. D. C., 1980, *J. solid-st. Chem.*, **34**, 315.
- YAMAGUCHI, G., YASUI, I., and CHU, W.-C., 1970, *Bull. chem. Soc. Japan*, **43**, 2487.

## HREM STUDIES OF Pd/Al<sub>2</sub>O<sub>3</sub> INTERFACES

Thomas Muschik and Manfred Rühle

HREM studies were performed at Pd/Al<sub>2</sub>O<sub>3</sub> interfaces formed after internal oxidation<sup>1</sup> of Pd-Al alloys (5 at.%) at ambient pressure for 24 h at 1273 K. Oxidized foils (Type I) were studied, as well as some specimens which were subsequently annealed for 1 h at 1273 K in Al vapor (Type II). The atomistic structure was evaluated by HREM studies, at the ARM in Berkeley (800 kV, C<sub>s</sub> = 1.3 mm, Δf ~ 14 nm).

### References

1. W. Mader, *Mat. Res. Soc. Symp. Proc.* 82: 403, 1987.
2. X. Y. Huang et al., *Scripta Met.* 22: 109, 1988.

### Results

A typical example of an Al<sub>2</sub>O<sub>3</sub> precipitate in Pd matrix is shown in Fig. 1. Diffraction studies show that close-packed planes of the ceramic are parallel to close-packed planes in the Pd. Quantitative HREM revealed that the precipitate consists of η-Al<sub>2</sub>O<sub>3</sub>, which possesses a cubic spinel structure and whose particles are quite frequently twinned. The perfect lattices of the simulated and experimentally obtained image agree quite well (Fig. 2). The translation stage between the Pd and η-Al<sub>2</sub>O<sub>3</sub> can be determined from Fig. 2.

Annealing in air and Al, respectively, resulted in a change of the structure of η-Al<sub>2</sub>O<sub>3</sub> in regions up to the two outermost [111] planes of the alumina in both cases. A subtle difference can be identified between HRTEM images of the Pd/η-Al<sub>2</sub>O<sub>3</sub> interfaces in as-oxidized (Type I) and Al annealed (Type II) samples (Fig. 3).

### Interpretation and Conclusion

The experimental contrast of the Pd/η-Al<sub>2</sub>O<sub>3</sub> interface in an Al annealed (Type II) specimen has been analyzed in detail. It is similar to the calculated contrast of a model structure in which the η-Al<sub>2</sub>O<sub>3</sub> is terminated by Al ions located at octahedral interstices between a close-packed plane in the metal, and a close-packed oxygen ion plane in the alumina, and where Al is segregated in the metal close to the interface. The experimental contrast of Pd/η-Al<sub>2</sub>O<sub>3</sub> interfaces in oxidized (Type I) samples are qualitatively consistent with the expected oxygen termination of the alumina. The results therefore support the interpretation of the hydrogen trapping experiments.<sup>2</sup>

The authors are at the Max-Planck-Institut für Metallforschung, Seestr. 92, D-7000 Stuttgart 1, Germany (formerly at the Materials Department, University of California, Santa Barbara, CA 93106). This work was supported by the Office of Naval Research under contract N00014-89-J-1764 and by the Volkswagen Stiftung under contract I/62802. The authors acknowledge the use of the ARM at the NCEM in Berkeley, Calif.

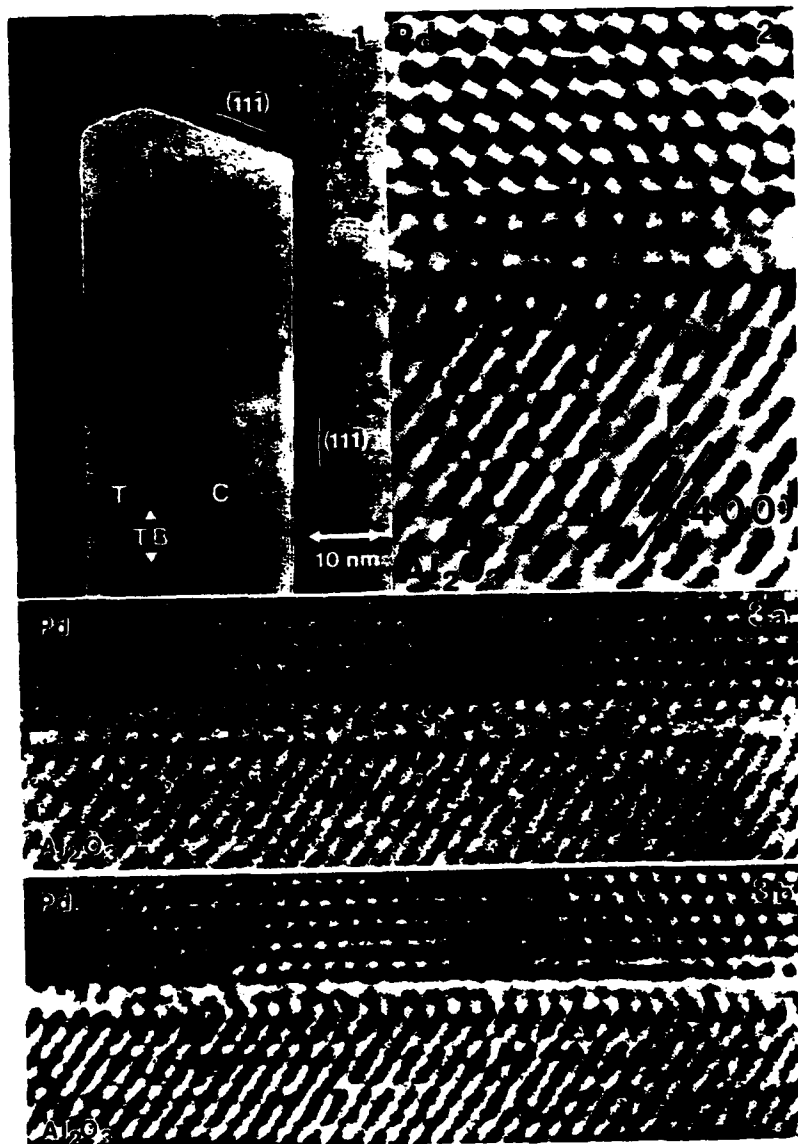


FIG. 1.--HRTEM image of typical twinned  $\eta$ - $\text{Al}_2\text{O}_3$  particle in Pd (110 projection). The twinned boundary (TB) separates parts with cube on cube orientation relationship with matrix (C) from twinned relation parts (T).

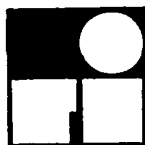
FIG. 2.--Comparison between experimental and computer-simulated images. Excellent fit is obtained in both parts,  $\eta$ - $\text{Al}_2\text{O}_3$  and Pd.

FIG. 3.--Comparison between near interface contrast in (a) aluminum annealed type II specimen, (b) as-oxidized type I specimen. The crystals have approximately the same thickness; HRTEM images were taken at about the Scherzer focus of the ARM.

**Sonderdruck aus:**

ZEITSCHRIFT FÜR  
**METALLKUNDE**

Herausgegeben von  
DER DEUTSCHEN GESELLSCHAFT FÜR METALLKUNDE EV.



**DR. RIEDERER-VERLAG GMBH**  
POSTFACH 104052  
7000 STUTTGART 1

# The Role of Oxygen for the Spinel Interphase Formation at Diffusion-Bonded Ni/Al<sub>2</sub>O<sub>3</sub> Interfaces<sup>1)</sup>

Kevin P. Trumble\* \*\* and Manfred Rühle\*

(\*Max-Planck-Institut für Metallforschung, Institut für Werkstoffwissenschaft, Seestr. 92, D-7000 Stuttgart 10, and \*\*Materials Department, University of California at Santa Barbara, Santa Barbara, CA, USA)

Dedicated to Professor Dr. rer. nat. Dr.-Ing. E. h. Hans-Jürgen Engell on the occasion of his 65th birthday

Sapphire single crystals were diffusion bonded to Ni polycrystalline foils which contained controlled amounts of dissolved oxygen. The experimental observations suggest that a threshold oxygen activity is required for the formation of a spinel interphase layer at the Ni/Al<sub>2</sub>O<sub>3</sub> interface. Thermodynamic calculations confirm that the threshold oxygen level necessary to stabilize the spinel increases from 0.006 at.% (60 at.ppm) at 1273 K to 0.025 at.% (250 at.ppm) at 1663 K. Further analysis indicated that the spinel exhibits a maximum thickness determined by the difference between initial and threshold oxygen concentrations and the Ni foil thickness. Considering the solubility limit of oxygen in solid Ni, the spinel thickness is limited to  $\approx 0.005$  times the Ni foil thickness.

## Der Einfluß des Sauerstoffes auf die Spinelreaktionsschichtbildung an diffusionsverschweißten Ni/Al<sub>2</sub>O<sub>3</sub> Grenzflächen

Saphireinkristalle wurden mit polykristallinen Nickelfolien verschweißt, in denen eine wohldefinierte Menge von Sauerstoff gelöst war. Die experimentellen Beobachtungen legen nahe, daß ein Schwellwert der Sauerstoffaktivität zur Ausbildung einer Spinelreaktionsschicht (NiAl<sub>2</sub>O<sub>4</sub>) an der Ni/Al<sub>2</sub>O<sub>3</sub> Grenzfläche erforderlich ist. Thermodynamische Berechnungen bestätigen die experimentellen Befunde. Der zur Stabilisierung der Spinelsschicht erforderliche Wert der Sauerstoffaktivität steigt von 0,006 At.-% (60 At.ppm) bei 1273 K auf 0,025 At.-% (250 At.ppm) bei 1663 K an. Eine weitergehende Analyse zeigt, daß die maximale Dicke der Spinellschicht aus der Differenz zwischen der Ausgangs- und Schwellwertkonzentration des Sauerstoffes und aus der Dicke der Nickelfolie bestimmbar ist. Aufgrund der Löslichkeitsgrenze des Sauerstoffes in Nickel ist die Spinelldicke auf das 0,005fache der Nickelfilmdicke begrenzt.

## 1 Introduction

Physical interactions on an atomic scale give rise to atomic bonding between many metals and ceramics and provide the basic for an understanding of the fundamental quantity, the work of adhesion. The atomic bonding and structure at metal/ceramic interfaces has been extensively studied since the 1960's<sup>1)</sup>. Recently, fracture mechanics considerations have led to the appreciation of additional contributions to interface fracture resistance for metal plasticity<sup>2)</sup> and interface roughness<sup>3)</sup>. However, metal/ceramic interfaces are generally formed by high temperature processes and are often exposed to high temperatures in service. At high temperatures chemical reactivity becomes an important issue. Chemical processes at metal/ceramic interfaces typically occur on a scale of micrometers or larger and include impurity segregation, interdiffusion, solutionization and reprecipitation, and the formation of intermediate phases (interphases). The resulting changes in interface microstructure and microchemistry often have dramatic effects on interface fracture resistance and are thus the ultimate consideration limiting the application of many metal/ceramic systems. Interphase formation represents perhaps the extreme case of metal/ceramic reactivity. This study explores interphase formation at the Ni/Al<sub>2</sub>O<sub>3</sub> interface.

Nickel aluminate spinel (Ni/Al<sub>2</sub>O<sub>4</sub>) interphase or reaction layers have been found to form at the interface between solid Ni and  $\alpha$ -Al<sub>2</sub>O<sub>3</sub> in numerous diffusion bonding studies<sup>4) to 7)</sup>. Although phenomenologically established, the underlying reaction process by which spinel formation

occurs at the Ni/Al<sub>2</sub>O<sub>3</sub> interface is not well understood. Previous investigators<sup>7)9)</sup> have proposed that the reaction must proceed through a NiO intermediate; that is, the Ni is somehow first oxidized to NiO which then reacts with the Al<sub>2</sub>O<sub>3</sub> in the well known spinel formation reaction between NiO and Al<sub>2</sub>O<sub>3</sub>. There is some experimental evidence<sup>10) to 12)</sup>, suggesting oxygen may play a role in spinel formation at the Ni/Al<sub>2</sub>O<sub>3</sub> interface but an oxygen activity dependence of spinel formation has not been clearly established or expressed in quantitative terms.

The effect is spinel interphase formation on the mechanical integrity of the Ni/Al<sub>2</sub>O<sub>3</sub> interface is also not well understood, as evinced by contradictory accounts in the literature. Some investigators<sup>7)9)</sup> claim spinel formation represents a sort of "reaction bonding" leading to strong interfaces, whereas others<sup>4)5)</sup> consider it to have a severe weakening effect. In either case, an understanding of the processing conditions and reaction mechanism leading to spinel formation is key to optimizing interface fracture resistance.

The present study focuses on spinel formation at the Ni/Al<sub>2</sub>O<sub>3</sub> interface, and in particular the role of oxygen, through a combined approach of controlled oxygen diffusion bonding experiments and equilibrium thermodynamic calculations.

## 2 Experimental Procedures and Observations

### 2.1 High Vacuum Ni/Al<sub>2</sub>O<sub>3</sub> Diffusion Bonding

In an earlier study<sup>13)</sup>, polycrystalline Ni (99.94 %) sheet 1.5 mm thick was diffusion bonded to  $\alpha$ -Al<sub>2</sub>O<sub>3</sub> single crys-

<sup>1)</sup> Presented at the "Hauptversammlung 1990 der Deutschen Gesellschaft für Materialkunde" in Osnabrück.

tals (basal plane || bond plane) in a high vacuum of  $\sim 1 \times 10^{-3}$  Pa ( $10^{-6}$  atm) at 1663 K (1390 °C) for 2 h with 4 MPa compression. The bonding apparatus consisted of a vacuum chamber fitted with loading rams and an inductively heated molybdenum susceptor. Cross sections of the resulting interfaces were prepared for transmission electron microscopy (TEM) by low speed diamond sawing, mechanical grinding and dimpling, and ion milling. TEM revealed a contiguous 1  $\mu$ m thick interphase layer of nickel aluminate spinel between the Ni and  $\alpha$ -Al<sub>2</sub>O<sub>3</sub> (Fig. 1). The microstructural details of the spinel interphase were reported previously<sup>13</sup>.

## 2.2 Very High Vacuum Annealing

When diffusion-bonded specimens containing the spinel interphase layer were annealed in a very high vacuum of  $\sim 1 \times 10^{-5}$  Pa ( $10^{-10}$  atm), also at 1663 K for 2 h, the spinel layer disappeared (fig. 2). This result indicated the stability of the spinel depends critically upon the oxygen activity, but raised the question of whether the source of the oxygen for spinel formation during high vacuum diffusion bonding was the higher oxygen partial pressure within the bonding apparatus or oxygen initially dissolved in the Ni.



Fig. 1. Bright-field TEM image showing 1  $\mu$ m thick nickel aluminate spinel interphase layer between Ni and  $\alpha$ -Al<sub>2</sub>O<sub>3</sub> after high vacuum ( $\sim 1 \times 10^{-3}$  Pa) diffusion bonding (see J. A. Wasynczuk and M. Rühle<sup>13</sup>).

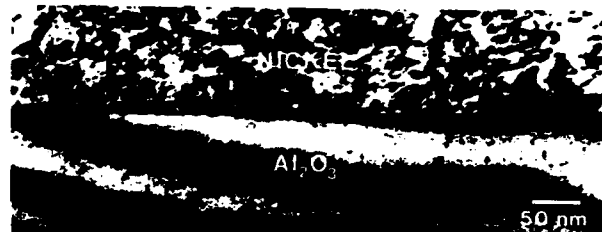


Fig. 2. Bright-field TEM image of region near spinel-containing interface after annealing in a very high vacuum of  $\sim 1 \times 10^{-5}$  Pa at 1663 K for 2 h showing no spinel layer.

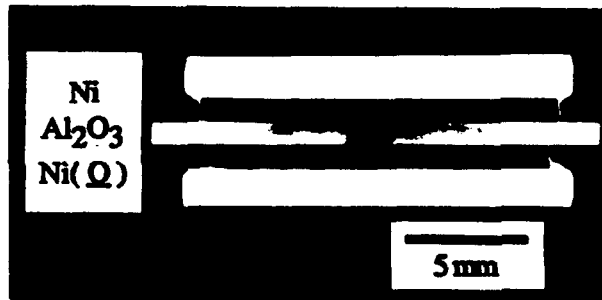


Fig. 3. Optical micrograph of polished and etched cross section of alumina/oxygen-free Ni/ $\alpha$ -Al<sub>2</sub>O<sub>3</sub>/oxygen-containing Ni/alumina diffusion bond showing smaller grain size of the oxygen-containing Ni (bottom).

## 2.3 Controlled-Oxygen Ni/Al<sub>2</sub>O<sub>3</sub> Diffusion Bonding

To elucidate the role of oxygen in spinel formation at Ni/ $\alpha$ -Al<sub>2</sub>O<sub>3</sub> interfaces, a second diffusion bonding experiment was conducted. High purity Ni (99.97 %) sheet 1 mm thick was cut to 15  $\times$  15 mm<sup>2</sup> for bonding to 1 mm thick  $\times$  20 mm diameter  $\alpha$ -Al<sub>2</sub>O<sub>3</sub> single-crystal disks (basal plane || bond plane, optical quality polish on both faces). Prior to bonding, half the Ni plates were hydrogen degassed to remove essentially all dissolved oxygen, while the others were saturated with oxygen ( $0.07 \pm 0.04$  at.%<sup>14</sup>) by pack annealing in NiO powder under flowing high purity argon. Both pretreatments were conducted at 1373 K (1100 °C) for 24 h, after which the plates were diamond polished and cleaned with acetone. Sandwiches of oxygen-free Ni/ $\alpha$ -Al<sub>2</sub>O<sub>3</sub>/oxygen-containing Ni were positioned between sintered alumina blocks and diffusion bonded in the same apparatus and under the same conditions as the first experiment (Section 2.1):  $\sim 1 \times 10^{-3}$  Pa, 1663 K, 2 h, and 4 MPa (20 K/min cooling rate). It should be noted that the oxygen-containing Ni was not saturated with oxygen at the bonding temperature, as the solubility limit of oxygen in solid Ni increases from 0.07 at.% at 1373 K to  $\approx 0.15$  at.% at 1663 K<sup>14</sup>.

The edges of the Ni plates appeared bright (unoxidized) after bonding. The bonded specimens were sectioned perpendicular to the interfaces and mechanically polished. Chemical etching revealed a smaller grain size in the oxygen-containing Ni than in the oxygen-free Ni (Fig. 3). The Ni plates experienced identical thermal histories during both pretreatment and bonding. The smaller grain size of the oxygen-containing Ni is thus most likely due to the grain

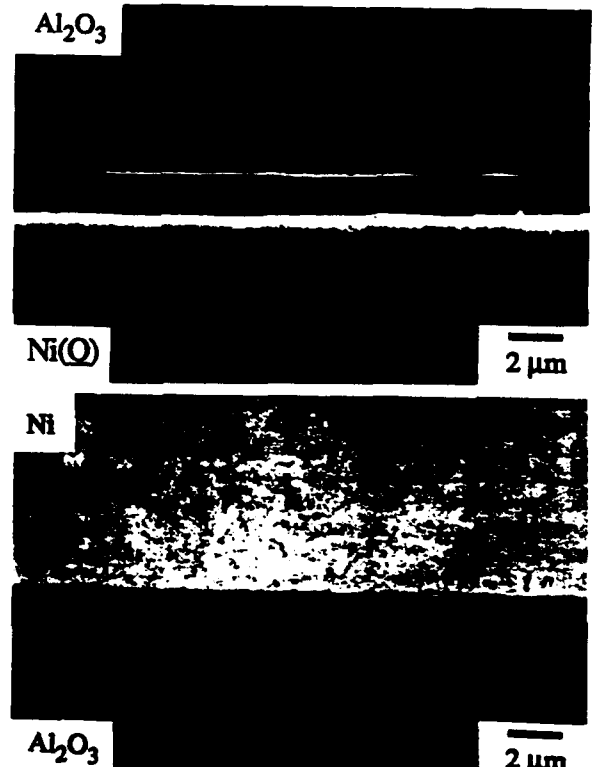


Fig. 4a and b. SEM images of regions close to diffusion-bonded Ni/ $\alpha$ -Al<sub>2</sub>O<sub>3</sub> interfaces produced under controlled-oxygen conditions. (a) Oxygen-containing Ni/ $\alpha$ -Al<sub>2</sub>O<sub>3</sub> interface showing 1.5  $\mu$ m thick spinel interphase. (b) Oxygen-free Ni/ $\alpha$ -Al<sub>2</sub>O<sub>3</sub> interface without spinel interphase.

**Bonding** growth inhibiting effect of dissolved oxygen in high purity metals<sup>15</sup>).

ation at Ni/ $\alpha$ -Al<sub>2</sub>O<sub>3</sub> single crystal, the interface between the oxygen-containing Ni and  $\alpha$ -Al<sub>2</sub>O<sub>3</sub> single crystal appeared blue, characteristic of nickel aluminate spinel<sup>16</sup>). No such coloration was observed at the oxygen-free Ni/ $\alpha$ -Al<sub>2</sub>O<sub>3</sub> interface. Scanning electron microscopy (SEM) revealed a spinel interphase layer at the oxygen-containing Ni/ $\alpha$ -Al<sub>2</sub>O<sub>3</sub> interface (Fig. 4a). The spinel was 1.5  $\mu$ m thick at the center of the interface, tapering down to  $\approx$  1.0  $\mu$ m at mid-radius, and was not resolvable within  $\sim$  1 mm of the bond edges. In contrast to the first diffusion bonding experiment (Section 2.1), the spinel layer was not fully contiguous, exhibiting discontinuous gaps all along its interface with the Ni [Fig. 4a]. No spinel reaction layer was resolvable by SEM at the oxygen-free Ni/ $\alpha$ -Al<sub>2</sub>O<sub>3</sub> interface (Fig. 4b).

Fracture along the spinel/Ni interface left the spinel layer as a thin film on the  $\alpha$ -Al<sub>2</sub>O<sub>3</sub>. TEM specimens were thus prepared by peeling off the Ni and backthinning (dimpling and ion milling) from the  $\alpha$ -Al<sub>2</sub>O<sub>3</sub> side. In plan section, the interphase layer was identified as nickel aluminate spinel by EDS and selected area electron diffraction (SAD) in an analytical electron microscope. Cross sections of the oxygen-free Ni/ $\alpha$ -Al<sub>2</sub>O<sub>3</sub> interface could be prepared for TEM by conventional cross-sectional techniques. No spinel layer was resolved by TEM with a resolution limit of 1 nm at the oxygen-free Ni/ $\alpha$ -Al<sub>2</sub>O<sub>3</sub> interface (Fig. 5).

The experimental observations suggest that a minimum oxygen activity is required for spinel formation at the Ni/ $\alpha$ -Al<sub>2</sub>O<sub>3</sub> interface. The source of the oxygen leading to spinel formation under the high vacuum conditions of the diffusion bonding experiments was oxygen initially dissolved in the Ni, not the oxygen partial pressure of the bonding atmosphere. Furthermore, the threshold oxygen level at 1663 K is less than (0.07  $\pm$  0.04 at.%), which is half the solubility limit of oxygen in Ni in equilibrium with NiO at 1663 K<sup>14</sup>). The experimental evidence thus indicates that the spinel formation reaction at Ni/ $\alpha$ -Al<sub>2</sub>O<sub>3</sub> interfaces need not proceed through a NiO intermediate.

### 3 Thermodynamic Calculations

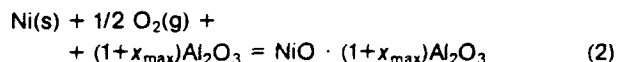
The oxygen activity dependence of spinel formation at the Ni/ $\alpha$ -Al<sub>2</sub>O<sub>3</sub> interface was explored further by equilibrium thermodynamic calculations. To write a balance spinel formation reaction between Ni and Al<sub>2</sub>O<sub>3</sub> one g-atom reactant oxygen is required per g-mole product spinel. NiAl<sub>2</sub>O<sub>4</sub> actually possesses considerable solubility for Al<sub>2</sub>O<sub>3</sub>, but essentially none for NiO. Nickel aluminate is thus most generally represented as NiO · (1+x)Al<sub>2</sub>O<sub>3</sub>, where x varies from zero (giving NiAl<sub>2</sub>O<sub>4</sub>) to x<sub>max</sub> which defines the Al<sub>2</sub>O<sub>3</sub>-saturated composition (e.g. x<sub>max</sub> = 0.38 at 1390 °C<sup>15</sup>). The first spinel to form during diffusion bonding should have the Al<sub>2</sub>O<sub>3</sub>-saturated composition because it forms in the presence of excess Al<sub>2</sub>O<sub>3</sub>. Combined with the experimental result that the reactant oxygen is dissolved in the Ni, the overall reaction is



where (O)<sub>Ni(s)</sub> denotes oxygen in solution in solid Ni.

Several determinations of the standard free energy of formation of Al<sub>2</sub>O<sub>3</sub>-saturated nickel aluminate involving gaseous reactant oxygen were available in the literature. The

particular value selected for analysis is applicable between 900 and 1400 °C<sup>18</sup>):



$$\Delta G_2^\circ = -242.090 + 74.4 T \quad (\text{J/mol}) \quad (3)$$

Park and Altstetter<sup>14</sup>) recently determined the standard free energy of solution of oxygen in solid Ni referred to a 1 at.% Henrian standard state for the dissolved oxygen

$$(\text{O})_{\text{Ni(s)}} = 1/2 \text{O}_2(\text{g}) \quad \Delta G_4^\circ = -182.000 - 70.2 T \quad (\text{J/mol}) \quad (4)$$

The standard free energy of reaction (1) is obtained by adding Eq. (3) and (4)

$$\Delta G_1^\circ = -60.090 + 4.2 T \quad (\text{J/mol}) \quad (5)$$

For reaction (1) the Al<sub>2</sub>O<sub>3</sub> and NiO · (1+x<sub>max</sub>)Al<sub>2</sub>O<sub>3</sub> are in their standard states and thus have unit activity. The Ni is also assigned unit activity because its solubility for oxygen is very low (Raoultian limit). At equilibrium the standard free energy of reaction (1) can be expressed in terms of an equilibrium constant K, which is the reciprocal of oxygen dissolved in the Ni



Fig. 5. TEM of diffusion-bonded Ni/ $\alpha$ -Al<sub>2</sub>O<sub>3</sub> interfaces produced under controlled-oxygen conditions: Bright-field of cross section close to oxygen-free Ni/ $\alpha$ -Al<sub>2</sub>O<sub>3</sub> interface without spinel.

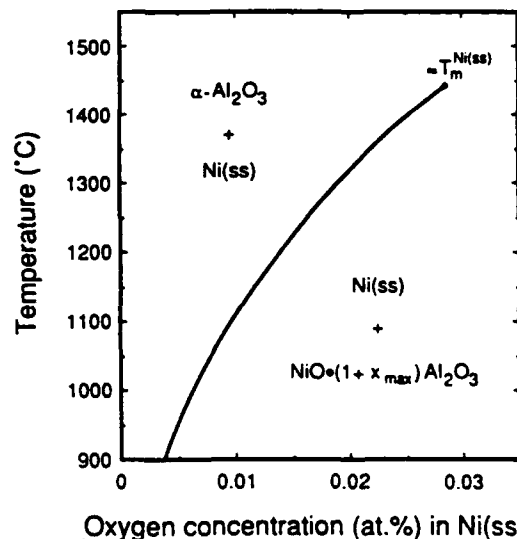


Fig. 6. Stability diagram of the calculated oxygen concentration in the Ni solid solution for the (Ni(ss), NiO · (1+x<sub>max</sub>)Al<sub>2</sub>O<sub>3</sub>,  $\alpha$ -Al<sub>2</sub>O<sub>3</sub>) equilibrium as a function of temperature [Eq. (10)].



$$\Delta G_i^\circ = -RT \ln K = RT \ln a_{\text{O}_2} \quad (6)$$

Solving for  $a_{\text{O}_2}$  with Eq. (5) and (6) yields the equilibrium oxygen activity for spinel formation during Ni/ $\alpha$ -Al<sub>2</sub>O<sub>3</sub> diffusion bonding, expressed in at.%,

$$(\text{at.}\% \text{ O}) = \exp(-7550 \pm 1200/T + 0.84) \quad (7)$$

Equation (7) is plotted in Fig. 6. Confirming the experimental results, it indicated that below a threshold oxygen activity, which increases with increasing temperature, oxygen-containing Ni is in equilibrium with Al<sub>2</sub>O<sub>3</sub>, whereas above the threshold the spinel is stable. Furthermore, the calculated threshold oxygen activity at 1390 °C is 220 at.ppm, quantitatively consistent with the experimental result that the threshold is less than 670 at.ppm.

#### 4 Spinel Thickness Evaluation

Several other principle features of the spinel formation reaction at Ni/ $\alpha$ -Al<sub>2</sub>O<sub>3</sub> interfaces follow directly from the oxygen activity dependence described in the previous sections. First, the reaction consumes a certain excess of oxygen dissolved in the Ni. For a closed system, the spinel layer thickness thus exhibits a maximum, which is determined by the difference between the initial and threshold oxygen concentrations and the Ni thickness. A mass balance (Appendix 7.1) for the conditions of the controlled-oxygen diffusion bonding experiment (Section 2.3) yields a predicted maximum spinel thickness of  $1.7 \pm 2.3 \mu\text{m}$ , in good agreement with the measured thickness of  $1.5 \mu\text{m}$  (Fig. 4a). A similar analysis using the solubility limit of oxygen in solid Ni<sup>14)</sup> yields the maximum possible thickness of spinel formed from initially dissolved oxygen as  $\approx 0.005$  times the Ni thickness.

Second, the reactant oxygen must diffuse from within the Ni to the interface. A detailed analysis of the reaction mechanism and kinetics is not presented in this article. It is clear, however, that the reaction can occur no faster than the oxygen can diffuse to the interface. Assuming oxygen transport in the Ni to be the rate-determining step of the reaction, the relative extent of the reaction can be calculated with well-known diffusion equations. Calculations detailed in Appendix 7.2 indicate that essentially all the reactable oxygen was kinetically capable of reaching the interfaces in the controlled-oxygen bonding experiment.

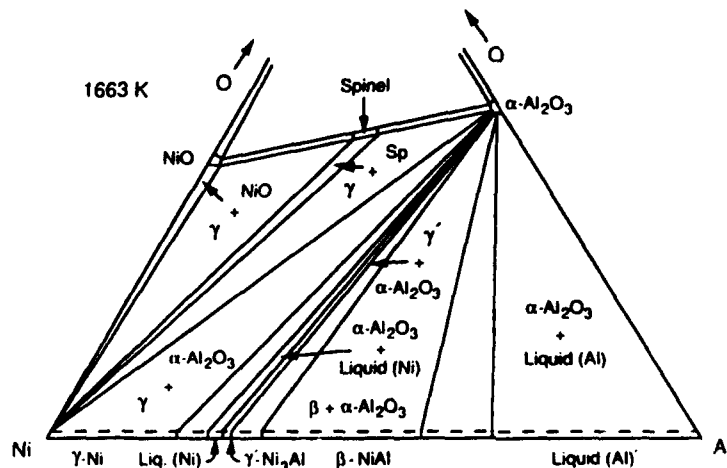


Fig. 7. The assessed Ni-Al-O phase diagram at 1663 K. Some solubilities exaggerated for clarity.

The agreement between the predicted and measured spinel thickness thus suggests that oxygen diffusion in the Ni was indeed the rate-determining step of the reaction and further substantiates the thermodynamically calculated threshold oxygen activity. Reported thicknesses of spinel layers that formed at Ni/ $\alpha$ -Al<sub>2</sub>O<sub>3</sub> interfaces in vacuum or inert gas atmospheres for times and temperatures similar to the present experiments are also of the order of  $1 \mu\text{m}$ .

## 5 Discussion

### 5.1 Threshold Oxygen Activity

The experimental observations and thermodynamic calculations show that a threshold activity of oxygen is required for spinel formation at Ni/ $\alpha$ -Al<sub>2</sub>O<sub>3</sub> interfaces. In the high vacuum diffusion bonding experiments the source of the required oxygen was oxygen initially dissolved in the Ni. The experiments and calculations also show that the minimum oxygen activity necessary for spinel formation is an order of magnitude less than the solubility limit of oxygen in Ni (NiO-saturated) and increases with temperature. Although these results clearly dispell the long-standing notion that the spinel formation reaction necessarily proceeds through a NiO intermediate, thermodynamic data were in fact available as early as 1942<sup>19)</sup> indicating the lower oxygen partial pressure of the {Ni, spinel, Al<sub>2</sub>O<sub>3</sub>} equilibrium relative to the {Ni, NiO} equilibrium. The numerous reports of spinel formation in vacuum and inert gas atmospheres are not surprising since oxygen contents exceeding the threshold are typical of "high purity" Ni, especially powders<sup>4)</sup>.

### 5.2 Ni-Al-O Phase Diagram and the Diffusion Path

A complete description of the phase equilibria relevant to microstructural development at Ni/ $\alpha$ -Al<sub>2</sub>O<sub>3</sub> interfaces would utilize the Ni-Al-O ternary phase diagram. Based on the ternary phase relationships at 1273 K presented by Elrefaie and Smeltzer<sup>17)</sup> and NiO-Al<sub>2</sub>O<sub>3</sub> and Ni-Al phase diagrams<sup>21)22)</sup>, a Ni-Al-O isothermal section at 1663 K has been assessed (Fig. 7). The Ni corner has not yet been quantitatively assessed. Metselaar and van Loo<sup>23)</sup> quantitatively presented the phase relationships in the Ni corner with Ni/ $\alpha$ -Al<sub>2</sub>O<sub>3</sub> diffusion paths for different oxygen activ-

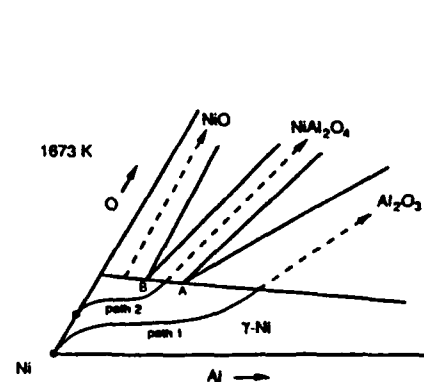


Fig. 8. Qualitative phase relationships of the Ni-rich Ni-Al-O phase diagram as presented by Metselaar and van Loo<sup>23)</sup> showing diffusion paths for Ni/ $\alpha$ -Al<sub>2</sub>O<sub>3</sub> couples (path 1: low oxygen, path 2: higher oxygen).

ities (Fig. 8). These diffusion paths represent the dissolution of  $\alpha$ -Al<sub>2</sub>O<sub>3</sub> into Ni at internal interfaces, and thus the diffusion of oxygen and Al away from the interface. These authors propose that, because oxygen diffuses much faster than Al in Ni, Ni/ $\alpha$ -Al<sub>2</sub>O<sub>3</sub> diffusion paths extend across the  $\gamma$ -Ni solid solution field predominantly parallel to the Ni-Al border. A diffusion path showing a stable Ni/ $\alpha$ -Al<sub>2</sub>O<sub>3</sub> interface at low oxygen activity is shown as path 1 in Fig. 8. It was assumed that the diffusion coefficients of oxygen and Al in dilute solutions in the  $\gamma$ -Ni are essentially independent of concentration, hence additional oxygen would shift the diffusion path to higher oxygen levels. At some level of supplementary oxygen the diffusion path would connect with the  $\gamma$ -Ni + spinel field (path 2), supposedly resulting in spinel formation. Observations of Ostwald ripening of  $\alpha$ -Al<sub>2</sub>O<sub>3</sub> particles in Ni<sup>(24,25)</sup> provide evidence that  $\alpha$ -Al<sub>2</sub>O<sub>3</sub> does dissolve to a certain extent in solid Ni. Moreover, measured diffusivities at 1673 K ( $D_{(O \text{ in Ni})} = 3.7 \times 10^{-7} \text{ cm}^2/\text{s}$  and  $D_{(Al \text{ in Ni})} = 8.1 \times 10^{-9} \text{ cm}^2/\text{s}$ ) suggest that oxygen dissolving into Ni from  $\alpha$ -Al<sub>2</sub>O<sub>3</sub> would diffuse away from the interface faster than the accompanying Al. The diffusion paths proposed by Metselaar and van Loo<sup>(23)</sup> thus seem to be qualitatively correct for the dissolution of  $\alpha$ -Al<sub>2</sub>O<sub>3</sub> into Ni.

A deeper understanding of the chemical interactions can be obtained, however, with a calculated Ni corner of the Ni-Al-O phase diagram. Specifically, the oxygen concentration in  $\gamma$ -Ni for the  $\{\gamma\text{-Ni, NiO} \cdot (1-x_{\text{max}})\text{Al}_2\text{O}_3, \alpha\text{-Al}_2\text{O}_3\}$  coexistence (point A, Fig. 8) is 0.025 at.% at 1663 K as calculated in Section 3. This value is an order of magnitude less than the solubility limit of oxygen in Ni. It remains to determine the corresponding Al concentrations. Elrefaie and Smeltzer<sup>(17)</sup> calculated a value of  $\sim 1 \times 10^{-9}$  at.% for  $\gamma$ -Ni for the  $\{\gamma\text{-Ni, NiO} \cdot (1-x_{\text{max}})\text{Al}_2\text{O}_3, \alpha\text{-Al}_2\text{O}_3\}$  coexistence at 1213 K. An analysis in Appendix 7.3 yields  $\approx 2 \times 10^{-5}$  at.% Al at 1663 K, three orders of magnitude smaller than the corresponding oxygen level (0.025 at.% oxygen). Similar calculations (Appendix 7.3) indicate  $\sim 6 \times 10^{-7}$  at.% in  $\gamma$ -Ni for the  $\{\gamma\text{-Ni, NiO, NiAl}_2\text{O}_4\}$  coexistence (point B, Fig. 8) at 1663 K.

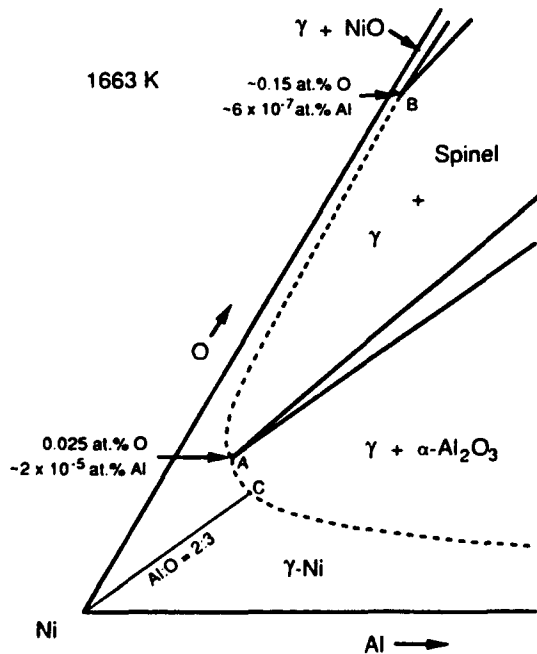


Fig. 9. Ni-rich corner of the Ni-Al-O phase diagram at 1663 K calculated in the present work. The  $\gamma$ -Ni solid solution is not entirely to scale.

The Ni corner of the Ni-Al-O phase diagram constructed using these compositions and phase diagram principles<sup>(26)</sup> is shown in Fig. 9.

There are two important implications of the calculated phase diagram. First, consider in more detail the dissolution of  $\alpha$ -Al<sub>2</sub>O<sub>3</sub> into pure Ni. Assuming negligible solubility of Ni in  $\alpha$ -Al<sub>2</sub>O<sub>3</sub> at the low oxygen activities in consideration, the dissolution is congruent. If the diffusivities of oxygen and Al in Ni were equal, the diffusion path would extend across the  $\gamma$ -Ni field along the Al:O = 2:3 isopleth, establishing the equilibrium interface concentrations in the  $\gamma$ -Ni at point C in Fig. 9. The higher diffusivity of oxygen, however, shifts the equilibrium interface toward lower oxygen and higher Al concentrations than point C. Hence, the dissolution of  $\alpha$ -Al<sub>2</sub>O<sub>3</sub> into oxygen-free Ni cannot provide sufficient oxygen to form spinel.

Second, the calculated composition of  $\gamma$ -Ni for the  $\{\gamma\text{-Ni, NiO} \cdot (1+x_{\text{max}})\text{Al}_2\text{O}_3, \alpha\text{-Al}_2\text{O}_3\}$  coexistence (point A, Fig. 9) is  $\approx 1000$  times higher in oxygen than Al. Diffusion paths for spinel formation actually lie within the extremely narrow  $\gamma$ -Ni solid solution region along the Ni-O border (Fig. 9). This emerges the importance of the threshold oxygen activity (thermodynamics) for spinel formation as opposed to any diffusion path (kinetics) associated with establishing local equilibrium Al activities by dissolution of  $\alpha$ -Al<sub>2</sub>O<sub>3</sub>. Diffusion paths for spinel formation at internal Ni/ $\alpha$ -Al<sub>2</sub>O<sub>3</sub> interfaces represent diffusion of oxygen in the Ni to the interfaces. The Al concentration in  $\gamma$ -Ni required for equilibrium with the spinel (point A, Fig. 9) is so small relative to the corresponding oxygen concentration that the required extent of the dissolution of  $\alpha$ -Al<sub>2</sub>O<sub>3</sub> is insignificant.

## 6 Conclusions

The oxygen activity dependence of spinel interphase formation at Ni/ $\alpha$ -Al<sub>2</sub>O<sub>3</sub> interfaces has been clarified. Spinel formation at internal Ni/ $\alpha$ -Al<sub>2</sub>O<sub>3</sub> interfaces requires a threshold activity of oxygen dissolved in the Ni, which increases with temperature and is less than the solubility limit of oxygen in Ni in equilibrium with NiO. Spinel formation thus need not proceed through a NiO intermediate. Thermodynamic calculations indicate the threshold oxygen level is 250 at.ppm at 1663 K and that the corresponding equilibrium Al concentration is three orders of magnitude lower ( $\approx 0.2$  at.ppm).

The oxygen activity dependence of spinel formation also provides insight into the reaction mechanism and kinetics. The reaction at internal interfaces consumes oxygen dissolved in the Ni. Due to the low solubility of oxygen in Ni, the maximum thickness of spinel that can be formed from oxygen initially dissolved in Ni is limited to  $\approx 0.005$  times the Ni thickness. The present observations suggest oxygen transport in the Ni is the rate-determining step of the spinel formation reaction. Further studies of the reaction mechanism and kinetics are in progress.

## 7 Appendices

### 7.1 Prediction of Maximum Spinel Layer Thickness

The maximum spinel layer thickness is predicted for the conditions of the controlled-oxygen diffusion bonding experiment by a mass balance on the reactable oxygen. Consider a  $1 \times 1 \times 0.1 \text{ cm}^3$  basis of Ni containing 0.070

( $\pm 0.040$ ) - 0.025 ( $\pm 0.020$ ) = 0.045 ( $\pm 0.060$ ) at.% reactable oxygen. One  $\eta$ -atom of oxygen is consumed per  $g$ -mole of product spinel. The volume of product spinel is calculated assuming a composition of  $\text{NiO} \cdot 1.38 \text{Al}_2\text{O}_3$ <sup>21)</sup> and density of 4.3  $\text{g}/\text{cm}^3$ <sup>27)</sup>. The resulting spinel volume is divided by two times the area of the basis to account for spinel formation on both sides of the Ni plate in contact with  $\alpha$ - $\text{Al}_2\text{O}_3$  (spinel was also observed between the oxygen-containing Ni and the sintered alumina block). Dimensional analysis yields a predicted maximum thickness of  $1.7 \pm 2.3 \mu\text{m}$ :

$$\frac{0.1 \text{ cm}^3 \text{ Ni}}{2 \text{ cm}^2 \text{ spinel}} \times \frac{8.90 \text{ g/cm}^3 \text{ Ni}}{58.7 \text{ g/mol Ni}} \times \frac{0.00045 \text{ mol O}_{\text{Ni}}}{1 \text{ mol Ni}} \times \frac{1 \text{ mol spinel}}{1 \text{ mol O}_{\text{Ni(s)}}} \times \frac{215.4 \text{ g/mol spinel}}{4.3 \text{ g/cm}^3 \text{ spinel}} = 1.7 \pm 2.3 \mu\text{m spinel} \quad (\text{A } 1.1)$$

## 7.2 Estimation of Relative Extent of Reaction

The relative extent of spinel formation at the Ni/ $\alpha$ - $\text{Al}_2\text{O}_3$  interfaces is estimated assuming that the rate-determining step of the reaction is the diffusion of oxygen from within the Ni to the interfaces. Considering a thin Ni plate sandwiched between two  $\alpha$ - $\text{Al}_2\text{O}_3$  blocks, the relative extent of reaction takes the form of the well-known series solution for diffusion out of a semi-infinite slab at constant surface activity<sup>28)</sup>

$$\frac{c_m - c_i}{c_o - c_i} = \frac{8}{\pi^2} \sum_{n=0}^{\infty} \frac{1}{(2n+1)^2} \exp \left\{ - \left[ \frac{(2n+1)\pi}{L} \right]^2 Dt \right\} \quad (\text{A } 2.1)$$

where  $c_m$ ,  $c_i$ , and  $c_o$  are the mean, interface, and uniform initial solute concentrations, respectively,  $D$  the solute diffusivity,  $t$  the time, and  $L$  the slab thickness. Evaluating the relative extent of diffusion with  $D_{(\text{O in Ni})} = 3.4 \times 10^{-7} \text{ cm}^2/\text{s}$  at 1663 K<sup>14)</sup>,  $t = 2 \text{ h}$ , and  $L = 1 \text{ mm}$  indicates 94 % of the reactable oxygen was kinetically capable of reaching the interfaces in the controlled-oxygen diffusion bonding experiment. Estimating the additional contribution from the heating and cooling transients suggests the diffusion of oxygen to the interfaces, and hence reaction, was more than 97 % complete during the bonding period.

In the first diffusion bonding experiment (Section 2.1) all the parameters were the same as above except that the Ni was 1.5 mm thick. The strong thickness dependence of the diffusion time results in a relative extent of reaction of only 73 % after 2 h at 1663 K. Including the heating and cooling transients as above, the relative extent of reaction increases to 77 %. In contrast to the controlled-oxygen diffusion bonding experiment, the calculations thus indicate that a supply of dissolved oxygen to the interfaces by diffusion from within the Ni was maintained throughout the bonding cycle in the first experiment.

## 7.3 Estimation of Equilibrium Al Concentrations at 1663 K

The Al concentrations in  $\gamma$ -Ni for the three-phase equilibria  $\{\gamma\text{-Ni, NiO} \cdot (1+x_{\text{max}})\text{Al}_2\text{O}_3, \alpha\text{-Al}_2\text{O}_3\}$  and  $\{\gamma\text{-Ni, NiO, NiAl}_2\text{O}_4\}$  are estimated by calculating the Al activities and estimating the Al activity coefficient. Combining Eq. (4) with the standard free energy of formation of  $\alpha\text{-Al}_2\text{O}_3$ <sup>29)</sup> gives the standard free energy of formation of  $\text{NiO} \cdot (1+x_{\text{max}})\text{Al}_2\text{O}_3$  from the elements. Expressing this in terms of the equilibrium constant and solving for the Al activity with Eq. (5) gives  $a_{\text{Al}} = 4.5 \times 10^{-13}$  (liquid Al standard state) for the  $\{\gamma\text{-Ni, NiO} \cdot (1+x_{\text{max}})\text{Al}_2\text{O}_3, \alpha\text{-Al}_2\text{O}_3\}$  coexistence at 1663 K.

Calculation of  $a_{\text{Al}}$  for the  $\{\gamma\text{-Ni, NiO, NiAl}_2\text{O}_4\}$  coexistence begins by solving for  $a_{\text{NiO}}$ . Elrefaie and Smeltzer<sup>17)</sup> measured the oxygen pressure of the  $\{\gamma\text{-Ni, NiO, NiAl}_2\text{O}_4\}$  coexistence over the range 1123 to 1423 K

$$\log P_{\text{O}_2} = \frac{-24.478}{T} + 8.804 \quad \text{atm} \quad (\text{A } 3.1)$$

Extrapolating Equation (A 3.1) to 1663 K and solving for  $a_{\text{NiO}}$  with the standard free energy of formation of  $\text{NiO}$ <sup>29)</sup> gives  $a_{\text{NiO}} = 0.90$ . Measurements<sup>21)</sup> suggest the solubility of  $\alpha\text{-Al}_2\text{O}_3$  in NiO is  $\sim 2.7 \text{ mol}\%$  at 1663 K. The standard free energy of formation of stoichiometric  $\text{NiAl}_2\text{O}_4$  from the binary oxides is  $-27,700 \text{ J/g-mol}$  at 1663 K based on the 298 K standard enthalpy and entropy and heat capacity data reported by Kubaschewski<sup>29)</sup>. Adding the standard free energy of formation of  $\alpha\text{-Al}_2\text{O}_3$ <sup>29)</sup> and solving for  $a_{\text{Al}}$  with Eq. (A 3.1) and  $a_{\text{NiO}} = 0.90$  yields  $a_{\text{Al}} \sim 1.3 \times 10^{-14}$  (liquid Al standard state) for the  $\gamma\text{-Ni, NiO, NiAl}_2\text{O}_4$  coexistence at 1663 K.

Expressing the calculated activities in terms of mol fractions requires the Al activity coefficient. Elrefaie and Smeltzer<sup>17)</sup> measured an activity coefficient for Al in Ni of  $\gamma_{\text{Al}} \approx 4 \times 10^{-8}$  at 1213 K (liquid Al standard state) with mol fraction-activity data from a series of dilute Ni-Al alloys equilibrated with  $\alpha\text{-Al}_2\text{O}_3$ . Since most nonideal solutions tend toward ideality with increasing temperature<sup>30)</sup>,  $\gamma_{\text{Al}}$  should increase with increasing temperature. The value of  $\gamma_{\text{Al}}$  at 1663 K is estimated by integration of the Gibbs-Helmholtz equation<sup>30)</sup>

$$\ln \frac{\gamma_{\text{Al}}^{T_2}}{\gamma_{\text{Al}}^{T_1}} = \frac{\Delta \bar{H}_{\text{Al}}}{R} \left[ \frac{1}{T_2} - \frac{1}{T_1} \right] \quad (\text{A } 3.2)$$

with a measured value of the partial molar enthalpy of solution of Al in Ni,  $\Delta \bar{H}_{\text{Al}} = -146 \text{ kJ/g-mole}$ <sup>31)</sup>, and the measured 1213 K activity coefficient. The result is  $\gamma_{\text{Al}} \approx 2 \times 10^{-6}$ . Alternately, assuming a regular solution, the temperature dependence of the activity coefficient is given by<sup>30)</sup>

$$\frac{\ln \gamma_{\text{Al}}^{T_2}}{\ln \gamma_{\text{Al}}^{T_1}} = \frac{T_1}{T_2} \quad (\text{A } 3.3)$$

from which  $\gamma_{\text{Al}} \approx 4 \times 10^{-6}$  at 1663 K, in good agreement with the value obtained above from the measured heat of solution.

The calculated activities and estimated activity coefficient give  $X_{\text{Al}} \approx 2 \times 10^{-7}$  in  $\gamma$ -Ni for the  $\{\gamma\text{-Ni, NiO} \cdot (1+x_{\text{max}})\text{Al}_2\text{O}_3, \alpha\text{-Al}_2\text{O}_3\}$  coexistence and  $X_{\text{Al}} = 6 \times 10^{-9}$  in  $\gamma$ -Ni for the  $\{\gamma\text{-Ni, NiO, NiAl}_2\text{O}_4\}$  coexistence at 1663 K.

The authors gratefully acknowledge helpful discussion with A.G. Evans, H. Schmalzried and K. C. Vlach.

## Literature

- 1) M. RÜHLE and A. G. EVANS, *Mater. Res. Soc. Symp. Proc.* **120** (1988) 293.
- 2) I. E. REIMANIS, B. J. DALGLEISH, M. B. SAHY, M. RÜHLE, and A. G. EVANS, *Acta Metall.*, in press.
- 3) A. G. EVANS and J. W. HUTCHINSON, *Acta Metall.* **37** (1989) 909.
- 4) C. A. CALOW and I. T. PORTER, *J. Mater. Sci.* **6** (1971) 156.
- 5) R. G. VARDIMAN, *Mater. Res. Bull.* **7** (1972) 699.
- 6) G. ELSSNER and G. PETZOW, *Z. Metallkde.* **64** (1973) 280.
- 7) W. H. SUTTON and FEINGOLD, *The Role of Grain Boundaries and Surfaces in Ceramics*, W. W. Kriegel and H. P. Palmour III (eds.), Plenum Press, New York (1966) 577.

existence  
of meas-  
urements of  
Al<sub>2</sub>O<sub>3</sub> co-

(A 3.1)

of  $a_{NiO}$   
gives  
the value of  $\alpha$   
and free  
energy of the bin-  
odal region at 298 K  
from the data  
of the free  
energy of Al  
standards at 1663 K.

mol frac-  
tion of Al  
in Ni of  
Al alloys  
with mol  
fraction of  
Al<sub>2</sub>O<sub>3</sub>  $\gamma_{Al}$   
value of  
the Helmholtz

(A 3.2)

of solu-  
tion meas-  
urements of  $2 \times 10^{-6}$   
at temperature  
by  $\gamma_{Al}$

(A 3.3)

ment with  
that of solu-

efficient  
of Al<sub>2</sub>O<sub>3</sub>  
in the  $\gamma$ -Ni,

discussion  
of

Proc. 120

RÜHLE, and

37 (1989)

(1971) 156.

(1973) 280.  
boundaries  
of Palmour III

- 1) C. A. CALOW, P. B. BAYER, and I. T. PORTER, *J. Mater. Sci.* **6** (1971) 150.
- 2) F. P. BAILEY and W. E. BORBRIDGE, *Mater. Sci. Res.* **6** (1971) 150.
- 3) M. G. GEE, *Brit. Ceram. Proc.* **34** (1984) 261.
- 4) A. J. STAPLEY and C. J. BEEVERS, *J. Mater. Sci.* **8** (1973) 1287.
- 5) L. J. WESTFALL, NASA Tech. Memo. TM-X3333 (1976).
- 6) J. A. WASYNCZUK and M. RÜHLE, *Ceramic Microstructures '86 - Role of Interfaces*, J. A. Pask and A. G. Evans (eds.), Plenum Press, New York (1987) 341.
- 7) J. W. PARK and C. J. ALTSTETTER, *Metall. Trans.* **18A** (1987) 43.
- 8) D. L. WOOD, *Trans. AIME* **209** (1957) 406.
- 9) M. BACKHAUS-RICOULT, *Ber. Bunsenges. Phys. Chem.* **90** (1986) 684.
- 10) F. A. ELREFAIE and W. W. SMELTZER, *J. Electrochem. Soc.* **128** (1981) 2237.
- 11) L. M. LENEV and I. A. NOVOKHATSKII, *Russ. J. Inorg. Chem.* **10** (1965) 1307.
- 12) R. FRICKE and G. WEITBRECHT, *Z. Electrochem. Angew. Phys. Chem.* **48** (1942) 87.
- 13) R. F. BUNSHAH and M. A. COCCA, *Techniques of Materials Preparation and Handling*, R. F. Bunshah (ed.), Vol. 1, Pt. 2 (1968).
- 14) F. A. ELREFAIE and W. W. SMELTZER, *Oxid. Met.* **15** (1981) 495.
- 15) M. F. SINGLETON, J. L. MURRAY, and P. NASH, *Binary Alloy Phase Diagrams*, T. B. Massalski (ed.), Vol. 1. ASM, Metals Park, OH (1986) 140.
- 16) R. METSELAAR and F. J. J. VAN LOO, *Ceramic Developments*, C. C. Sorrell and B. Ben-Nissan (eds.), Trans. Tech. Pub. Ltd, Switzerland (1988) 413.
- 17) M. H. LEWIS, R. H. SEEBOHM, and J. W. MARTIN, *Powder Metall.* **10** (1962) 87.
- 18) J. A. DROMSKY, F. V. LENEL, and G. S. ANSELL, *Trans. AIME* **224** (1962) 236.
- 19) F. N. RHINES, *Phase Diagrams in Metallurgy*, McGraw-Hill, New York (1956).
- 20) J. D. TRETJAKOW and H. SCHMALZRIED, *Ber. Bunsenges. Phys. Chem.* **69** (1965) 396.
- 21) W. JOST, *Diffusion in Solids, Liquids and Gases*, Academic Press, New York (1960).
- 22) O. KUBASCHEWSKI and C. B. ALCOCK, *Metallurgical Thermochemistry*, 5th Ed., Pergamon Press, Oxford (1979).
- 23) D. R. GASKELL, *Introduction to Metallurgical Thermodynamics*, 2nd. Ed., McGraw-Hill, New York (1981).

(Eingegangen am 6. März 1990)